Variable Speed Scissored Pair Dual Gimbal Control Moment Gyro for Nano-Satellites

by

Douw Steyn

Thesis presented in partial fulfilment of the requirements for the degree
Master of Engineering
in the Faculty of Engineering at Stellenbosch University.

Supervisor:
Prof W.H. Steyn

Department of Electrical and Electronic Engineering

December 2015

Acknowledgements

I would like to thank the following people for their help and support throughout the past two years:

- Prof WH Steyn for all his knowledge and experience in ADCS design.
- Mr Johan Arendse for his exceptional soldering skills.
- Mr Lincoln Saunders for manufacturing the mechanical components.
- Mr Philipp Wagner for his fabrication of the gears.
- Willem Jordaan, Jako Gerber, Mike-Alec Kearney, Christo Groenewald and Gerhard Janse van Vuuren that had to endure my constant stream of questions.
- Nico Calitz, Nico Rossouw and Muhammad Junaid for their patience and composure.
- SANSA for their financial support.
- Finally, my parents for their unwavering love and support.

Declaration

By submitting this thesis electronically, I declare that the entirety of the work contained herein is my own, original work, that I am the sole author thereof (save to the extent explicitly otherwise stated), that reproduction and publication thereof by Stellenbosch University will not infringe any third party rights and that I have not previously in its entirety or in part submitted it for obtaining any qualification.

December 2015

Abstract

The work presented in this thesis describes the development of an attitude control actuator for use in CubeSats. This actuator uses novel Control Moment Gyro technology to perform slew manoeuvres. The configuration consists of a symmetric pair of counter-rotating gyros mounted in scissoring dual gimbals. The outer gimbals are mechanically constrained using gears driven by a single stepper motor while the inner gimbals are individually actuated using two additional stepper motors. Three-axis control is achieved by changing the gimbal angles for roll and pitch manoeuvres and varying the wheel speed for yaw rotations. Electronics were designed to control the momentum wheel motors and the gimbal angle actuators. A mathematical model was derived from the mechanical design. The model was used in simulations where a slew manoeuvre was performed in each axis individually in order to match the Hardware-in-the-Loop test conditions. The average power usage, for the three-axis implementation, during a slew manoeuvre was measured at 420 milli-Watt with maximum of 556 milli-Watt. The volume required for the actuator is only 10 cm x 5 cm x 5 cm and has a mass of 260 g, making it suitable for CubeSat use.

The attitude controllers tested include a Bang-Off-Bang and a Quaternion Feedback controller. The controllers are typically combined for large slew manoeuvres: The Bang-Off-Bang controller is used first and at the required final attitude, the Quaternion Feedback controller is enabled to accurately track the reference angle. Hardware-in-the-Loop tests were done on a low-friction air bearing platform for ground based attitude control demonstrations. Attitude knowledge was obtained from a MEMS inertial measurement unit and a laser pointer. Tests were repeated for various platform moments of inertia in order to empirically determine the expected pointing accuracy of the system. Similar tests were also performed using a conventional reaction wheel configuration to compare the performance. A maximum torque of 0.52 mNm can be achieved by this new actuator and a pointing accuracy of less than 0.2 degrees was demonstrated on the air bearing platform. Initial results show satisfactory performance to justify further development of a flight actuator module.

Uittreksel

Die doel van hierdie tesis is om 'n oriëntasie aktueerder te ontwikkel wat in CubeSats gebruik kan word. Hierdie aktueerder voer rotasie bevele uit deur gebruik te maak van 'n innoverende BeheerMoment Giroskoop (BMG) ontwerp. Die ontwerp bestaan uit 'n identiese paar van teenoor-roterende giroskope wat in dubbele rame gemonteer is. Beide buiterame roteer met dieselfde hoek in teenoorgestelde rigtings, sowel as die binnerame. Die buiterame is meganies gekoppel met ratte en roteer met behulp van 'n enkele stappermotor, terwyl die binnerame elkeen met hul eie stappermotor aangedryf word. Drie-as beheer word moontlik gemaak deur die rame te roteer vir rol en duik en die wielspoed te verander vir gier rotasies. Elektronika is ontwerp om die stapper en GS motors te beheer, waarna 'n wiskundige model vir die hardeware ontwerp ontwikkel is. Hierdie model is gebruik in simulasies om rotasies in elke as te toets en hardeware toetse is gedoen om die metings te bevestig. Die gemiddelde kragverbruik van die volledige ontwerp is 420 milli-Watt, met maksimum van 556 milli-Watt. Die stelsel is geskik vir nano-satelliete aangesien die volume slegs 10 cm x 5 cm x 5 cm is, en die massa 260 g is.

Die rigting beheerdertegnieke wat getoets is sluit in 'n Aan-Af-Aan en 'n Kwarternioon-terugvoerbeheerder. Hierdie word dikwels saam gebruik vir groot rotasies. Die Aan-Af-Aan beheerder word eerstens gebruik om die gewenste hoek te bereik, waarna daar na die Kwarternioon-terugvoer oorgeskakel word om die finale hoek akkuraat te volg. Hardeware toetse is uitgevoer deur van 'n luglaer, wat amper wrywinglose rotasies toelaat, gebruik te maak. Rigtingmetings was verkry met 'n MEMS inersieële sensor en 'n laserwyser. Deur sleurtoetse op die luglaer vir verskeie traagheidsmomente te herhaal, is 'n oriëntasie akkuraatheid van 0.2 grade behaal. Om die resultate te vergelyk, is dieselfde toetse ook uitgevoer op 'n enkele groot reaksiewiel. Die maksimum wringkrag wat die stelsel gedurende toetse behaal het, was 0.52 mNm. Hierdie resultate dui daarop dat die ontwerp genoeg voordele inhou om verdere ontwikkeling te doen en 'n vlugmodel te oorweeg.

Table of Contents

List of Figures

List of Tables

Nomenclature

List of Abbreviations

ADCS	Attitude Determination and Control System
BLDC	Brushless DC
CAN	Controller Area Network
CMG	Control Moment Gyroscope
DC	Direct Current
DCM	Direction Cosine Matrix
DGCMG	Dual Gimbal CMG
EMF	Electromotive Force
EPS	Electrical Power System
ESL	Electronic Systems Laboratory
HIL	Hardware-in-the-Loop
I2C	Inter-Integrated Circuit
IC	Integrated Circuit
ISS	International Space Station
LSB	Least Significant Bit
MEMS	Micro Electro Mechanical Systems
MISO	Master Input Slave Output
MOI	Moment Of Inertia

MOSI	Master Output Slave Input
MSB	Most Significant Bit
OBC	On Board Computer
PC	Personal Computer
PCB	Printed Circuit Board
PID	Proportional Integral Derivative
PWM	Pulse Width Modulation
RPM	Rotations Per Minute
RX	Receive bus
SCK	Serial Clock
SGCMG	Single Gimbal CMG
SPI	Serial Peripheral Interface
$\overline{\text{SS}}$	Slave Select
TX	Transmit bus
UART	Universal Asynchronous Receiver/Transmitter
U	Unit

List of Symbols

θ	Slew angle
ζ	Damping ratio
$\mathbf{B}$	Attitude control system Jacobian matrix
$\mathbf{B}_E$	Earth's magnetic field vector
$\mathbf{C}_A^B$	Rotation matrix from reference frame A to B
C_{ij}	Rotation matrix element
$\boldsymbol{\delta}$	Gimbal angle

δ_1	Inner gimbal angle
δ_2	Outer gimbal angle
Δh	Differential component of wheel angular momentum
$\mathbf{e}$	Euler axis vector
$\mathbf{h}$	Angular momentum
h_0	Common component of wheel angular momentum
$\mathbf{h}_{\text{max}}$	Maximum angular momentum build-up
$\mathbf{h}_{\text{total}}$	Total DGCMG angular momentum
$\mathbf{I}$	Satellite moment of inertia vector
I_{wheel}	Flywheel moment of inertia
$\mathbf{M}$	Magnetic dipole moment vector
$\mathbf{N}$	Torque
$\mathbf{N}_c$	Commanded torque for magnetorquers
$\mathbf{N}_{\text{DGCMG}}$	Torque generated by DGCMG
$\mathbf{N}_{\text{disturb}}$	External disturbance torques
$\mathbf{N}_{\text{max}}$	Maximum torque for each DGCMG axis
$\mathbf{N}_{\text{slew}}$	Satellite slew torque
ω_{f}	Flywheel angular rate
ω_n	Natural frequency
$\boldsymbol{\omega}_B^I$	Angular rate of satellite body inertially referenced
$\mathbf{q}$	Quaternion
$\mathbf{q}_e$	Rotation error Quaternion
$\mathbf{q}_f$	Final rotation Quaternion
q_i	Quaternion element

$\mathbf{q}_{\text{vec}}$	Vector containing first three Quaternion elements
T	Sampling time
t	Slew time
t_0	Time at start of slew manoeuvre
t_h	Time after half the slew is completed
$\mathbf{x}$	Attitude control system states

Chapter 1

Introduction

1.1 CubeSats

Large satellites allow for many functions to be performed on a single platform and they are typically designed to last several years. However, they are costly to develop and launch. Universities and scientific researchers do not have the budget that corporations have. Therefore they need more cost effective satellite missions. This sparked the development of miniaturized satellites. CubeSats are one of these miniaturized satellites and were developed by California Polytechnic State University and Stanford University. CubeSats are classed as nano-satellites or pico-satellites according to their mass. They were initially designed as an educational platform but are now often used in important scientific space research missions. CubeSats have become a common platform for satellite development due to its standardised modular design that utilizes commercial off-the-shelf components. The standard 1U CubeSat is a pico-satellite with a size of $10\,\text{cm} \times 10\,\text{cm} \times 10\,\text{cm}$ and a mass of approximately $1.33\,\text{kg}$. More of these 1U segments can be combined to form larger CubeSats of 2U, 3U and higher that falls into the nano-satellite class. The standardised modular design allows companies to buy components such as an on-board computer or power management module, and easily integrate it into their own platform. This accelerates the development cycle and also allows large quantities of components to be produced for use in satellite constellations or formation flight. The launch of these CubeSats is inexpensive and can be done as a piggy-back module on a larger satellite launch or as a bundle such as the QB50 project where 50 CubeSats, developed by universities around the world, will be launched together in early 2017. These CubeSats will form a constellation that will perform scientific analysis on the lower thermosphere. Usually CubeSats are deployed from a spring-loaded container called a P-POD developed by California Polytechnic State University.

The QB50 satellites will however be deployed from multiple ISIPODs configured in a *StackPack* developed by the Dutch company ISIS [1].

A survey of older CubeSats shows that earth observation is a viable application for CubeSat missions [2]. This survey shows that attitude control is often not very precise in CubeSats with pointing accuracies of typically 2°. The accuracy required by radio communication and solar panel orientation is not very strict and 2° would be sufficient, but for earth observation, improvements are required. Due to the small volume available, imaging with a CubeSat faces large design challenges. However, deployable earth imaging telescopes on CubeSats are becoming reality as shown by Champagne *et al.* [3] and Dearborn *et al.* [4]. These large CubeSats have a larger moment of inertia (MOI) and thus require more torque to perform rapid slew manoeuvres and also require fine pointing accuracy.

1.2 Attitude Control

Current actuators that are commonly used in CubeSats are reaction wheels or momentum wheels alongside magnetic torquer rods. The wheels can provide relatively large torque by transferring momentum of the spacecraft to the wheels in order to perform slew manoeuvres.

1.2.1 Internal Torques

With the total momentum of the system constant, $\mathbf{N} = \dot{\mathbf{h}}$ shows that the external torque applied to the system is zero, where $\mathbf{h}$ is the angular momentum vector and $\mathbf{N}$ is the torque vector. Any moving device within the satellite will therefore only generate an internal torque on the satellite. When a wheel within the satellite is accelerated, its angular momentum increases and, with the satellite being a closed system, the total angular momentum remains constant causing the body to accelerate proportionally in the opposite direction of the wheel.

Momentum wheels developed by the Electronics Systems Laboratory (ESL) at Stellenbosch University have the following specifications [5]:

- Maximum momentum storage of 40 mN m s
- Torque capability of 2.1 mN m
- Peak power usage of 1.8 W with average of 180 mW
- Total mass of 162 g

- Size of $\phi 55\,\text{mm} \times 30\,\text{mm}$

These wheels are for use in large CubeSats and nano-satellites and more specifications can be found in the datasheet that is available in Appendix C. It should be kept in mind that three of these wheels will be necessary for three-axis control.

Schoonwinkel designed a 4-wheel, tetrahedral configured, reaction wheel module for use in nano-satellites that have the following specifications [6]:

- Maximum momentum storage per wheel of $20\,\text{mN m s}$
- Torque capability per wheel of $5\,\text{mN m}$
- Peak power usage of $6.36\,\text{W}$ with average of $2.7\,\text{W}$
- Total mass of $751\,\text{g}$
- Size of $110\,\text{mm} \times 110\,\text{mm} \times 130\,\text{mm}$

This configuration allows for three-axis control with zero angular momentum bias when all wheels spin at the same angular rate. It is difficult to control motors at near zero speed and this configuration allows for the wheels to operate at a bias that will simplify the control. This near zero speed problems are common for reaction wheels and are referred to as zero crossing errors.

Maryland Aerospace has a three-axis control unit that contains 3 reaction wheels. This unit is suitable for large CubeSats and nano-satellites as it is a closed system that can easily be integrated. The specifications from the datasheet as found in Appendix C are as follows [7]:

- Maximum momentum storage per wheel of $9.37\,\text{mN m s}$
- Torque capability per wheel of $0.635\,\text{mN m}$
- Peak power usage of $12.9\,\text{W}$ with average of $4.98\,\text{W}$
- Total mass of $640\,\text{g}$
- Size of $76.2\,\text{mm} \times 76.2\,\text{mm} \times 70\,\text{mm}$

A major advantage of reaction- and momentum wheels are their simplicity that ensures their reliable operation during extended missions.

1.2.2 External Torques

However, the satellite is not a perfectly closed system. There exists external torques that increase or decrease the total angular momentum of the satellite. The first of these disturbance torques is aerodynamic drag. CubeSats commonly operate in low Earth orbits where there are still atmospheric particles present that causes drag on the satellite. If the drag force centre of pressure is not aligned with the centre of mass of the satellite, a torque will be generated. Aerodynamic drag can also be utilized by fins on the satellite to stabilize the attitude. Such fins can even be used to control the attitude of the satellite [8] as shown in Figure 1.1.

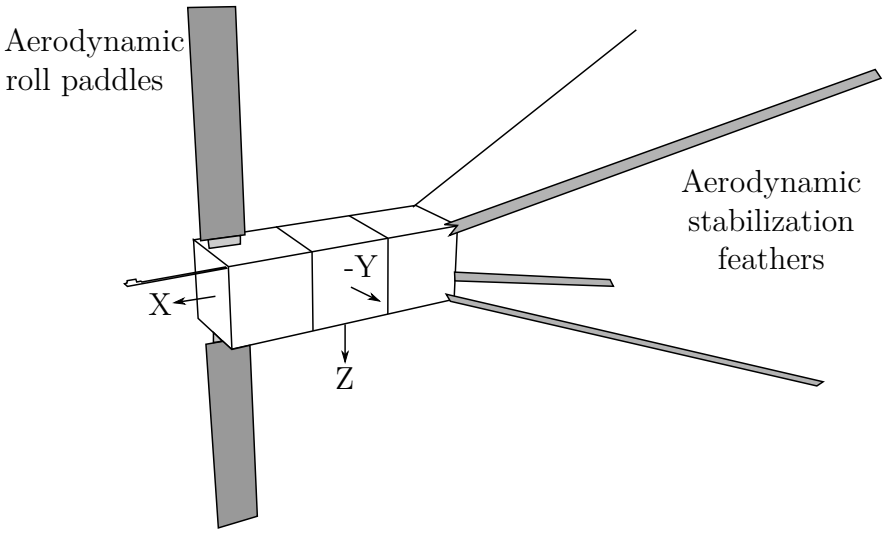

Figure 1.1: Aerodynamic stabilization and control of ZACUBE-2 [9].

The atmospheric drag can also be utilized to deorbit a satellite. This deorbiting is necessary to prevent build-up of space debris that may destroy operational spacecraft. By increasing the satellite surface area after its mission is completed, the atmospheric drag can be increased to allow rapid deorbiting. This rapid deorbiting was to be demonstrated on a CubeSat platform by the deOrbitSail mission [10].

Another force is the gravity gradient on the satellite where sections of the satellite further from Earth experience less gravitational force than the closer sections, causing a torque. In order to stabilize the attitude of a satellite, a large boom can be deployed to utilize the gravity gradient torque as done on SUNSAT [11] shown in Figure 1.2. The boom is typically mounted in the Z-axis of the satellite and will align itself with the nadir axis. If a momentum wheel is added to keep the X-axis directed towards the velocity vector, the spacecraft will make a full rotation around its Y-axis during one orbit period. This creates a stable platform for earth observation.

Even photons from the sun impacting on the surfaces of the satellite produce a

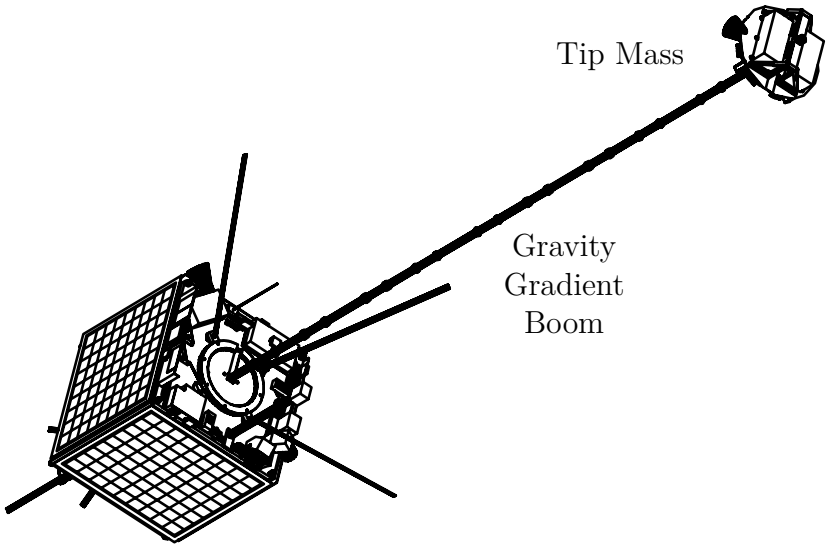

Figure 1.2: SUNSAT with gravity boom deployed [11].

noticeable disturbance torque. This torque is dependent on the area and reflectivity of the exposed surface as well as the distance between the centre of pressure and the centre of mass. This force is utilized by solar sails and may be a viable method to travel within our solar system. A solar sail demonstration mission has been performed by Ikaros [12] for interplanetary travel. Another demonstration for a solar sail mission is planned for 2016 by the CubeSat based LightSail-B [13] which will use solar radiation pressure to change its orbit characteristics.

Another torque that is more noticeable in low Earth orbits is caused by the magnetic field of the earth that couples with any magnetic moment present on the satellite body. The magnetic moment may be caused by residual magnetism in the body frame. This magnetic coupling is often utilized by CubeSats to dump momentum that has built up on the internal wheels by inducing a magnetic moment in torquer rods. Torquer rods are simple electromagnets aligned with the satellite body frame that can provide 2-axis control at any given orbital position. These torquer rods are also utilized to perform detumbling of the satellite during the commissioning phase of the satellite using a B-dot controller [6]. The ESL developed torquer rods [5] for CubeSats shown in Figure 1.3 with a magnetic moment of $0.24\,\mathrm{Am}^2$ that will provide a maximum torque at the earth's magnetic poles of approximately $11.5\,\mu\mathrm{N\,m}$. It is at the earth's magnetic poles where the geomagnetic field is the strongest. This geomagnetic field can be measured using the magnetometer or estimated from an orbit propagation model. The datasheet for these torquer rods are available in Appendix C.

Thruster propulsion can provide large external torque and may greatly increase the capabilities of CubeSats, but is not commonly used due to volume and mass restrictions.

Figure 1.3: ESL magnetic torquer rod [5].

Large propellant tanks are needed for conventional butane propulsion, but electric plasma propulsion can be an option for satellites that have an ample power source. The exhaust from propulsion systems pollute the environment close to the satellite and may reduce imaging capabilities. Propulsion systems have been analysed in [14] and it is concluded that the complexity and cost currently involved in the CubeSat development of such systems make them unsuitable for universities and small companies.

1.3 Control Moment Gyroscopes

The restrictions on CubeSats call for a minimum power and volume actuator that can still provide a large internal torque. Control Moment Gyros (CMGs) are well suited for this task. When a rotation vector is applied perpendicular to the spinning axis vector of a object, a torque is generated perpendicular to both of these vectors. This is referred to as gyroscopic precession. The reverse is also true where a torque applied perpendicularly to the axis of a spinning object results in a rotation that is perpendicular to both these vectors and is called torque induced precession. This effect is visible in the directional change of a gyroscope's spin axis when its centre of mass is misaligned with its pivot point, as illustrated in Figure 1.4 for a spinning top toy. The torque in this example is caused by the gravitational force. Free nutation is also present and in practice the spin axis will wobble at a rate proportional to that of the spin rate. This free nutation is further explained by Butikov [15]. The gyroscopic precession is utilized by a CMG to provide large torque amplification. A simple CMG consist of a flywheel mounted in a frame called a gimbal that is actuated to produce the commanded slew torque. The torque generated by a CMG is given by,

$$\mathbf{N}_{\text{generated}} = \dot{\boldsymbol{\delta}} \times \mathbf{h} \tag{1.1}$$

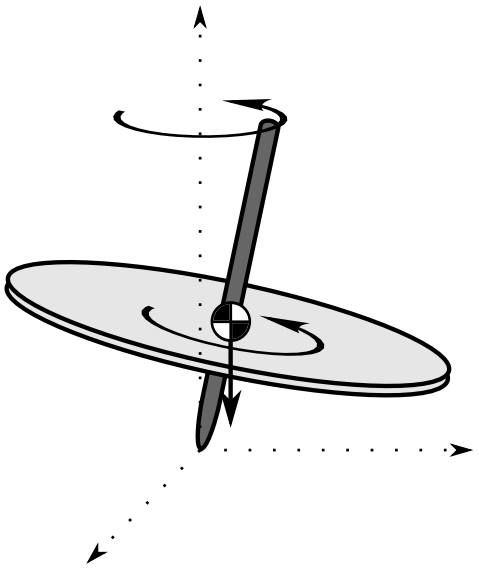

Figure 1.4: Spinning top toy.

Where $\mathbf{N}_{\text{generated}}$ is the generated torque vector, $\dot{\boldsymbol{\delta}}$ is the gimbal angle rate vector and $\mathbf{h}$ is the angular momentum vector of the flywheel. The angular momentum of the flywheel is its angular rate, ω_{f}, times the moment of inertia (MOI), I_{wheel}, around its spin axis.

1.4 CMG Technology

The use of gyroscope technology prior to space exploration included the stabilization of large naval vessels, monorail trains, weapon sights for large tank guns and aircraft guidance systems. The gyroscopic effect allowed large military ships to perform agile manoeuvres during combat using flywheels with a constrained roll axis. When a gyroscope is prevented to precess while a disturbance torque is applied, it will reject that torque. Modern cruise ships use massive CMGs to keep the ship level during stormy weather and during a sharp course adjustment [16]. The benefit of using gyroscopes over hydrodynamic fin stabilization is that no forward motion is required.

Gyroscopic stabilization has been used in early satellites where the entire satellite spins around a body axis to provide stability. A spinning satellite will always precess to spin around the axis with maximum inertia in order to minimize the kinetic rotational energy, as was found with the Explorer-1 mission [17] where flexible parts on the satellite caused a dissipation of energy. A part of the spinning spacecraft can be despun to keep it stable for RF communication and earth imaging. Modern satellites are also often slow spinning to keep the temperature on the outside panels uniform, but

they rely on internal momentum wheels to provide gyroscopic stability.

CMGs allow for the utilization of the gyroscopic torque and are commonly used in large spacecraft to perform large angle slew manoeuvres. The simplest configuration of only a single flywheel and gimbal is referred to as a Single Gimbal CMG (SGCMG) as shown in Figure 1.5. This configuration provides a torque in the plane normal to the

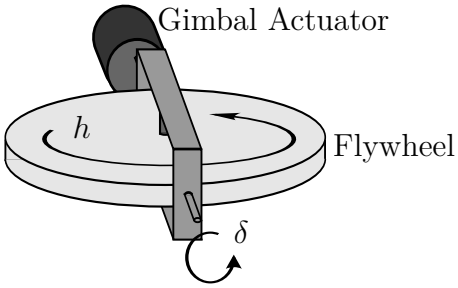

Figure 1.5: SGCMG.

gimbal axis. To achieve full three-axis control, a minimum of 3 SGCMGs are needed. The major drawback of a system with only 3 SGCMGs is the presence of singularity points. This is when a commanded torque vector cannot be generated by any gimbal rotation. This situation is also known as gimbal lock. Many steering laws have been developed to avoid singularity situations such as seen in [18]. More SGCMGs can be combined to provide redundancy to escape singularity situations. The MIR space station used 6 parallel mounted SGCMGs that was fully singularity robust. If any CMG failed in this configuration, three-axis control was still possible.

Previous SGCMG design and testing was done by Berner [19] from Stellenbosch University that had a maximum torque capability of 52.3 mN m but was far too large and heavy for CubeSat use.

A novel modular SGCMG has been developed by Honeybee Robotics that can provide immense torque using a very small volume as seen in in the following specifications [20]:

- Maximum momentum storage per CMG of 56 mN m s
- Torque capability per CMG of 112 mN m
- Peak power usage of 2 W with average of 1.5 W
- Total CMG mass of 600 g
- Size of 48 mm×48 mm×91 mm

The datasheet for these SGCMGs can be found in Appendix C. These SGCMG units can be combined in any configuration that a satellite mission may require. Unfortunately the mass of one of these SGCMG is almost half the mass allowed for a CubeSat.

The pyramid configuration shown in Figure 1.6, as described in [18], is a well-known configuration that has minimal singularity directions with only 4 SGCMGs and can provide full three-axis control. Nagabhushan and Fitz-Coy developed a pyramid

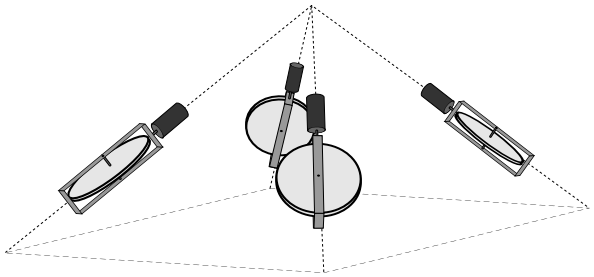

Figure 1.6: Pyramid array of SGCMGs.

SGCMG array shown in Figure 1.7 used in SwampSat with the following specifications [21]:

- Maximum momentum storage of 0.8 mN m s
- Torque capability per CMG of 0.8 mN m
- Peak power usage of 3 W
- CMG mass of 437 g
- Size of 100 mm×100 mm×50 mm

This design proves the feasibility of using complex CMG based designs in CubeSats. However, a disadvantage of this design is that it takes up half the volume of a 1U CubeSat.

Another configuration is the mounting of the SGCMG inside another gimbal. This is referred to as a Dual Gimbal CMG (DGCMG) as shown in Figure 1.8 and allows for full three-axis control. The singularity avoidance of this configuration is simpler due to the extra degree of freedom that the additional gimbal provides. This configuration is also more compact than a pyramid array of SGCMGs. The extra gimbal does, however, add more mechanical complexity to the design and increase the probability for failure to occur. Three orthogonally mounted DGCMGs were used in the NASA Skylab and a two pair parallel mounted configuration is used in the International Space Station (ISS). Both these configurations are singularity robust and do not require complex steering laws.

Figure 1.7: SwampSat's pyramid configured SGCMGs [21].

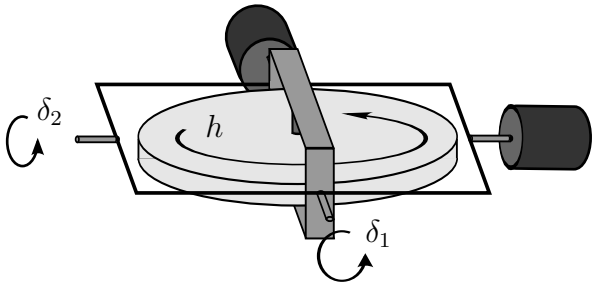

Figure 1.8: DGCMG.

DGCMGs have not yet been used in CubeSats, but with miniature motor technology, it may be a compact solution.

1.5 Overview of Thesis

This thesis follows the development of a novel DGCMG based actuator for use in CubeSats. This actuator is designed to improve upon existing CMG technology. The mechanical design is small in size and mass and requires minimum power to operate. Motor driver selection and testing was done to find the most suitable drivers for the wheel motors and gimbal actuators. Electronics were designed to control the motors, communicate with sensors and interface with a computer. Attitude controllers were implemented and used in simulations to compare with Hardware-in-the-Loop tests. Test results were compared with conventional reaction wheel results.

1.5.1 Specifications

A satellite at an altitude of 500 km will have an orbital velocity of about 7.62 km/s. To track a stationary ground based target, the satellite must be able to rotate at

$0.873\,°/s$. This agile manoeuvrability is required for future earth observation CubeSat applications which will track ground based targets. Agile slew manoeuvrability for a satellite has been defined as 1-10 °/s by [22]. This DGCMG must be able to perform such an agile slew for a 3U CubeSat with a maximum inertia axis of about $0.0333\,\mathrm{kg\,m^2}$.

From Newton's rotation laws, the torque required to do a 30° slew in 10 s for such a satellite can be calculated as approximately $0.7\,\mathrm{mN\,m}$ from (1.4). This will give an agile average angular rate of $3\,°/s$.

$$\ddot{\theta} = \frac{N}{I} \tag{1.2}$$

$$\dot{\theta} = \frac{N}{I}t \tag{1.3}$$

$$\theta = 0.5\frac{N}{I}t^2 \tag{1.4}$$

Where N is the maximum torque, I is the maximum MOI, θ is half of the slew angle and t is half the slew time. This equation applies the maximum acceleration for the initial half the slew and then the maximum deceleration for the latter half. This slew rate will only be possible for such a large angle manoeuvre if the acceleration can be applied throughout the initial half of the slew. This would indicate a momentum transfer capability of $3.5\,\mathrm{mN\,m\,s}$. Without this, the slew can only be completed if the satellite is allowed to rotate at a constant angular rate before decelerated when nearing the required angle. The control logic for this will be explained later in Chapter 3.

From the existing CMGs designed for CubeSats and the reaction wheels that are commercially available as discussed previously, as well as the calculated torque required for agile manoeuvres, the following specifications can be used that will provide significant improvement for use in future nano-satellite missions:

- Torque capability per axis of $0.8\,\mathrm{mN\,m}$. This will provide agile manoeuvrability.
- Maximum momentum storage of $1\,\mathrm{mN\,m\,s}$ per axis. This value is low to allow the gimbals to only operate within a small angle range that will decrease the volume of the design. This will simplify the hardware design as discussed in Section 2.3.
- Peak power usage of 2.5 W with average of 0.5 W. This power usage specification is strict, because this is the obvious advantage CMGs should provide over reaction wheels. This specification will be refined in Section 2.4.6 when the power of the electronic components are evaluated.
- Size of $50\,\mathrm{mm}\times50\,\mathrm{mm}\times100\,\mathrm{mm}$ ($\frac{1}{4}$U). This size constraint is as an attempt to improve upon the size specification of Nagabhushan [21].

- Total mass of 300 g. The mass of a 1U CubeSat may not exceed 1.33 kg and for the size constraint set at $\frac{1}{4}$U, the same ratio of mass would be 333 g.

This specified torque value can be divided by the actuator power usage, the mass or the volume, to provide efficiency ratings. This will allow for different actuators to be compared in Chapter 5 of this thesis. With these specifications, the proposed actuator will have an output torque versus input power efficiency rating of $\eta_P = 3.20 \times 10^{-4}\,\mathrm{Nm/W}$, an output torque per mass efficiency of $\eta_M = 2.7 \times 10^{-3}\,\mathrm{Nm/kg}$ and an output torque per volume of $\eta_V = 3.2\,\mathrm{Nm/m^3}$.

Chapter 2

System Design

This chapter details the design of the proposed attitude control actuator for use in CubeSats. The design process will consist of mechanical and electronic development.

2.1 DGCMG Configuration

The DGCMG configuration proposed in this thesis is similar to that used in the ISS where two pairs of DGCMG are mounted in a parallel configuration and their gimbal angles are controlled to rotate at equal but opposite angles. Wie analysed a similar configuration in his book, consisting of parallel mounted SGCMGs [18]. Steyn also simulated a *Near-Minimum-Time* controller on parallel mounted and scissor pair controlled SGCMGs [23]. The term 'scissor' is used throughout this thesis to indicate that the two gimbals rotate with the same angle magnitude, but in opposite directions. The DGCMG configuration developed in this thesis consists of a symmetric pair of counter rotating flywheels (rotate at equal speed, but opposite directions). These flywheels are each mounted in a dual gimbal framework. The outer gimbals scissor with the use of gears and a single motor. Each inner gimbal has a motor and are configured by the circuitry to also scissor. This ensures that corresponding gimbals of each flywheel have equal angle magnitude, but with opposite direction at all times.

2.1.1 Benefits and Disadvantages

This configuration will allow the flywheel combination to have zero total angular momentum at zero gimbal angles while each still maintains a non-zero angular rate. The non-zero angular rate is important due to the difficulty involved in controlling a motor at low RPM.

With deployable payloads, the usefulness of a CubeSat greatly increases, but so does the complexity of the attitude control. When the CubeSat is launched, the MOI is much smaller than after the sails, booms, solar panels, antennae or telescopes are deployed. The attitude actuator should have enough torque capability to perform agile large angle slew manoeuvres with the large MOI. With the small MOI at the start, there is the risk the system will become unstable, if too large torque is used during manoeuvres. With the proposed DGCMG configuration, the nominal wheel speed can be kept low after launch to perform manoeuvres with low torque and increased when the deployables are released.

In order to have additional control capability, the flywheel rates can be variable to supply a nett angular momentum to the satellite. This configuration will then allow for three-axis control and a large redundancy factor. When a flywheel motor fails, there will still be a DGCMG available to perform limited three-axis manoeuvres. This will, however, require an entirely new attitude controller that has a singularity avoidance steering algorithm. If the outer gimbal actuator fails, limited two-axis control will still be possible. If any of the inner gimbal actuators fail, the corresponding flywheel can be turned off to conserve power and the remaining DGCMG can be used to perform three-axis manoeuvres. If insufficient power is available on the satellite, one of the inner gimbal stepper motors and its corresponding flywheel can be deliberately disabled. These mitigation strategies for potential failures are essential, but they all sacrifice the zero momentum bias advantage of the scissored pair.

A major disadvantage of the configuration is the mechanical complexity. As with any satellite component design, the risk of failure increase with the increase in complexity. To manufacture this design with precise alignment and tight tolerances will be difficult. This design includes the use of bearings, gears and several motors. The motors are connected to the controller boards via flexible wires that will have to withstand the long term motion of the gimbals. The mechanical structure will have to survive the forces and vibrations involved during launch and withstand the vacuum environment and large temperature fluctuations of space.

2.2 Motors

The motors considered for use as actuators in the DGCMG configuration are stepper, brushed and brushless direct current motors. Magnetic suspension of the rotating flywheels, as done by Zheng [24], has been investigated, but would be overly complex and impossible to implement at low power on a CubeSat.

2.2.1 Stepper Motors

Stepper motors consist of a rotor that has a large quantity of teeth with alternating magnetic polarity. The rotor is surrounded by the stator which consists of electromagnetic coils that are switched in alternation to align the teeth with each coil in sequence. The more teeth present on the rotor, the finer the accuracy of the rotations will be possible. Figure 2.1 show the internal structure of a stepper motor where B coils are powered and the rotor teeth are aligned with the teeth on the B stator.

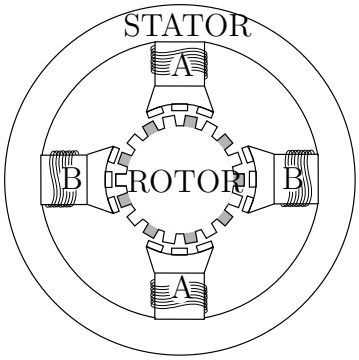

Figure 2.1: Internal structure of stepper motor.

The stepper motor coils require relatively large current that can be provided by an H-bridge as shown in Figure 2.5. Stepper motors were chosen to actuate the gimbals in the DGCMG design. The motivation for this choice was primarily due to the ease of controlling the motor in open loop configuration to a specified angle with good accuracy. The torque these motors can achieve is high and they do not have brushes that may wear in the vacuum of space. The stepper motors used in the DGCMG design is the AM0820-V-5-56-08 with 08/1 64:1 planetary gear-head from FAULHABER [25]. This combination uses sintered and sleeve bearings, but vacuum rated versions with ball bearings are available. One of the stepper motors is shown in Figure 2.2.

Figure 2.2: FAULHABER stepper motor with gear-head.

The datasheet for these stepper motors can be found in Appendix C and show that the step resolution is 18°. With the gear-head, the step resolution becomes approximately 0.28°. The step resolution will not influence the magnitude of the torque that will be generated, but will cause the torque to be applied for a longer or shorter duration than required. The stepping rate resolution will influence the torque resolution.

2.2.1.1 Stepper Motor Drive Sequence

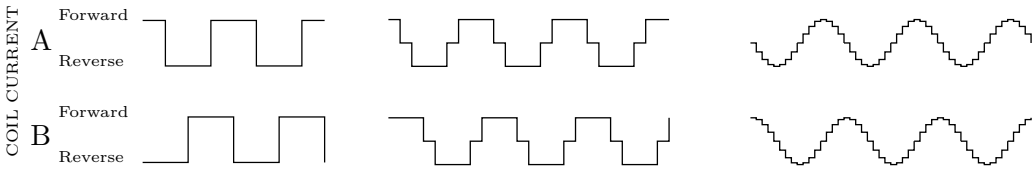

(a) Full-step mode. (b) Half-step mode. (c) Micro-step mode.

Figure 2.3: Stepper motor modes of operation.

The FAULHABER stepper motor is a bipolar type and therefore required two H-bridges. The sequence of forward and reverse pulses provided to the stepper coils are determined when transistor switches are opened or closed. The stepping of the motor can be done in either full-, half- or micro-step modes. Figure 2.3a shows the waveforms of the coil current for the full-step mode. This mode uses the least power as only one coil can be powered at any given moment. This will also provide a stepping resolution of 360° divided by the rotor teeth quantity. With half-step mode shown in Figure 2.3b, the resolution is halved as the rotor teeth can be controlled to a position between the two coils when they are both powered. Micro-stepping is a technique used to smooth the rotation of the motor to reduce noise and vibrations by providing the coils with a nearly sinusoidal waveform that are 90° out of phase as shown in Figure 2.3c. It is however difficult to use a normal H-bridge to generate such a waveform and the torque is greatly decreased. The resolution may increase with micro-stepping, but the accuracy decreases due to the reduced holding torque. A hybrid method may be used where micro-stepping is used during rotation, but the final step will always land on a full-step. This will provide the benefit of smooth rotation, reduced resonance and high holding torque. When the coils are then switched off, the permanent magnets provide the holding torque and the power usage will be very low.

2.2.2 Brushed Direct Current Motors

Traditional brushed DC motors are used as actuators in many earth based applications due to their low cost and simple implementation. Brushes are used to carry current

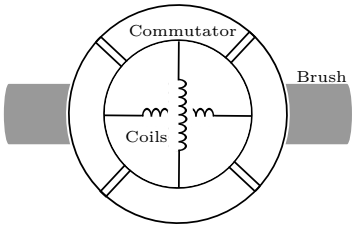

Figure 2.4: Commutation of brushed DC motor.

to the coils located on the rotor by a component referred to as the commutator as illustrated in Figure 2.4. Brushed DC motors can be driven by a simple H-bridge circuit, as seen in Figure 2.5, to supply enough current to the coils. The microcontroller is incapable of supplying such large currents. The main disadvantage of these motors is the wear of their brushes with prolonged use. This wear is even more profound in the harsh environments of space where the vacuum environment does not allow for conventional lubricants. Brushed motors may however be used on low lifespan satellite missions where they are much more cost efficient and simpler to integrate.

2.2.2.1 H-Bridge

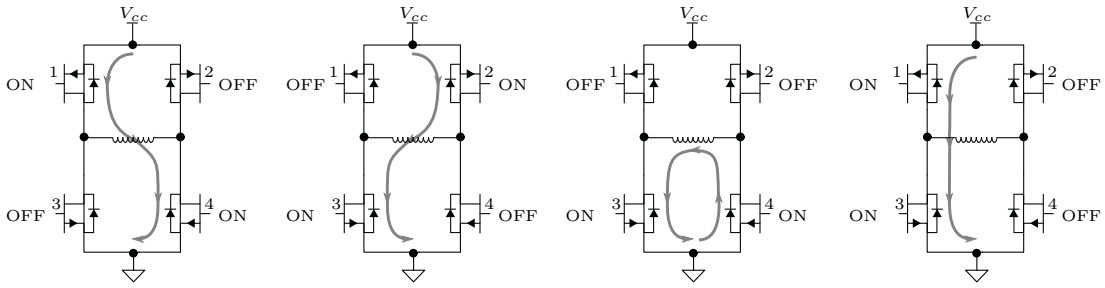

(a) Forward mode. (b) Reverse mode. (c) Brake mode. (d) Shoot-through.

Figure 2.5: Full H-bridge operation modes.

A full H-bridge consists of four drive transistors, typically MOSFETS as seen in Figure 2.5. The transistors can be switched by logic from a microcontroller to provide power to the coil in reverse and forward direction. The transistors can be simplified as switches where 1 and 4 are closed, and 2 and 3 are open to allow current to flow in the forward direction through the coil as seen in Figure 2.5a. With 2 and 3 closed, and 1 and 4 open, current will flow in the reverse direction as seen in Figure 2.5b. With all the switches open, the motor will continue to rotate within a vacuum environment and only the brushes and bearings will provide rotational resistance. This is not a good method of braking the motor if implemented on a momentum or reaction wheel due to the slow deceleration. When switches 1 and 2 or 3 and 4 are closed, the motor coil will

be shorted as seen in Figure 2.5c. The back electromotive force (EMF) in the motor coil will cause current to flow in the opposite direction through the coil and cause the motor to brake quickly. The motor coil and drive transistor must be able to handle this high current flow. Situations where 1 and 3 or 2 and 4 are closed simultaneously must be avoided as this shorts the power supply and is known as shoot-through as seen in Figure 2.5d. The control logic of the H-bridge must take into account the transistor's on and off time delays to ensure that switch 1 is completely off before 3 is activated.

2.2.3 Brushless Direct Current Motors

As the name implies, brushless DC motors (henceforth referred to as BLDC motors), do away with brushes. The rotor in this case consists of permanent magnets with the electromagnetic coils located on the stator. In order to determine which coil needs to be powered, an electronic commutator is necessary. This commutation is done by advanced drivers that may use the back EMF or dedicated Hall effect sensors to measure the current position of the rotor magnets. With the position of the rotor known, the driver can power the coil required for rotation. The BLDC motor driver consists of a half-bridge for each phase of the motor and digital logic for commutation. The half bridge consists of transistors 1 and 3 in Figure 2.5 and is used to switch the coil input between the supply voltage (to power the coil) and ground (to switch off the coil). A simplified example of a BLDC motor with driver is shown in Figure 2.6.

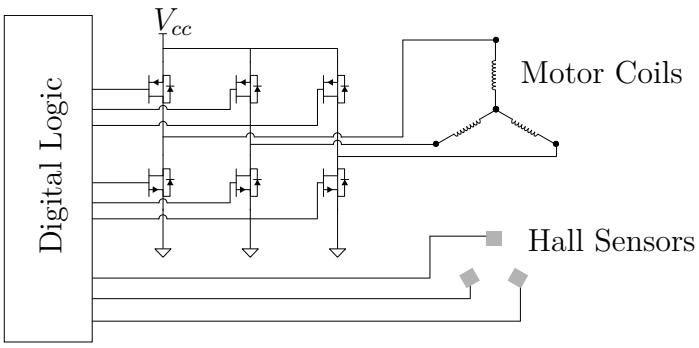

Figure 2.6: Half bridge drive of BLDC motor.

BLDC motors are more reliable and provide higher torque than brushed DC motors and are commonly used in modern satellites' momentum- and reaction wheel designs. In order to accelerate the flywheels to the required angular velocity, BLDC motors are used for this DGCMG design. The BLDC motors used are 1509-006-B Flat BLDC Micromotors from FAULHABER as shown in Figure 2.7. The datasheet for these BLDC motors are available in Appendix C. They are also available with vacuum rated bearings [25] and have been flight tested in various CubeSat missions [5]. The vacuum

rating has been sufficiently tested and the flight heritage confirms the durability of these motors.

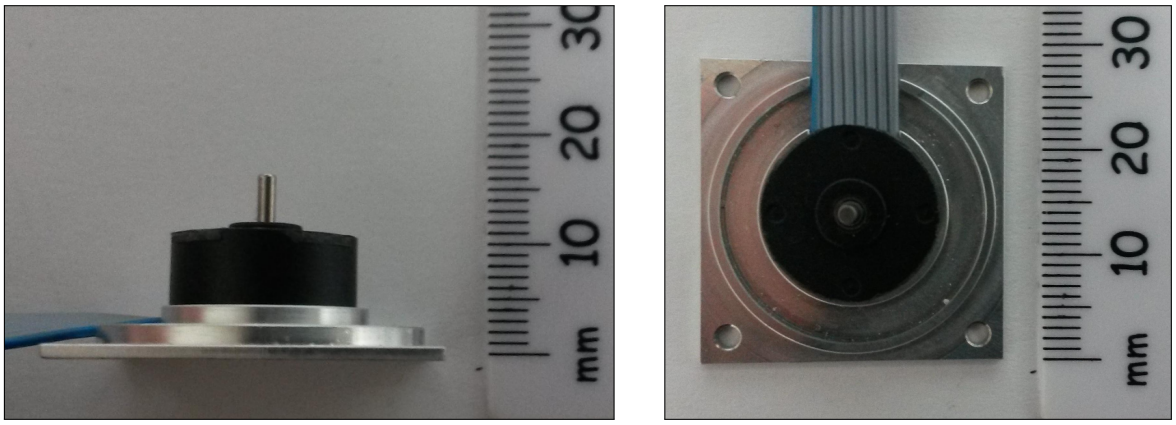

(a) BLDC motor side view.

(b) BLDC motor top view.

Figure 2.7: FAULHABER BLDC motor on mounting plate.

2.2.3.1 Back Electromotive Force

Back electromotive force (EMF) is the result of the Faraday law of induction where the rotating coils in the magnetic field of the motor produce a voltage opposing the applied voltage. This back EMF is directly proportional to the rotation rate of the motor and can be measured by the analogue to digital logic of the driver.

2.2.3.2 Hall Effect Sensors

The Hall Effect relies on the Lorentz force where a charge carrier experiences a force when it travels through a magnetic field. The sensor consists of a constant current flowing through a semiconductor that is located between two conductive plates. When a magnetic field is introduced, the charge carriers are forced towards one of the plates and a voltage can then be measured across these plates. Hall sensors can be integrated into a BLDC motor design where the permanent magnets on the rotor pass the sensors on the stator and send a voltage pulse to the digital logic of the driver.

2.3 Mechanical Design

The use of 3D printing technology simplified the mechanical design process. This allowed for several concept models to be built before a final mechanical model was manufactured. The 3D printing was done with low cost ABS plastic. This did not

provide the accuracy and rigidity demanded for the tests performed on the model. The final mechanical model was manufactured from 7075 Aluminium alloy due to its high strength, low density and low thermal expansion compared to standard 6061 Aluminium alloy.

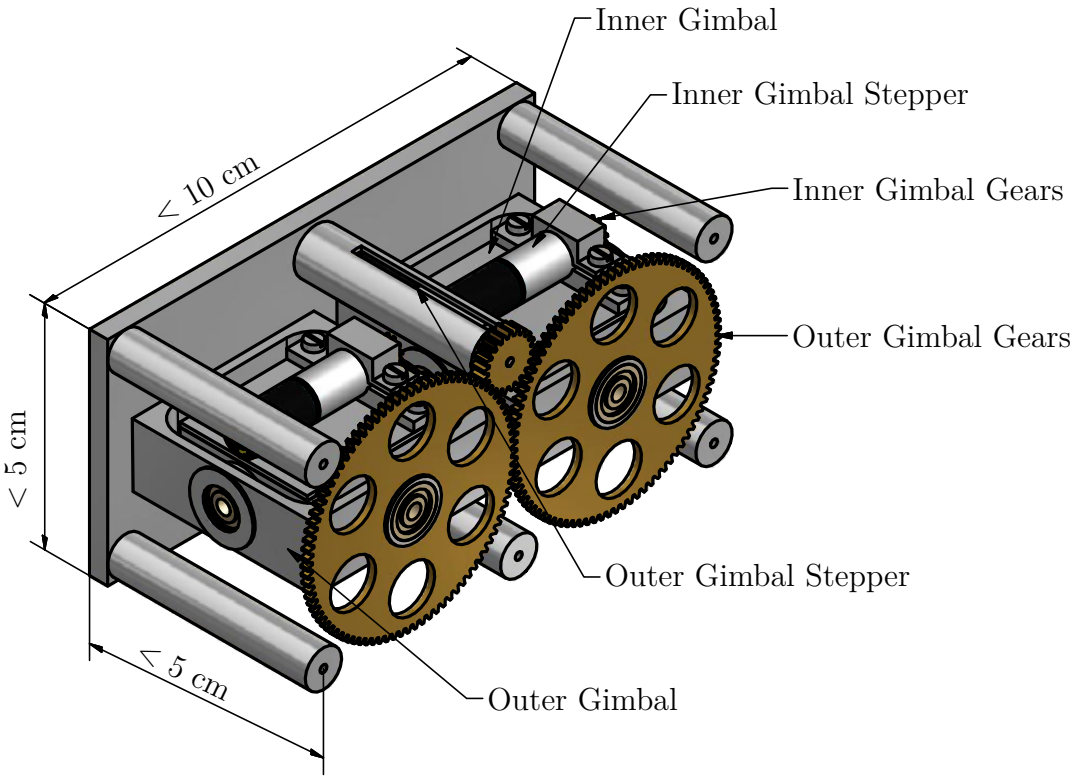

Figure 2.8: Mechanical design of scissored DGCMG pair.

Figure 2.8 show the final mechanical design with the motors mounted in place. Notice that the outer gimbal motor is mounted in a tube that is fixed to the frame of the design. The inner gimbal stepper motors can be seen fixed to the top of each inner gimbal casing. Their drive shaft gears are meshed with gears that are fixed to the outer gimbals. The BLDC motors with their flywheels shown in Figure 2.9a and 2.9b are enshrouded by the inner gimbal casing as shown in Figure 2.9c. Without any of the wiring and electronics, this design will fit inside a volume of $10\,\text{cm} \times 5\,\text{cm} \times 5\,\text{cm}$. The completed model is shown in Figure 2.10 from various views, but more detailed design schematics can be found in Appendix D.1. The weight of the mechanical design is measured as 292 g with the motors included, but can be easily reduced to 260 g, if material is removed from the frame. Even more material can be removed if strength analysis is done to ensure that no rigidity is lost. With the new mass value defined, the efficiency value in Chapter 1 will increase.

In Chapter 3, the calculations determined that the maximum momentum storage

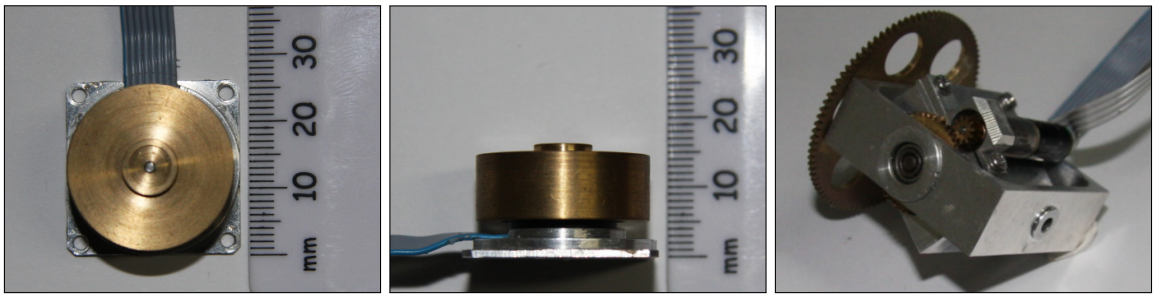

(a) Flywheel on motor, top view. (b) Flywheel on motor, side view. (c) Single DGCMG assembly with inner gimbal.

Figure 2.9: Mechanical DGCMG design with flywheels.

will be at gimbal angles of ±90°. Therefore continuous gimbal rotations are not necessary and the angle range can be limited. This will circumvent the requirement for slip-rings to carry electrical signals to the gimbal- and flywheel motors. Slip-rings are used in CMG designs when continuous rotation of the gimbals is allowed.

This range of rotation requires a carefully designed flexible harness. This harness consists of multi-core wires in a ribbon cable. These are routed to allow flexing to occur over a large radius as seen in Figure 2.10. The plastic insulation of this ribbon cable is very stiff. This create the risk that the wires can easily sever from the delicate pads of the stepper motors. Therefore the maximum gimbal angle is chosen as ±25° where little stress is exerted on the wires. Chapter 3 discuss future improvement that can be made in the cable design.

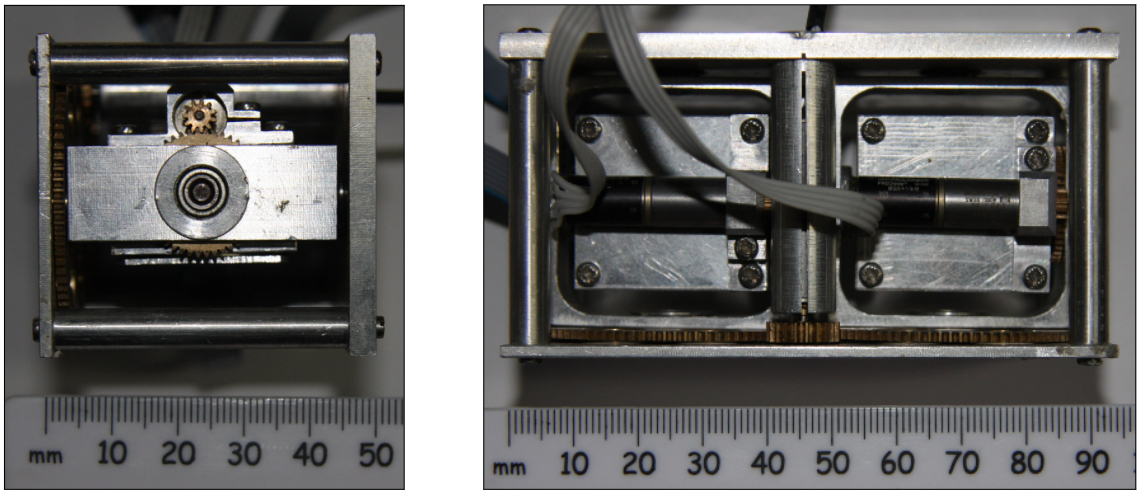

(a) DGCMG side view. (b) DGCMG top view.

Figure 2.10: Complete mechanical DGCMG design.

2.3.1 Gear Design

The outer gimbals are geared with each other to enable scissoring. One of the gimbal axis gears is also meshed with the drive gear of a single stepper motor. Figure 2.11a shows the layout of the outer gimbal gears. For the inner gimbals, two separate stepper motors are used. Each of these stepper motor drive shafts is geared with their respective gimbal axis as seen in Figure 2.11b. Involute gear teeth are used with pitch circles optimized to have the least amount of backlash and still maintain low friction.

Cold welding and galling should be considered whenever metal surfaces come into contact in vacuum environments. Expansion and contraction from large temperature fluctuations may increase abrasion during gimbal rotations. For this reason brass was chosen as the gear material due to its resistance to mechanical abrasion and cold welding. Materials such as plastic and oil based lubricants evaporate in low pressure environments in a process referred to as outgassing. Outgassing of lubricants pose a friction issue and therefore the brass gears are manufactured with a diamond cut finish in order to achieve a highly smooth surface between teeth reducing the need for lubricant.

At the relatively low $0.17\,\mathrm{rad\,s^{-1}}$ speed of gimbal rotation, the minute friction still present can easily be overcome by the $20\,\mathrm{mN\,m}$ torque of the stepper motors. The stepper motors have resolution of 18° per step. Each stepper also has a built-in gearbox with a reduction ratio of 64:1. The reduction ratios of the outer and inner gimbal gears are 90:21 and 46:11 respectively. Therefore, the gimbal angle resolutions are 0.066° and 0.067°. The steppers have an angular accuracy of ±10% of their step size. The gearboxes have ±1.5° in backlash and the gimbal gears have a measured backlash of ±0.5°. This backlash may cause a gimbal deviation of up to 0.896°. In practice, the flywheels act as gyroscopes and require a torque from the stepper motors to rotate them. Therefore the backlash does not produce a large gimbal angle deviation. However, any flywheel imbalance causes the gimbals to rattle in the ±0.896° range, where the stepper holding torque does not constrict it. To balance the small wheels, specialized machinery is required, but this was unavailable for this design.

The gears and the frame that they are mounted on are constructed of different material and will experience different thermal expansion with the extreme temperature fluctuations encountered by CubeSats. The linear thermal expansion coefficient for Brass and Aluminium is respectively $19\,\mathrm{\mu m\,m^{-1}\,°C^{-1}}$ and $23.6\,\mathrm{\mu m\,m^{-1}\,°C^{-1}}$. The outer gimbal gears have the longest spacing between their axes and will have the largest expansion difference. From these coefficients, and the temperature range of $-20\,°\mathrm{C}$ to $80\,°\mathrm{C}$, it is calculated that the largest mesh deviation of the gear teeth will be $12.5\,\mathrm{\mu m}$.

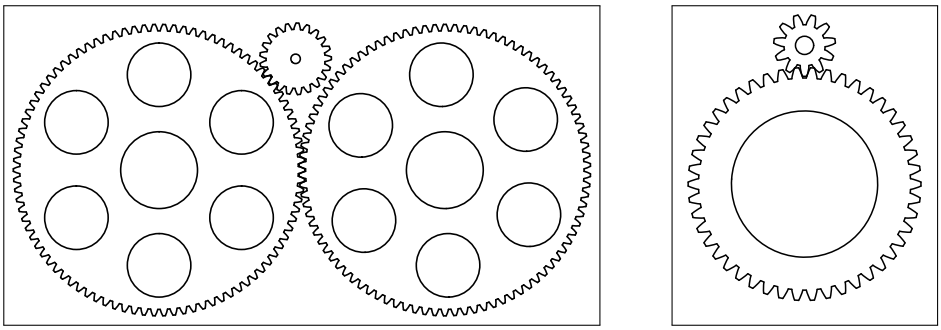

(a) Outer gimbal gears. (b) Inner gimbal gears.

Figure 2.11: Gear layout.

This value is only slightly larger than the manufacturing tolerances of 5 µm and will be even smaller for the inner gimbal gears and can safely be ignored.

2.3.2 Flywheels

In Chapter 1 the torque specification was chosen as 0.8 mN m. The maximum gimbal rate is calculated from the maximum stepper rate to be approximately 0.17 rad s^{-1}. With this information, and (1.1), the angular momentum of a single flywheel can be calculated as 2.4 mN m s. The BLDC motor can operate up to 16000 RPM, but with a flywheel mounted, the slightest misalignment will cause vibration that will damage the motor. With experimentation, the maximum safe speed is found to be 10000 RPM. The flywheel speed should have large range for Z-axis slews, but still maintain a high nominal speed for CMG operation. Therefore the nominal speed is chosen as 8000 RPM. At this speed the flywheel should have a MOI of 2.8 mg m^2. With its high density of 8.47 g cm^{-3}, brass is a suitable material for the manufacturing of the flywheel. This will allow for a high MOI at lower volumes. Figure 2.12 shows the dimensions of a flywheel that is mounted on one of the BLDC motors. The flywheel and motor combination was already available and has been used on reaction wheels manufactured by the ESL as mentioned in Chapter 1.

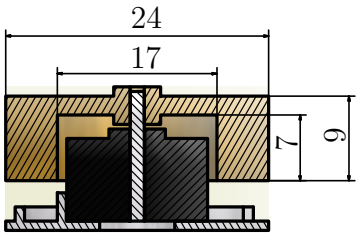

Figure 2.12: Flywheel dimensions.

The moment of inertia of these flywheels can be calculated as follows:

$$\begin{aligned} I_{zz} &= \frac{1}{2}M_1R_1^2 - \frac{1}{2}M_2R_2^2 \\ &= \frac{1}{2}\left(d\pi R_1^2 H_1\right)R_1^2 - \frac{1}{2}\left(d\pi R_2^2 H_2\right)R_2^2 \end{aligned} \tag{2.1}$$

Where d is the brass density, R_1 is the flywheel outer radius of 12 mm, R_2 is the flywheel inner radius of 8.5 mm and $H_1 = 9$, $H_2 = 7$ is the flywheel height. With these values the MOI is calculated as 1.99 mg m^2 and the mass was calculated as 21 g. The actual mass was slightly less and would indicate that the density differs or the volume measurement inaccurate. Therefore, the MOI was adjusted to 1.98 mg m^2. The rotor of the BLDC motor increases the MOI to 2.05 mg m^2. This MOI is slightly less than the required 2.8 mg m^2 and will allow for a maximum torque of 0.58 mN m. Therefore, the system will be less power efficient, less mass efficient and less volume efficient.

2.4 Electronics Design

Electronic circuitry must be able to receive commands from a PC or satellite onboard computer (OBC) or ADCS OBC and translate those commands to pulse width modulation (PWM) signals for the BLDC motor drivers or provide pulses for the stepper motor drivers. The design should allow for volume constraints and have minimal power losses. For the testing of the DGCMG capabilities, the electronics must also be able to receive angular rate measurements from sensors and send it to the PC based controllers.

2.4.1 Sensors

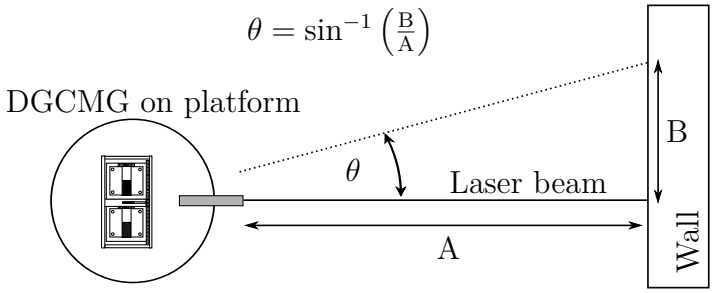

Figure 2.13: Laser slew angle determination.

The inertial rate measurements will be provided by a MEMS inertial measurement unit, ADIS16375, from Analog Devices. This unit will provide rates that can be integrated to find the rotation angles. The rate measurements are dependant on the

ambient temperature and therefore the ADIS16375 is calibrated before each test by placing the sensor on a stationary surface and measuring the rates. The measurements showed a significant drift after approximately 10 minutes. Therefore, the rates are measured for the last minute before the test is performed to minimize the influence of this drift. The mean is found of these rates and is subtracted from the measurements acquired during the test. To confirm the slew angles, a laser diode is added to the design which can be pointed to a wall. The distance of the test setup from the wall is known and the travel by the laser diode aim point can be measured to determine the angle of the slew as shown in Figure 2.13. The laser was used during slew rotations of 30° and verified the rate sensor gain as specified in the datasheet. During space flight, MEMS measurements will be available along with sun and nadir measurements. Therefore, the rates and absolute rotation angles will be available and will allow for more accurate slew control.

2.4.2 BLDC Motor Drivers

All drivers considered had to be able to operate from a 8 V power supply in order to be compatible with as wide as possible variety of commercially available CubeSat Electrical Power System (EPS) units as surveyed by Burt [26]. The driver had to be robust against over-current and tolerate the large temperature range of −20 °C up to 80 °C in space. The total PCB area occupied by the driver and its supporting components had to be kept at a minimum.

2.4.2.1 BA6859AFP-Y

The BA6859AFP-Y from ROHM requires few supporting components and operates between 3 V and 14 V, but the package itself is 13.6 mm × 7.8 mm in size. Additional features of this integrated circuit (IC), is current limiting, rotation direction detection and prevention, true sinusoidal drive as well as multiple brake modes. A problem with this driver is that the rotation direction cannot be changed and that an analogue input is required to regulate the speed. This analogue input can be achieved by low pass filtering the PWM output of the microcontroller, but will require an additional resistor and capacitor. When the motor current is switched off, the flywheel will decelerate very slowly due to the low friction in the vacuum environment and therefore the brake feature is required to perform fast speed control.

2.4.2.2 L6235D

The L6235D from ST Micro has a recommended voltage range from 12 V to 52 V, but was found during tests to operate from as low as 8 V. This IC is fairly large at 15.4 mm × 10.3 mm and also requires an analogue signal for speed control. Additionally, it has space heritage, over-current protection, thermal shutdown and a brake feature.

2.4.2.3 A4915

The A4915 from Allegro is an IC that serves as a pre-driver. This driver requires the drive transistors seen on the right in Figure 2.14 and will therefore require larger surface area on the PCB although the IC itself is only 5 mm × 5 mm. The benefit of this design is that the drive electronics can be customized for a particular motor. The driver speed input can be either analogue or from a PWM. It has undervoltage detection, thermal shutdown and a brake feature.

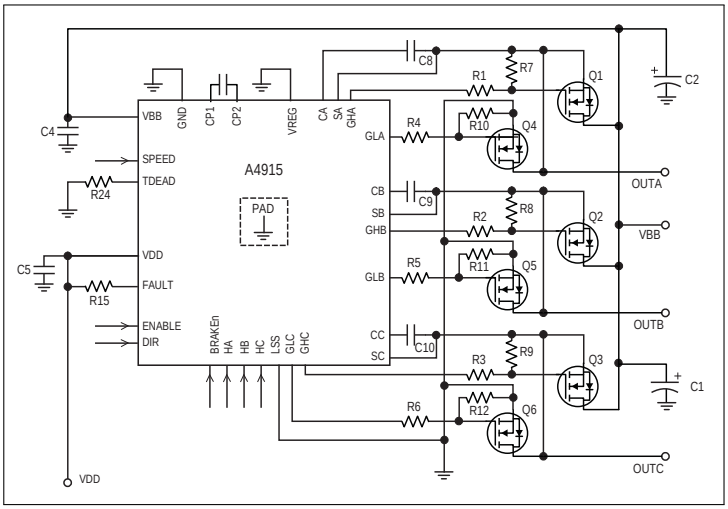

Figure 2.14: Circuit diagram for A4915 driver from datasheet [27].

2.4.2.4 A4941

The A4941 from Allegro is an example of a sensor-less driver that was also tested. This IC is very small at 5 mm × 6.4 mm and requires the smallest PCB area of all the drivers tested, but does not use the Hall sensor outputs from the motors for commutation, but rather the back electromotive force (EMF). It requires few additional components and has overcurrent protection and PWM speed control. The driver had difficulty commutating the motor at low speeds and did not have brake or reverse features. This does not influence the performance of the proposed DGCMG design, due to the high

nominal rotation rate of the flywheels. It is however favourable to acquire a driver that is suitable for multiple applications such as conventional reaction wheels.

2.4.2.5 LV8827LFQA

The driver that was used in the final design is the LV8827LFQA from ON Semiconductor. This driver utilizes the Hall sensors for commutation and has a voltage range of 8 V to 35 V. As with the L6235D, the driver was found to operate at just 7 V, but is not recommended as this falls outside the specifications and may differ for other ICs of different batches. The package size is 4 mm × 4 mm and few supporting components are necessary. The driver uses a PWM signal for speed control and has a brake and reverse feature. The IC also has a current-limiter, undervoltage protection and thermal shutdown. A comparison of all the different features of the drivers is shown in Table 2.2.

2.4.2.6 Driver Power Usage

The LV8827LFQA driver performed well during power usage comparisons, as seen in Table 2.1. The power measurements for all the drivers tested include the Hall sensors, digital logic of the drivers and XOR gates for the rate signal. PCB designs for each driver can be found in Appendix E.

Table 2.1: BLDC Motor Driver Power Usage.

Driver	**Average Power [mW]**			
	0 RPM	**200 RPM**	**4000 RPM**	**10000 RPM**
BA6859AFP-Y	110	160	181	263
L6235D	106	119	148	252
LV8827LFQA	112	112	145	211
A4915	105	123	178	334
A4941	43	NA	71	140

The XOR gates are used to construct a flywheel speed signal from the signals on the three Hall sensor output lines of the BLDC motors. Each Hall sensor gives two pulses for every rotation of the wheel. The output from the XOR gate will therefore give six pulses for every rotation of the flywheel. This signal is shown in Figure 2.15 for one rotation. The microcontroller counts these pulses during one sample period to determine the flywheel speed.

This does not provide a very high resolution speed feedback and will limit the settling time of the BLDC motor speed control, but is sufficient for the current CMG application. To perform yaw manoeuvres the wheel speeds will deviate from their high

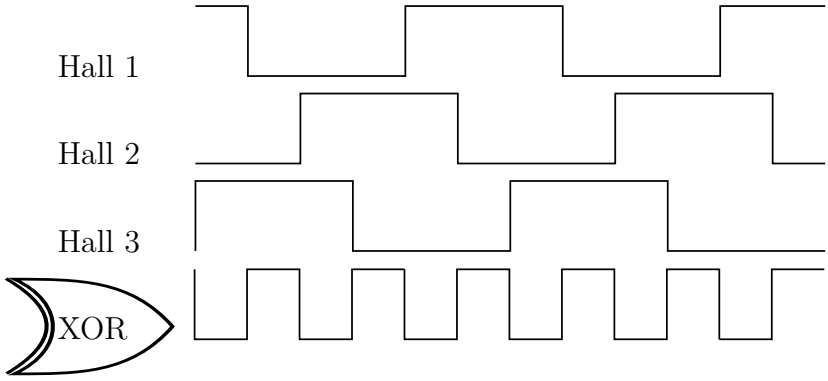

Figure 2.15: BLDC motor rate feedback signal.

nominal speed, but still remain high enough for the Hall sensor signal to be adequate. For reaction wheels that does not have a speed bias, it is necessary to have an external encoder.

Table 2.2: BLDC Motor Driver Features.

Features	**BA6859AFP-Y**	**L6235D**	**LV8827LFQA**	**A4915**	**A4941**
Small PCB Size	×	×	✓	×	✓
Low Voltage	✓	×	×	✓	✓
Direction Control	×	✓	✓	✓	×
Brake	✓	✓	✓	✓	×
Digital PWM Control	×	×	✓	✓	✓
Voltage Protection	×	✓	✓	✓	✓
Current Limiting	✓	✓	✓	×	✓
Thermal Protection	✓	✓	✓	✓	✓
Sensored Commutation	✓	✓	✓	✓	×

2.4.3 Stepper Motor Drivers

The stepper motors used is bipolar with 20 steps per revolution. The stepper motors have their own gearboxes with a ratio of 64:1. This will allow for an inner gimbal angle resolution of 0.067° and an outer gimbal resolution of 0.066°.

The first driver considered, is the A3901 dual H-bridge from Allegro. This driver is very small at 3 mm × 3 mm and has thermal shutdown and shoot through protection. The driver is capable of running in either full- or half-step mode as previously discussed. The LV8411GR from ON Semiconductor was also tested. This driver is the same size as the A3901, but contains four H-bridges rather than two. This allows for two stepper motors to be driven by a single IC. This driver also has thermal protection, undervoltage protection and an extra transistor for driving photosensors.

The magnetic torquer rods used in the CubeSat for momentum dumping requires an H-bridge to be driven in forward or reverse mode. The stepper drivers can therefore be

used for multiple applications in the satellite. The A3901 was used in the final design due to availability and the space flight heritage. This IC has been used in previous satellite missions to drive magnetic torquer rods.

The steps will be counted in order to determine the current angle of the gimbals. During tests, it was found that the stepper motors occasionally missed steps at some rate commands and that the current angle value is lost after a reset occurred. For further development it is recommended to have a rotation sensor that will provide absolute angle feedback even after a reset of the system occurs.

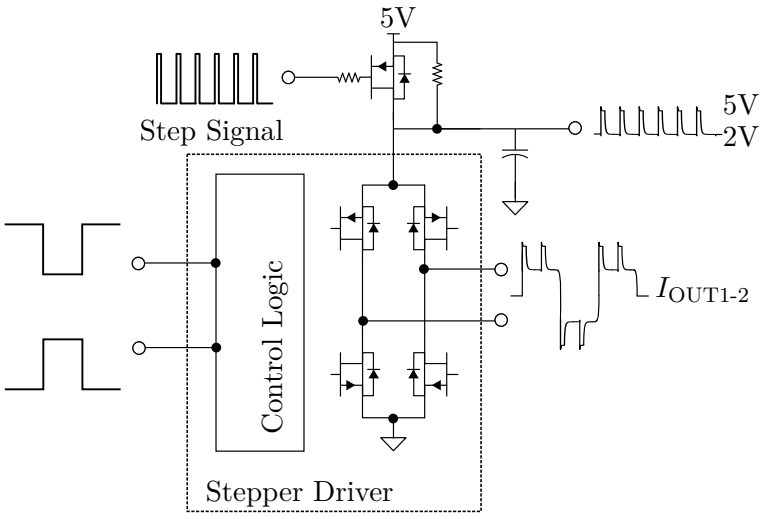

Figure 2.16: Stepper H-bridge with signals for single coil.

To improve the stepper reliability, a method must be devised of powering the stepper coils to produce an initial large torque in order to accelerate the stepper rotor and then reduce the torque, as the rotor acquires the necessary velocity to propel it to the next step position. This is done by applying a high voltage at the power supply pin of the driver during the initial step and then a lower voltage to ensure the rotor reaches a desired step position. The circuit for this is simple and is shown in Figure 2.16, with the input and output signals for a single coil of the stepper motor. Notice the BSS84P P-channel MOSFET at the power supply of the stepper driver.

2.4.4 Microcontroller

The microcontroller selected for this DGCMG application will be used during testing, but any commercially available ADCS OBC should be able to perform the functions required. For the tests, the microcontroller must be able to send and receive commands from the PC. The microcontroller will contain the control system of the BLDC motors and hold the gimbal steppers count in memory. It will also receive rate measurements

from the ADIS16375 and relay them to the PC. A survey of microcontrollers suitable for an ADCS OBC was conducted by Botma [28] and from his research it was decided that, for the required functions, an 8-bit microcontroller would be sufficient and will require less power. It would be favourable to use a microcontroller that is similar to those already in use on satellites. ATMEL has radiation hardened microcontrollers available and it would be favourable to develop using their architecture. The ATMEGA90CAN128 from ATMEL was used as microcontroller due to its low power usage and possible expansion to also utilize the CAN bus and the I2C bus commonly used in CubeSats. The pins used on the microcontroller are:

- 2 Interrupt pins for XOR gate signals.
- 2 Digital pins for BLDC drivers.
- 2 PWM output pins for BLDC drivers.
- 14 Digital output pins for stepper motor drivers.
- RX and TX pins.
- SPI communication pins.
- 1 Interrupt pin for ADIS16375 data ready flag.

The layout of the microcontroller and drivers are shown in Figure 2.17 and more detailed PCB layouts are shown in Appendix E.

The two interrupts from the XOR gates are used to count the pulses during a sampling period. These pulses are used to determine the rate of the BLDC motors. The two digital pins connected to the BLDC motor drivers are used to set the rotation direction of the motors. These pins can be hard coded as the motors will always spin in opposite directions for this DGCMG configuration. The two PWM pins control the current supplied by the drivers to the BLDC motors. Varying the duty cycle of the PWM allows for speed control. A 0% duty cycle will cause the driver to enter short brake mode and will allow the control system to reduce the rate of the flywheel quickly. Each stepper motor H-bridge requires four inputs to set the pulse sequence sent to the coils as discussed previously. The additional two digital pins used by the stepper motors are used to chop the power supply of the stepper drivers, in order to reduce the power consumption. This method is discussed in the previous section and shown in Figure 2.16. The TX and RX pins are used by the UART of the microcontroller to communicate with the PC. This communication is done via a wireless link. The SPI pins are used to communicate with the ADIS16375. These SPI pins include the SCK,

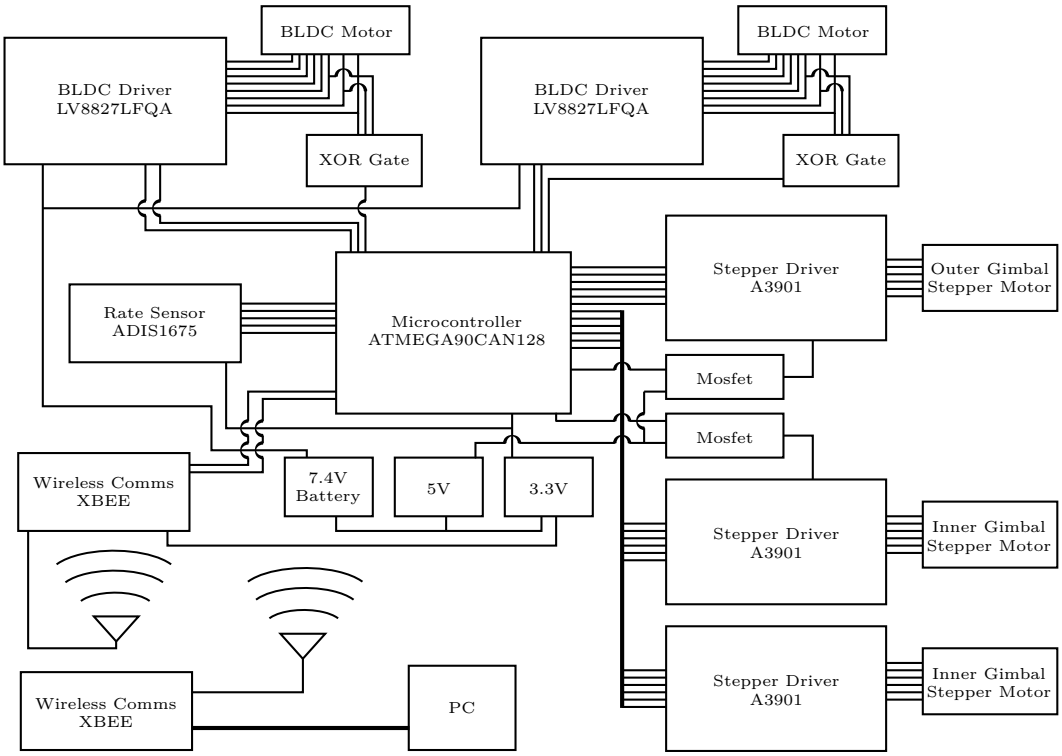

Figure 2.17: Layout of electronic components.

MISO, MOSI and $\overline{\text{SS}}$. The SCK pin carries the serial clock from the microcontroller to the ADIS16375 where each clock pulse coincides with data transferred via the MOSI pin towards the ADIS16375 and via the MISO pin towards the microcontroller. The $\overline{\text{SS}}$ pin is used to select the ADIS16375 as the slave component being communicated with. More information about the ADIS16375 SPI communication is given in Appendix B. There is an additional interrupt pin connected to the ADIS16375 indicating when a measurement is ready and a SPI read can commence.

The microcontroller is running at a clock frequency of 8 MHz provided by an external crystal oscillator. This clock frequency is divided by integer values within the microcontroller to provide the stepping frequency used for the stepper motor rates. This clock divider is set by a variable received from the PC to change the stepper rates.

2.4.5 Wireless Communication

For practical tests, the final model will be placed on a low friction platform to perform slew manoeuvres. It is required that no cables influence the torque on the system. Therefore communications must be done wirelessly and power must be provided by a battery. XBEE wireless shields were used for communication due to their ease of setup,

availability and small size as seen in Figure 2.18. These shields use the 2.4 GHz band and require 165 mW during transfers.

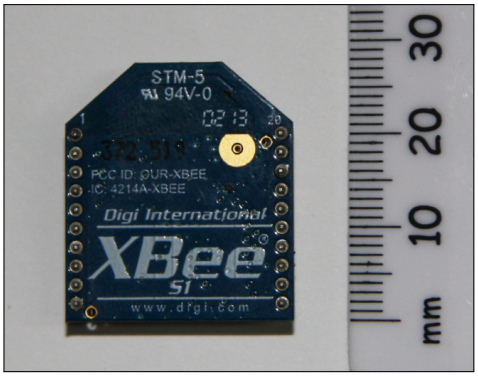

Figure 2.18: XBEE wireless shield.

2.4.5.1 Protocol

The packets sent by the PC to the microcontroller consist of the following bytes:

- 16 bit Inner gimbal reference angle as step count.
- 8 bit Inner gimbal reference rate as a clock divider.
- 16 bit Outer gimbal reference angle as step count.
- 8 bit Outer gimbal reference rate as a clock divider.
- 2×16 bit Reference speed for BLDC motors in RPM.
- 2×16 bit Control system gains for BLDC motors.
- End of packet indication sequence: 0xFF, 0x00, 0xFF, 0x00.

And packets received by the PC from the microcontroller consists of:

- 16 bit Current inner gimbal angle as step count.
- 8 bit Current inner gimbal rate as a clock divider.
- 16 bit Current speed for BLDC motor in RPM (A).
- 16 bit Current outer gimbal angle as step count.
- 8 bit Current outer gimbal rate as a clock divider.
- 16 bit Current speed for BLDC motor in RPM (B).

- 16 bit X-axis rate from ADIS16375.
- 16 bit Y-axis rate from ADIS16375.
- 16 bit Z-axis rate from ADIS16375.
- End of packet indication sequence: 0x00, 0xFF.

Therefore, a send and receive sequence will consist of 288 bits. The communication sequence must complete in as short a period as possible to allow the control systems sufficient time to execute within a sample period of 100 ms. This 100 ms sample period was chosen to achieve a suitable control bandwidth for the BLDC motors and slew controller. With a baud rate of 19 200 bps the transfer will complete in 15 ms and leaves ample time for all other functions to complete. The end packet sequences is used to identify that a packet has been received. When the sequence is received, the length of the packet will indicate if any bytes have been lost. The buffer is cleared after each packet is received. This is not a very robust protocol, but is sufficient for the short distance communication done during the tests. Improvements can be made by adding a packet start sequence and a parity check before the end of packet sequence. The packet can also be split into separate control packets containing different information. This will prevent redundant data transfers such as the wheel controller gains.

2.4.6 Power Supply

As mentioned before, the testing setup will require the use of a battery. The battery used is a Lithium-Polymer 2 cell battery with a 3200 mA h capacity and an average charged voltage of 7.4 V. The different components have theoretical maximum power ratings shown in Table 2.3 as found from the datasheets. These values have not been confirmed individually with measurements and are derived from the supply currents as stated in the datasheets and the actual voltage used to power the IC.

From this table the voltage supplies required are the raw battery voltage (7.4 V), 5 V and 3.3 V. Linear regulators are used to supply these voltages, but switched mode regulators can be used in future to improve efficiency. The regulators used are the well-known LM317 (NCV317BD2TG) for the 3.3 V line and a 7805 (MC7805CD2TG) for the 5 V line. The maximum current supplied by the raw battery voltage line can be limited to 400 mA as the BLDC motors are the only components utilizing this source. The 5 V regulator must be able to supply 240 mA for use by all the stepper motors. The 3.3 V supply are used for all the digital logic and should be stabilized by larger capacitors to reduce noise. During tests, it was found that the 3.3 V supply was unable

Table 2.3: Component Power Usage.

Component	**Voltage Source [V]**	**Average Power [mW]**	**Maximum Power [mW]**
ATMEGA90CAN128	3.3	33	100
Stepper Motor	5	178	400
BLDC Motor	6	128.8	1295
Stepper Driver	5	4.4	8.6
BLDC Driver	7.4	31.3	37.6
Wireless XBEE	3.3	148.5	165
ADIS16375	3.3	570.9	1500

to switch on the ADIS16375. The datasheet states that for 400 µs during start-up, the ADIS16375 can draw up to 1.5 A. The surface mount version of the LM317 can only supply a maximum of 1 A. By monitoring the voltage on the regulated 3.3 V supply, it was found that the ADIS16375 retries the start-up every 324 ms, as indicated by voltage drop-outs. By placing a capacitor in parallel to the ADIS16375, the initial start-up will fail, but the capacitor will charge during the 324 ms period before the ADIS16375 tries the start-up again. By using a large 1 mF capacitor, it will be fully charged by the 1 A source within 16.5 ms. With this fully charged capacitor a current of 1.5 A could be supplied for 11 ms which is enough to start the ADIS16375.

With the power information in Table 2.3, the specification in Chapter 1 can be adjusted to 4 W peak and 0.9 W average. This excludes the rate sensor and XBEE power usage and will decrease the expected power efficiency defined in Chapter 1.

2.5 Motor Control

The BLDC motor speeds must be controlled to specific values in order for the slew controllers to operate correctly. In this section a simple speed controller is designed that will be implemented in the microcontroller. To find a model for the BLDC motors, the duty cycle of the PWM control input to the driver is adjusted until the output speed is roughly at the nominal wheel speed during DGCMG operation. The duty cycle is then adjusted until the speed reaches roughly the maximum used during the slew manoeuvres. A test is then performed where the PWM duty cycle is stepped from the nominal speed to the maximum speed. The transient response for this step input can be seen in Figure 2.19. During tests it was found that the model is different at low speeds. The model derived around this operating point provide a good representation of the system for typical operation speeds.

The input to the motor driver is a PWM signal that governs the applied voltage

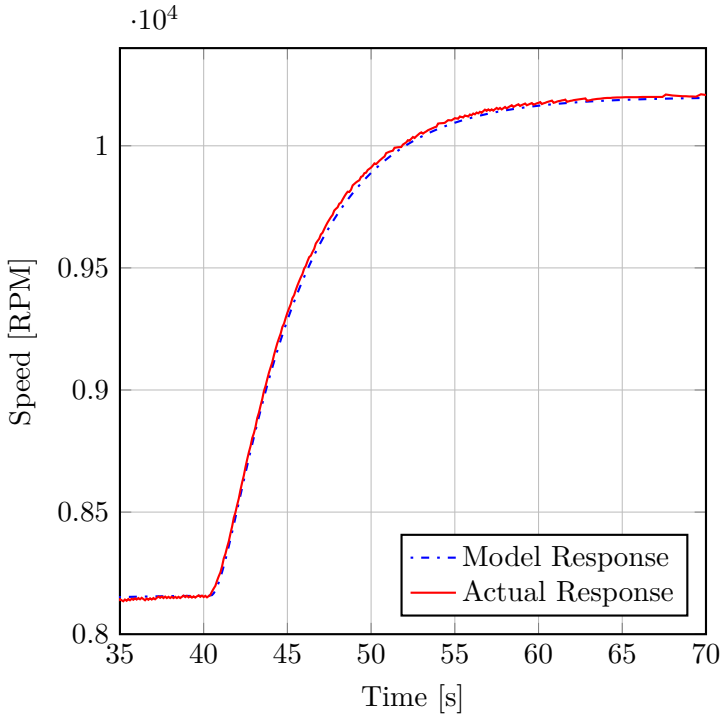

Figure 2.19: Open loop step response of reaction wheel.

and the motor speed is the output being controlled. The model for the motor speed will thus be second order. A second order model was fitted to the measured transient response by adjusting the natural frequency and damping parameters as seen in (2.2). The figure shows that the model matches the actual response. This model can then be discretized by taking its Z-transform for a sampling time of 0.1 s as seen in (2.4). A faster sample time can be used if a more accurate encoder is used for the BLDC motors.

$$G(s) = \frac{K\omega_n^2}{s^2 + 2\zeta\omega_n s + \omega_n^2} \tag{2.2}$$

$$= \frac{45.48}{s^2 + 1.455s + 0.2675} \tag{2.3}$$

$$G(z) = \frac{0.2167z + 0.2065}{z^2 - 1.862z + 0.8646} \tag{2.4}$$

The open loop poles and zeros for this model are given by,

$$\text{Poles} = \begin{bmatrix} 0.9786 & 0.8835 \end{bmatrix} \tag{2.5}$$

$$\text{Zeros} = -0.9527 \quad , \tag{2.6}$$

and can be seen in the root locus plot in Figure 2.20.

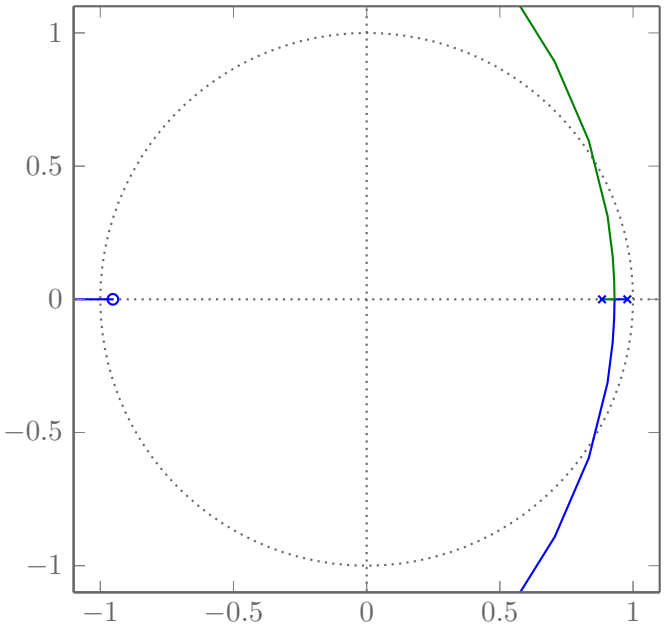

Figure 2.20: Root locus plot of open loop model in discrete domain.

To perform yaw rotations, the wheel speeds will change and for this application overshoot is undesirable. In order to achieve the best settling time with minimal overshoot, the closed loop specifications are chosen as:

$$\zeta = 0.9 \tag{2.7}$$

$$2\%\mathrm{t}_s < 10\,\mathrm{s} \tag{2.8}$$

With this settling time, the bandwidth of the system improved from $0.2\,\mathrm{rad\,s^{-1}}$ to $0.48\,\mathrm{rad\,s^{-1}}$. This bandwidth can be improved further with more accurate speed encoders and motors with higher torque and braking capabilities. The wheels must also follow a reference input with no steady state error in order for slews to be performed accurately. For this, integral control is required and a pole at $z = 1$ is added. By cancelling the plant open loop pole at 0.9786, the gain can be adjusted to achieve the required transient response.

$$C(z) = \frac{K(z - 0.9786)}{(z - 1)} \tag{2.9}$$

With gain K=0.011 the closed loop poles are at $0.941 \pm 0.0335i$. These poles provide a settling time of 6.6 s and a damping of 0.862 close to the specifications. In Figure 2.21 it can be seen that the BLDC RPM very closely follow the reference and only has slightly more overshoot than the simulated response. The zero position and gain can

be easily adjusted by variables in the communication packet and allows different wheel models to be used.

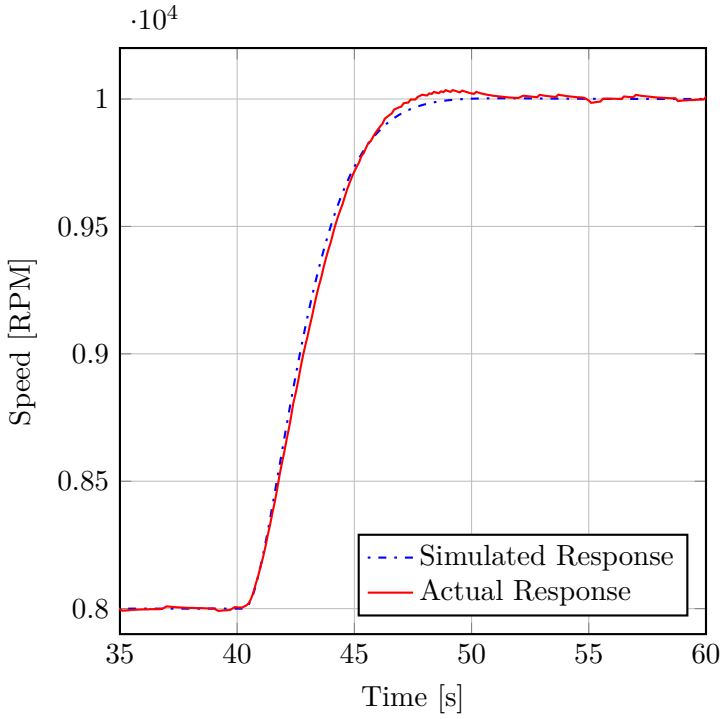

Figure 2.21: Closed loop step response of reaction wheel.

2.6 Summary

In summary, this chapter has outlined the design of the proposed DGCMG configuration. The motors used in the design are three small stepper motors for the gimbal angle actuators and two BLDC motors for the flywheel speeds. The mechanical design section discussed the materials used for the structure and the gears designed to rotate the gimbals. The electronic design included an evaluation of the drivers selected for the BLDC and stepper motors and the microcontroller functions. Communication methods, sensors used and the power management were then discussed and selection of components was made. Finally the control system located on the microcontroller responsible for the BLDC speeds was designed. This completed DGCMG configuration can now be evaluated with tests in the upcoming chapters. Detailed schematics of all mechanical and electronic designs can be found in Appendix D.1 and E.

Chapter 3

Attitude Control

Attitude refers to the orientation of one reference frame with respect to another. This orientation can be represented in a number of ways, most notably of which is a Direction Cosine Matrix (DCM), Euler angles, Axis-Angle and Quaternions. The DCM representation is a 3×3 matrix that can rotate any vector from reference frame A to reference frame B. Every element of this matrix, C_{ij}, is the cosine of the angle between the corresponding vector elements, b_i and a_j. Equation 3.1 shows a simple rotation of a vector in reference frame A to reference frame B.

$$\begin{aligned} \begin{bmatrix} b_1 \\ b_2 \\ b_3 \end{bmatrix} &= \begin{bmatrix} C_{11} & C_{12} & C_{13} \\ C_{21} & C_{22} & C_{23} \\ C_{31} & C_{32} & C_{33} \end{bmatrix} \begin{bmatrix} a_1 \\ a_2 \\ a_3 \end{bmatrix} \\ &= \mathbf{C}_{\mathrm{A}}^{\mathrm{B}} \begin{bmatrix} a_1 \\ a_2 \\ a_3 \end{bmatrix} \end{aligned} \tag{3.1}$$

A helpful property of this representation is that the DCM matrix is orthonormal and the rotation from reference frame B to A is simply the transform or inverse of the matrix in (3.1). Therefore $\mathbf{C}_{\mathrm{B}}^{\mathrm{A}} = \left[\mathbf{C}_{\mathrm{A}}^{\mathrm{B}}\right]^{-1} = \left[\mathbf{C}_{\mathrm{A}}^{\mathrm{B}}\right]^{T}$. A disadvantage of this representation is that it contains redundant information about the rotation that will cause an increase in processing and storage requirements.

Euler angles is a set of rotations performed on a vector about each axis of the current reference frame in a specified order. The order is given as Euler 1-2-3, Euler 3-2-1, etc. and each provides a unique rotation sequence to the same final attitude. An Euler 1-2-3 rotation will refer to a roll around the X-axis followed by a pitch around the Y-axis and finally a yaw around the Z-axis. This representation is often used in satellites and

aircraft due to the easy visualization of rotations by humans. This representation only requires three values, but the use of trigonometric functions complicate the calculations. The microcontroller uses Taylor series expansion to approximate the trigonometric values and singularity situations may occur at some angles when solving the kinematic equations.

The Axis-Angle representation are derived from Euler's Eigenaxis Rotation theorem. This theorem states that any rotation can be represented by a unit vector, representing an axis that is stationary in the inertial reference frame and also fixed to the body of the rotating object, and an angle that gives the magnitude of rotation around the axis. The orientation of the axis will hence remain unchanged relative to the inertial and the body reference frame. The axis is often referred to as the Euler axis or the eigenaxis.

The Euler axis, (e_1, e_2, e_3), and angle, θ, parameters can be represented in a special form referred to as a Quaternion, (q_1, q_2, q_3, q_4), as defined in (3.2).

$$\begin{aligned} q_1 &= e_1 \sin\left(\frac{\theta}{2}\right) \\ q_2 &= e_2 \sin\left(\frac{\theta}{2}\right) \\ q_3 &= e_3 \sin\left(\frac{\theta}{2}\right) \\ q_4 &= \cos\left(\frac{\theta}{2}\right) \end{aligned} \tag{3.2}$$

where,

$$q_1^2 + q_2^2 + q_3^2 + q_4^2 = 1$$

This Quaternion representation has the special property of no singularities or trigonometric functions and is consequently used in control mathematics. More information about these attitude representations and the conversion between them can be found in Appendix A.

3.1 Reference Frame

Satellite attitude refers to the orientation of the satellite body frame with respect to a predefined reference frame. The frame often used by earth orbiting bodies is the orbit reference frame. This reference frame is ideal for earth observation and orientations

relative to the flight path. In this orbit reference frame the X- and Z-axis are in the orbital plane with the Z-axis nadir pointing and the X-axis pointing at the velocity vector (during circular orbits) as shown in Figure 3.1. Note that the Y-axis completes the right hand orthogonal set. The orientation of the satellite is often expressed as roll around the X-axis, pitch around the Y-axis and yaw around the Z-axis for simple human understanding.

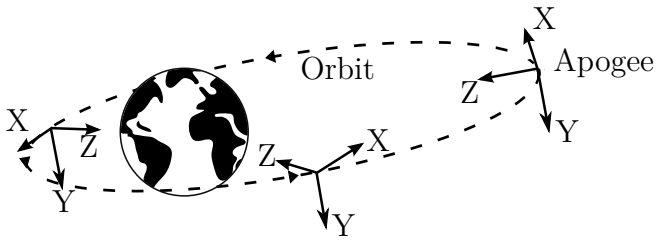

Figure 3.1: Orbital reference frame.

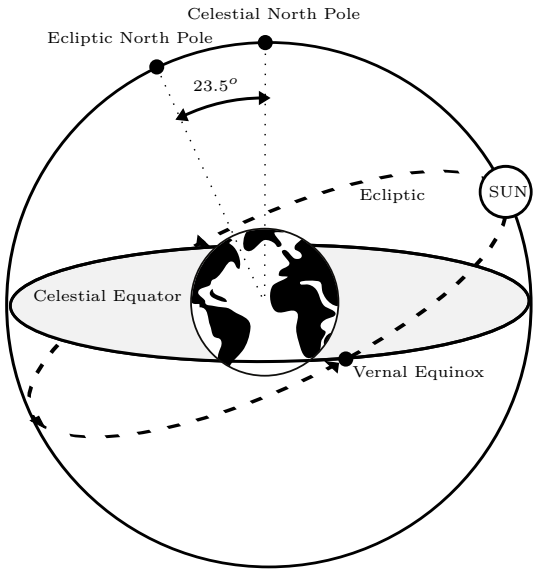

Figure 3.2: Inertial reference frame.

It is also necessary to have a reference frame that is inertially fixed. Such a reference frame is helpful in orbit analysis, star cameras and any inertial motion calculations. The inertial reference frame often used by earth orbiting bodies is the geocentric reference frame with its origin at the centre of the earth where the X-axis is aligned with the vernal equinox and the Z-axis is towards the celestial North Pole as shown in Figure 3.2. Again note that the Y-axis completes the right hand orthogonal set. The vernal equinox is the point where the sun passes through the earth's equatorial plane, called the celestial equator, towards the northern celestial hemisphere. This frame is not truly inertial due to the motion of the earth around the sun and the slow orbital precession

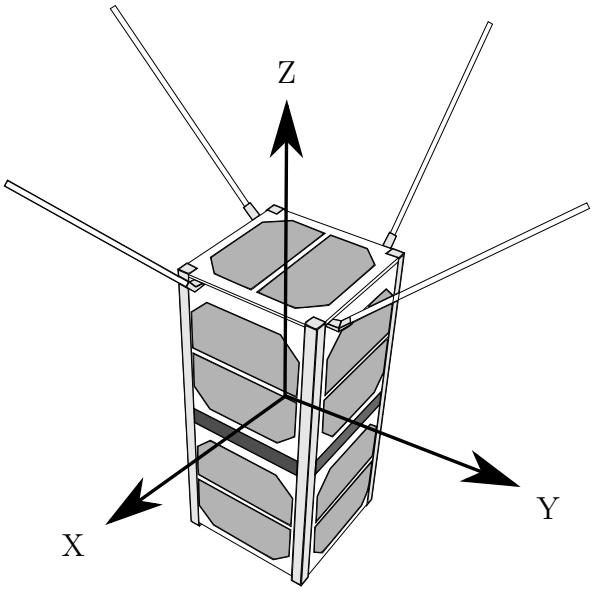

Figure 3.3: Satellite body reference frame.

of the vernal equinox. For an exact inertial reference frame a time stamp is needed such as the mean vernal equinox vector on 1 January 2000, commonly known as the J2000 frame.

Another inertial reference frame is the heliocentric frame, where the origin is at the centre of the sun and the Z-axis is now in the ecliptic pole direction and the X-axis is again in the vernal equinox direction. This reference frame is ideal for any bodies that do not orbit earth but rather the sun, but this is not relevant to this study.

Lastly, a reference frame is needed for the satellite itself, in order to map the orientation of its internal components. This satellite reference frame has its centre at the satellite centre of mass and its axes aligned with the satellite body as seen in Figure 3.3. This allows the different attitude sensors and actuators to be given mounting direction cosine matrices to define their orientation in the satellite. The satellite body reference frame is often chosen to align with the orbit reference frame for nominal satellite orientation.

3.2 System Modelling

The DGCMG configuration designed in the previous chapter must be evaluated with tests and simulations. This will enable comparisons with the design specifications outlined in Chapter 1 and current technology that is commercially available. In order to determine the torque capabilities of the proposed DGCMG, a model must be developed that closely simulate the physical setup.

3.2.1 Rotational Kinematics

The proposed DGCMG configuration can be simplified as two DGCMGs as seen in Figure 3.4 and the rotational kinematics of this system can then be analysed. In order to use the DGCMG as a torque actuator for the satellite, the torque output must be found in terms of the current gimbal angles, gimbal rates and flywheel rates. Torque is equal to the change in angular momentum of a system. Therefore, to model the torque capabilities, the angular momentum of the wheels must first be converted to each gimbal reference frame and finally to the satellite body frame. This vector is reliant on the rotation angles of the gimbal frames. The rotation of the gimbal frames will have a momentum contribution to the system, but this can be ignored during calculations due to the balanced layout.

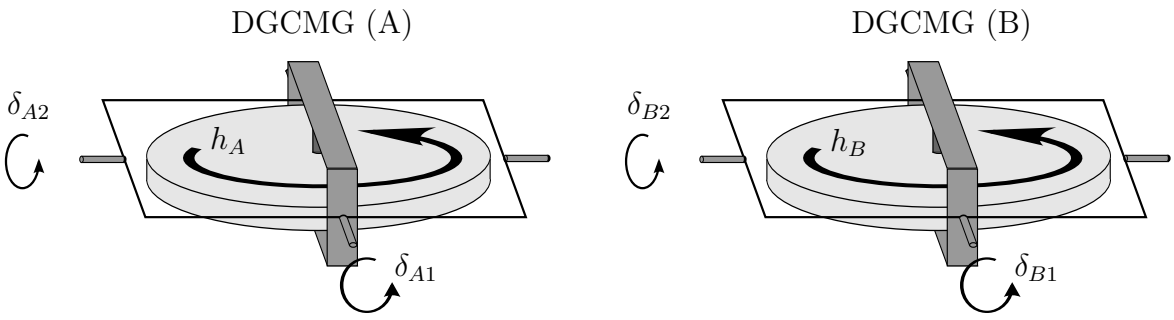

Figure 3.4: Scissored DGCMG pair.

Focussing on the DGCMG-A first, the angular momentum, h_A, is directed in the positive Z-axis of the wheel reference frame. The transformation to the first and then second gimbal reference frames is given by (3.5).

$$\mathbf{h'_A} = \begin{bmatrix} 1 & 0 & 0 \\ 0 & \cos(\delta_{A1}) & \sin(\delta_{A1}) \\ 0 & -\sin(\delta_{A1}) & \cos(\delta_{A1}) \end{bmatrix} \cdot \mathbf{h_A} \tag{3.3}$$

$$\mathbf{h''_A} = \begin{bmatrix} \cos(\delta_{A2}) & 0 & -\sin(\delta_{A2}) \\ 0 & 1 & 0 \\ \sin(\delta_{A2}) & 0 & \cos(\delta_{A2}) \end{bmatrix} \cdot \mathbf{h'_A} \tag{3.4}$$

$$= \begin{bmatrix} -\cos(\delta_{A1})\sin(\delta_{A2})h_A \\ \sin(\delta_{A1})h_A \\ \cos(\delta_{A1})\cos(\delta_{A2})h_A \end{bmatrix} \tag{3.5}$$

The inner gimbal angles are given by δ_1 and the outer gimbal angle by δ_2. The

A and B subscripts identify which DGCMG is referenced. The wheel momentum for DGCMG-B is also referenced with the satellite body in the same way and the total angular momentum result is then calculated as shown in (3.6).

$$\mathbf{h}_{\text{total}} = \begin{bmatrix} -h_A \cos(\delta_{A1}) \sin(\delta_{A2}) - h_B \cos(\delta_{B1}) \sin(\delta_{B2}) \\ h_A \sin(\delta_{A1}) + h_B \sin(\delta_{B1}) \\ h_A \cos(\delta_{A1}) \cos(\delta_{A2}) + h_B \cos(\delta_{B1}) \cos(\delta_{B2}) \end{bmatrix} \tag{3.6}$$

As previously mentioned, this configuration has the constraint that the gimbals are scissoring, meaning that the gimbal angles are of equal magnitude but opposite directions. It is also constrained that the angular momentum of the two wheels have a component, h_0, that is in opposite directions and a variable, Δh, the difference in magnitude. These constraints are shown in (3.7) to (3.10).

$$h_A = h_0 + \frac{1}{2}\Delta h \tag{3.7}$$

$$h_B = -h_0 + \frac{1}{2}\Delta h \tag{3.8}$$

$$\delta_{A2} = -\delta_{B2} = \delta_2 \tag{3.9}$$

$$\delta_{A1} = -\delta_{B1} = \delta_1 \tag{3.10}$$

Equation 3.6 can then be simplified by these constraints to (3.11).

$$\mathbf{h}_{\text{total}} = \begin{bmatrix} -2 \cos(\delta_1) \sin(\delta_2) h_0 \\ 2 \sin(\delta_1) h_0 \\ \cos(\delta_1) \cos(\delta_2) \Delta h \end{bmatrix} \tag{3.11}$$

With the angular momentum vector of the DGCMG setup defined, the variables that can be manipulated by actuators are chosen as the states of the control system. These states are $\mathbf{x} = \begin{bmatrix} \delta_1 & \delta_2 & \Delta h \end{bmatrix}^T$.

3.2.2 Rigid-Body Dynamics

The satellite can be assumed to be a rigid body with an applied torque causing an angular acceleration around its centre of mass proportional to the moment of inertia of the satellite. This is known as the Euler rotational equation of motion and is given by (3.12).

$$\mathbf{I}\dot{\boldsymbol{\omega}}_B^I = \mathbf{N}_{\text{slew}} = \mathbf{N}_{\text{gyro}} - \mathbf{N}_{\text{DGCMG}} + \mathbf{N}_{\text{disturb}} \tag{3.12}$$

$\mathbf{N}_{\text{gyro}}$ represents the gyroscopic coupling torque of the spacecraft and is given by (3.13).

$$\mathbf{N}_{\text{gyro}} = -\boldsymbol{\omega}_B^I \times (\mathbf{I}\boldsymbol{\omega}_B^I + \mathbf{h}_{\text{total}}) \tag{3.13}$$

The satellite moment of inertia is given by $\mathbf{I}$ and the inertially referenced satellite angular rate is given by $\boldsymbol{\omega}_B^I$. This body rate vector represents the inertial angular rates about the principal axes of the satellite and can be measured with gyroscopic sensors mounted on the satellite body. The rotation of the satellite is generally very slow and hence the gyroscopic torque will be small in comparison to the other torques. Therefore the gyroscopic torque may be ignored, but with the computational strength of modern microcontrollers, it is not necessary. $\mathbf{N}_{\text{DGCMG}}$ is the internal actuator generated torque that is given by (3.14), which is the differentiation of the angular momentum of the system calculated in (3.11). The $\mathbf{N}_{\text{disturb}}$ torque is a combination of all the disturbance torques such as aerodynamic drag, magnetic coupling torque, gravity gradient torque and solar radiation pressure as discussed in Chapter 1.

With the actuator torque, $\mathbf{N}_{\text{DGCMG}}$, available from the steering laws, the change in actuator states, $\dot{\mathbf{x}}$, should be determined that will provide this torque. This change in actuator states can be found using the propagation matrix, $\mathbf{B}(\mathbf{x})^{-1}$, as seen in (3.15. The propagation matrix is simply the inverse of the Jacobian matrix, $\mathbf{B}$, as seen in (3.14). This Jacobian matrix is the partial differentiation of the total angular momentum from (3.11). Whenever the inverted Jacobian matrix is undefined, a singularity event occurs. For this case it is when any of the gimbal angles reach $\pm 90°$, but this is outside the capabilities of the current mechanical design.

$$\begin{aligned}\mathbf{N}_{\text{DGCMG}} = \dot{\mathbf{h}}_{\text{total}} = \mathbf{B}(\mathbf{x}) \cdot \dot{\mathbf{x}} &= \frac{\partial \mathbf{h}_{\text{total}}}{\partial \mathbf{x}} \cdot \dot{\mathbf{x}} \\ &= \begin{bmatrix} 2\sin(\delta_1)\sin(\delta_2)h_0 & -2\cos(\delta_1)\cos(\delta_2)h_0 & 0 \\ 2\cos(\delta_1)h_0 & 0 & 0 \\ -\sin(\delta_1)\cos(\delta_2)\Delta h & -\cos(\delta_1)\sin(\delta_2)\Delta h & \cos(\delta_1)\cos(\delta_2) \end{bmatrix} \cdot \dot{\mathbf{x}}\end{aligned} \tag{3.14}$$

$$\dot{\mathbf{x}} = \mathbf{B}(\mathbf{x})^{-1} \cdot \dot{\mathbf{h}}_{\text{total}} = \begin{bmatrix} 0 & \frac{1}{2\cos(\delta_1)h_0} & 0 \\ \frac{-1}{2\cos(\delta_1)\cos(\delta_2)h_0} & \frac{\sin(\delta_1)\sin(\delta_2)}{2\cos^2(\delta_1)\cos(\delta_2)h_0} & 0 \\ \frac{-\sin(\delta_2)\Delta h}{2\cos(\delta_1)\cos^2(\delta_2)} & \frac{\sin(\delta_1)\Delta h}{2\cos^2(\delta_1)\cos^2(\delta_2)h_0} & \frac{1}{\cos(\delta_1)\cos(\delta_2)} \end{bmatrix} \cdot \dot{\mathbf{h}}_{\text{total}} \tag{3.15}$$

The control laws explained in Sections 3.3 and 3.4 provide the torque reference, $\mathbf{N}_{\text{slew}}$ that is used in (3.14) and (3.15) to find the change in state vector, $\dot{\mathbf{x}}$, and with the current states known, the new state vector can be determined with integration. The new states can now be sent to the actuators and also used to update the inverted Jacobian matrix.

3.3 Bang-Off-Bang Controller

In order to provide optimal large angle agility for the satellite, a control law is necessary that will give near minimum time slew manoeuvres around a constant eigenaxis. A controller that will meet these requirements is described by Steyn [23, 29] for dual-wheel configurations and will be referred to henceforth as a Bang-Off-Bang controller.

The controller will find the angle error as a quaternion, $\mathbf{q}_e$, as shown by (3.16) and also calculate the halfway point condition for the manoeuvre as shown by (3.18). See Appendix A for detail about quaternion rotation representation.

$$\mathbf{q}_e = \mathbf{q}^{-1}\mathbf{q}_f = \begin{bmatrix} q_{f4} & q_{f3} & -q_{f2} & -q_{f1} \\ -q_{f3} & q_{f4} & q_{f1} & -q_{f2} \\ q_{f2} & -q_{f1} & q_{f4} & -q_{f3} \\ q_{f1} & q_{f2} & q_{f3} & q_{f4} \end{bmatrix} \begin{bmatrix} q_1 \\ q_2 \\ q_3 \\ q_4 \end{bmatrix} \tag{3.16}$$

The commanded final rotation quaternion is given by $\mathbf{q}_f$.

$$\max_{i=1,2,3} |q_{ie}(t)| - q_{\text{half}} = \begin{cases} > 0 & \forall t < t_h \\ < 0 & \forall t > t_h \end{cases} \tag{3.17}$$

$$q_{\text{half}} = \max_i \left| \frac{q_{ie}(t_0) \sin(\frac{\theta}{4})}{\sin(\frac{\theta}{2})} \right| \tag{3.18}$$

The current time is given by t, and t_h is the time when the halfway point is reached. The start time of the manoeuvre is given by t_0, and the angle, θ, is calculated at the start of the manoeuvre as the shortest angle between the commanded pointing vector and the current pointing vector that is given in quaternion rotation format, $\mathbf{q}$.

With only body rate measurements, $\boldsymbol{\omega}_B^I = \begin{bmatrix} \omega_1 & \omega_2 & \omega_3 \end{bmatrix}^T$, available during tests, the rates must be integrated in order to obtain $\mathbf{q}$. This can be done by solving (3.19) to (3.22) and integrating the $\dot{\mathbf{q}}$ result. During space flight, this will not be necessary as sun and nadir data would be available and will provide the current pointing vector.

$$\dot{q}_1 = \frac{1}{2}(\omega_1 q_4 - \omega_2 q_3 + \omega_3 q_2) \tag{3.19}$$

$$\dot{q}_2 = \frac{1}{2}(\omega_1 q_3 + \omega_2 q_4 - \omega_3 q_1) \tag{3.20}$$

$$\dot{q}_3 = \frac{1}{2}(-\omega_1 q_2 + \omega_2 q_1 + \omega_3 q_4) \tag{3.21}$$

$$\dot{q}_4 = \frac{1}{2}(-\omega_1 q_1 - \omega_2 q_2 - \omega_3 q_3) \tag{3.22}$$

The controller will apply the maximum torque that is available in the rotation direction, until the halfway point for the manoeuvre is reached. This phase of the manoeuvre is referred to as the acceleration phase. Then the negative maximum torque is applied in order to bring the satellite to a zero angular rate during the deceleration phase. If any of the gimbal angles or wheel speeds reach their saturation limit during the acceleration phase, the torque will be zeroed. The satellite will then be allowed to continue to rotate, at a constant angular rate, for an equal amount of time before and after the halfway point for the manoeuvre is reached. This constant rotation rate phase may be referred to as the coasting phase. After this coasting phase, the deceleration phase is entered in order to stop the rotation of the satellite. The torque for these three phases is shown by (3.23) with Figure 3.5 showing a common torque, rate and angle profile of this type of manoeuvre around an eigenaxis.

$$\mathbf{N}_{\text{slew}} = \begin{cases} +s \min_i \left| \dfrac{N_{\text{max-}i}}{I_{ii} q_{ie}} \right| \text{diag}(\mathbf{I}) \mathbf{q}_{\text{vec}} & t \in \{t_0, t_h - 0.5t_c\} \\ 0 & t \in \{t_h - 0.5t_c, t_h + 0.5t_c\} \\ -s \min_i \left| \dfrac{N_{\text{max-}i}}{I_{ii} q_{ie}} \right| \text{diag}(\mathbf{I}) \mathbf{q}_{\text{vec}} & t \in \{t_h + 0.5t_c, t_f\} \end{cases} \tag{3.23}$$

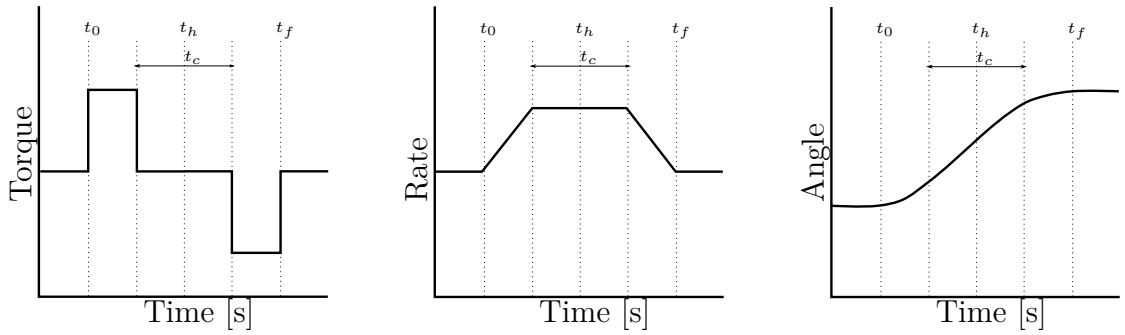

Figure 3.5: Bang-Off-Bang controller.

The quaternion $\mathbf{q}_{\text{vec}}$ is the first three elements of the error quaternion, $\mathbf{q}_e$, from (3.16). The scaling factor s is chosen as 0.9 in order to leave head room torque capability to compensate for disturbance torques experienced during the manoeuvre. The $\mathbf{N}_{\text{max}}$ vector is the maximum torque that can be achieved for each axis of the DGCMG and can be found by inspecting (3.14). The maximum torque for a CMG axis will be the maximum gimbal rate multiplied the maximum angular momentum the flywheel can achieve. This result must be doubled due to the two DGCMGs used. The Z-axis maximum torque will simply be the maximum change in angular momentum the wheels can achieve.

The equation finds the axis with the highest control effort required as the axis with the largest MOI, largest rotation error and smallest torque capability. The largest torque possible will be applied to this axis with proportionately scaled down torques applied to the axes with less control effort to ensure a rotation around the eigenaxis. This will prevent unnecessary power wasted on the other axes. The final deceleration phase can either end when the satellite body rates reach zero or after twice the time has elapsed as was needed to reach the halfway mark of the manoeuvre, but this might be inaccurate if disturbance torques are present.

The axis with the lowest torque capability will be the axis that relies on the wheels in reaction wheel mode. Therefore, it would be wise to have this axis of the actuator aligned with the axis of the satellite where no large angle slews will be performed.

Usually this would be the Z-axis of the satellite.

3.4 Quaternion Feedback Equations

At the end of a Bang-Off-Bang manoeuvre, there might be an offset angle due to disturbance torques or non-zero initial rates. To ensure a zero steady state error, a quaternion feedback (Q-feedback) regulator can be implemented. The Q-feedback method for eigenaxis manoeuvres as described by Wie *et al.* [30] is well known in attitude control industry. This controller closely resembles a classical PID or PD controller. The control torque can be calculated from the current angular rate, $\boldsymbol{\omega}_B^I$, and the quaternion error, $\mathbf{q}_{\text{vec}}$ as shown by (3.25).

$$\mathbf{N}_{\text{slew}} = \mathbf{K}\mathbf{q}_{\text{vec}} + \mathbf{D}\boldsymbol{\omega}_B^I \tag{3.24}$$

$$= 2\omega_n^2\mathbf{I}\mathbf{q}_{\text{vec}} + 2\zeta\omega_n\mathbf{I}\boldsymbol{\omega}_B^I \tag{3.25}$$

Where ω_n is the natural frequency that determines the slew settling time and ζ is the damping ratio that determines the overshoot. An optional integral term can be added to improve steady state error as shown by (3.26).

$$\mathbf{N}_{\text{slew}} = \mathbf{K}\left(\mathbf{q}_{\text{vec}} + \frac{1}{T}\int \mathbf{q}_{\text{vec}}\right) + \mathbf{D}\boldsymbol{\omega}_B^I \tag{3.26}$$

Where T is the sampling time chosen as 0.1 s in the previous chapter.

3.4.1 Saturation Logic

When any of the gimbal angles or motor speeds reach their saturation values, the integral term will keep increasing in magnitude in what is referred to as integral wind-up. Therefore the commanded torque must be bounded by the DGCMG torque capabilities. Wie shows how simple logic can be added to the steering law in (3.26) to avoid saturation as shown by (3.28) from [18].

$$\mathbf{N}_{\text{slew}} = \mathbf{K}\underset{L_i}{\text{sat}}\left(\mathbf{q}_{\text{vec}} + \frac{1}{T}\int \mathbf{q}_{\text{vec}}\right) + \mathbf{D}\boldsymbol{\omega}_B^I \tag{3.27}$$

$$= 2\omega_n^2\mathbf{I}\underset{L_i}{\text{sat}}\left(\mathbf{q}_{\text{vec}} + \frac{1}{T}\int \mathbf{q}_{\text{vec}}\right) + 2\zeta\omega_n\mathbf{I}\boldsymbol{\omega}_B^I \tag{3.28}$$

Where:

$$\underset{X_{\max},X_{\min}}{\text{sat}}(x) = \begin{cases} X_{\max} & \text{if } x > X_{\max} \\ x & \text{if } X_{\min} < x < X_{\max} \\ X_{\min} & \text{if } x < X_{\min} \end{cases} \tag{3.29}$$

$$L_i = \frac{\zeta}{\omega_n}\min\left\{\sqrt{1.6\frac{N_{\text{max-}i}}{I_{ii}}|q_{\text{vec}-i}|}, |\omega_{B-i}^I|_{\max}\right\} \tag{3.30}$$

This logic will also ensure that the slew rate does not exceed a predefined maximum satellite body rate as given by $|\omega_{B-i}^I|_{\max}$. This maximum body rate is defined for satellites that have large deployed antennas or solar arrays that flex during slew manoeuvres. This flexing may cause the control system to enter an unstable oscillation [18].

3.4.2 Summary

To summarise, this chapter gives an introduction to the reference frames used for attitude control as well as different methods of representing orientations in those reference frames. The DGCMG configuration is analysed to build a mathematical model of the torques that it can generate. The chapter concludes by presenting two attitude controllers that will be implemented on the DGCMG configuration. With these attitude controllers and the torque model, slew simulations can now be performed and compared to hardware slew tests.

Chapter 4

Practical Measurements

In previous chapters the proposed DGCMG have been analysed and constructed. A mathematical model has been created in order to create an attitude controller with this DGCMG and now it is required to test the performance of this DGCMG and confirm that the model is an accurate representation of the hardware. The tests must include power, torque and pointing accuracy measurements in order to compare the DGCMG with the specifications of Chapter 1.

4.1 Method and Setup

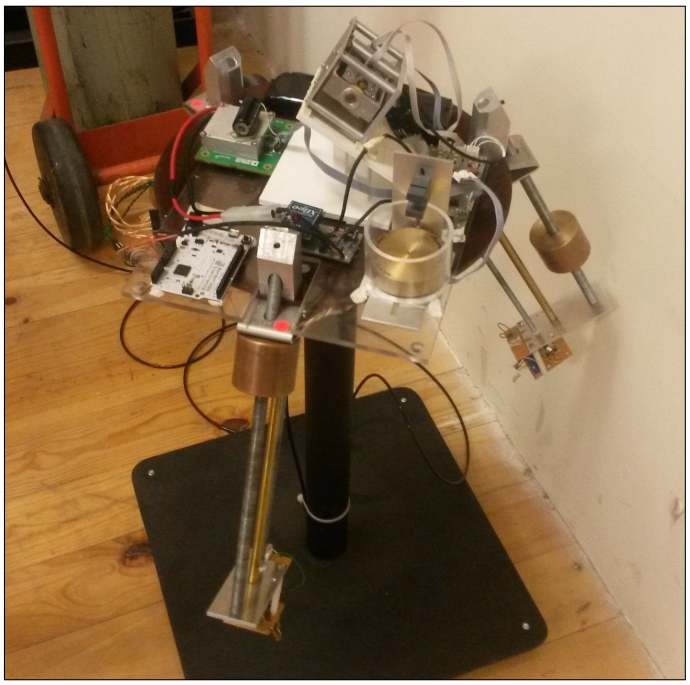

Figure 4.1: Setup on air bearing.

In order to test the DGCMG, a near zero friction environment is required. This can be achieved with the use of an air bearing. Figure 4.1 shows the actual hardware setup on the air bearing with all the components necessary for a slew test located on the platform. The air bearing consists of a platform mounted on a perfectly round ball that rests in a socket. Inside the socket is several nozzles connected to a pressurized nitrogen supply. This effectively causes the ball to float inside the socket with very little friction. The use of nitrogen is due to its large molecular mass that will result in lower effusion rate according to Graham's Law. By placing the DGCMG on this air bearing, a single axis can be tested with a slew manoeuvre. If the centre of mass of the platform and DGCMG setup can be exactly centred with the ball centre of rotation, three-axis slews can also be tested for small angles as done by Chesi [31]. Figure 4.2 shows a simple diagram of the air bearing with DGCMG setup that clarifies the location of all the components.

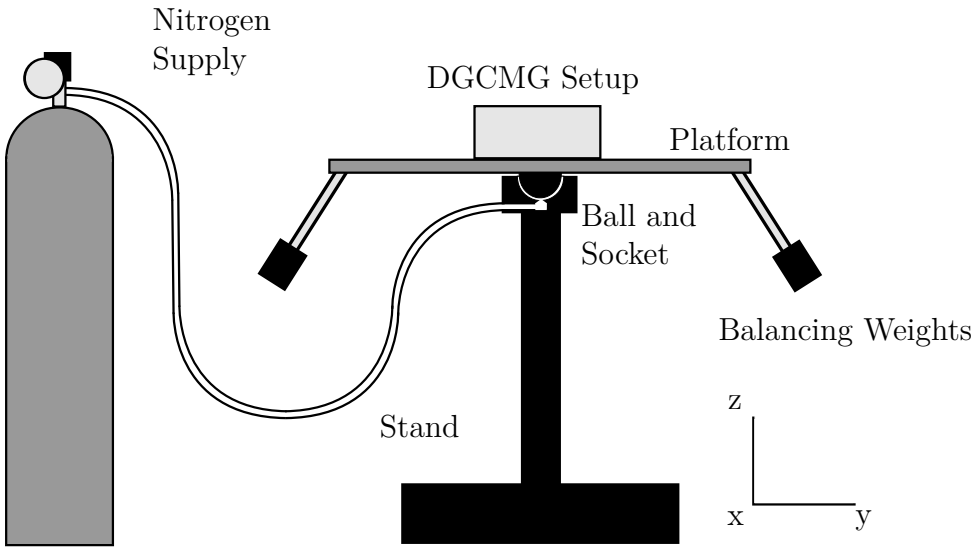

Figure 4.2: Air bearing with DGCMG setup.

The ball surface is not perfectly smooth and in practice, it was found that the air bearing do provide small disturbance torques to the system due to the flow of gas over the ball. The motion of the platform is measured using a MEMS inertial measurement unit as described in Section 2.4. This sensor provides angular rates that can be integrated to find actual slew angles. After each of the slew manoeuvres, the final angle is verified using a laser pointer mounted on the platform that projects on a wall next to the air bearing setup. With simple trigonometry, the angle can then be calculated.

To balance the platform before a manoeuvre, the sensor readings as well as a spirit level was used, but when the platform was released, some motion was still observed.

The centre of mass of the platform and DGCMG setup was in all cases below the centre of the ball and any slight misalignment of this centre of mass with the ball-socket pressure point will cause a pendulum motion after initial release. Previous hardware development was done on automatic balancing rods to shift the centre of mass towards the centre of rotation, but further work should be done on this system for operational use.

4.1.1 Moment of Inertia Determination

The moment of inertia of the air bearing and DGCMG combination is needed in order to perform accurate slew manoeuvres. Especially for the Bang-Off-Bang controller that does not contain integration control and may leave a large angle offset for the Q-feedback controller to correct. To determine the moment of inertia, the DGCMG is mounted with the wheel spin axis aligned to the air bearing Z-axis and an angular rate input is applied to both wheels in the same direction. The wheel moment of inertia is known and the air bearing rotation rate is measured with the inertial measurement unit. With (4.1), the moment of inertia can be calculated for the air bearing in the Z-axis when the combined setup starts from rest.

$$\begin{aligned} \Delta \mathrm{h}_{\mathrm{wheels}} + \Delta \mathrm{h}_{\mathrm{platform}} &= 0 \\ I_{\mathrm{wheels}} \Delta\omega_{\mathrm{wheels}} + I_{\mathrm{platform}} \Delta\omega_{\mathrm{platform}} &= 0 \\ I_{\mathrm{platform}} &= -\frac{I_{\mathrm{wheels}} \Delta\omega_{\mathrm{wheels}}}{\Delta\omega_{\mathrm{platform}}} \end{aligned} \tag{4.1}$$

This test was done several times to confirm the Z-axis MOI value. A larger momentum wheel was also used to minimize the error that may be introduced by inaccurate wheel MOI values. With this MOI value, the **I** matrix was built and used in the control system design. The X- and Y-axis MOI values were left as zero and the products of inertia were ignored. This is allowed due to only Z-axis rotations being performed on the air bearing. In a satellite application, the products of inertia may cause wobble around the centre of mass during slew manoeuvres. Therefore, the design layout of the satellite should attempt to minimize the products of inertia even at the cost of adding ballast weight.

4.2 Example Manoeuvre

The model of the DGCMG was simulated for a slew manoeuvre of 30 degrees in each axis. This slew manoeuvre was then tested on the air bearing. The actual MOI of the

air bearing was used during all simulations to properly compare the final results. In order to test multiple axes of the DGCMG at once, the DGCMG was also mounted at an angle on the air bearing platform. This angle is equal to an Euler 1-2-3 rotation of 30° roll, −20° pitch and 0° yaw. The controller can easily be modified by multiplying the angular momentum of the system in (3.11) with a DCM as shown by (4.3). The Jacobian matrix and slew torque matrix can again be re-calculated the same way as in (3.14) and (3.15).

$$\begin{aligned}\mathbf{C}_{\mathrm{A}}^{\mathrm{P}} &= \begin{bmatrix}\cos(-20°) & 0 & -\sin(-20°)\\ 0 & 1 & 0\\ \sin(-20°) & 0 & \cos(-20°)\end{bmatrix}\begin{bmatrix}1 & 0 & 0\\ 0 & \cos(30°) & \sin(30°)\\ 0 & -\sin(30°) & \cos(30°)\end{bmatrix}\\ &= \begin{bmatrix}0.9397 & -0.1710 & 0.2962\\ 0 & 0.8660 & 0.5000\\ -0.3420 & -0.4698 & 0.8138\end{bmatrix} \qquad (4.2)\end{aligned}$$

$$\mathbf{h}'_{\mathrm{total}} = \mathbf{C}_{\mathrm{A}}^{\mathrm{P}} \cdot \mathbf{h}_{\mathrm{total}} \qquad (4.3)$$

4.3 Simulation Setup

The simulation was done from the Matlab Simulink environment with the use of an S-function as the controller. This S-function receive rate feedback and produce a new state vector for the DGCMG. These states were fed into a model of the DGCMG on the air bearing. The model in turn produced an estimated angular rate for controller to receive.

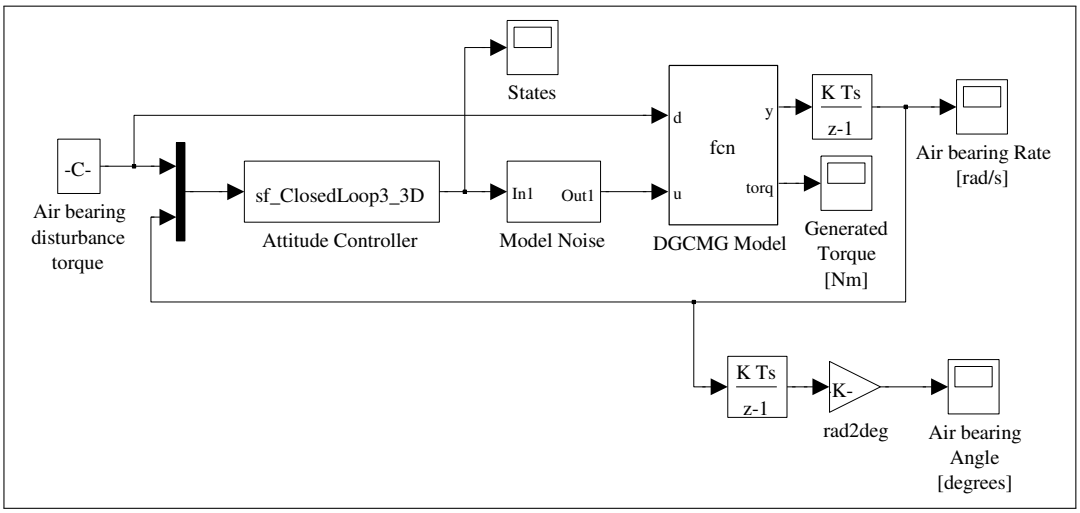

Figure 4.3: Simulation block diagram.

Figure 4.3 shows the block diagram used to collect the simulation data. The 'Model Noise' block contains several adjustments to the controller states to have them more closely fit real-world values and saturation limitations. The stepper angles were given backlash inaccuracy as described in Section 2.3.1. The stepper rates were achieved using integer clock dividers in the microcontroller for the step pulse generators. Therefore the received rates were rounded to the nearest achievable rate. This gimbal angular rate inaccuracy was also modelled in the noise block. Noise and saturation limits were also added to the flywheel speeds as measured during tests. An attempt was made to model the flywheel dynamic imbalance with a sinusoidal torque with a frequency equal to the rotation speed. This would require a very small simulation time step to simulate this high frequency sinusoidal torque. However due to difficulty in determining this imbalance, this torque was neglected. Bearing, BLDC motor and driver disturbances were also not included for the same reason. In the simulation diagram, the model of the DGCMG on air bearing were easily switched with an S-function to send the state commands via the serial COM port to the actual hardware in order to perform Hardware-in-the-Loop (HIL) tests. This HIL block diagram is shown in Figure 4.4.

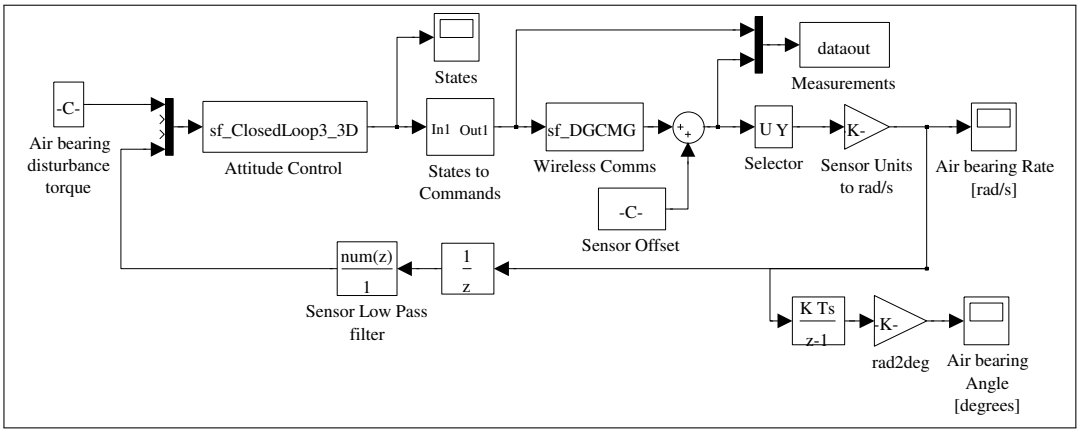

Figure 4.4: HIL block diagram.

In this diagram the states are translated to PWM and step commands that can be sent to the air bearing. The rate measurements received were adjusted according to calibration done before the manoeuvre was performed, and stored for analysis. A low pass filter was added to remove noise from the sensor measurements. This does add additional poles and zeros to the system, but their effect was only used to prevent constant stepper jitter. An example of the effect of this filter is shown in Figure 4.5. For accuracy, the unfiltered data was used to determine the total slew and the torque developed. For the data plots displayed in the next section, the torque and rate data was filtered to improve readability. This ensured that the torque measurements

calculated by differentiating the air bearing rates did not amplify the noise present on the sensor.

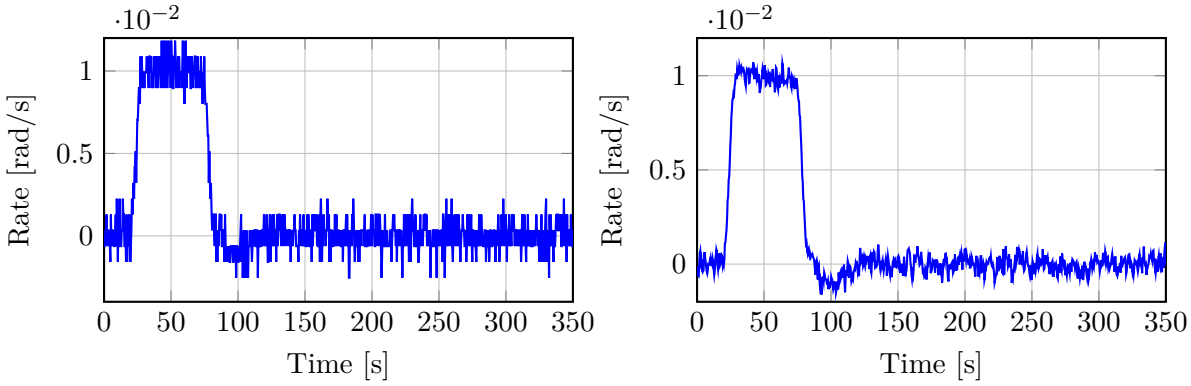

(a) Unfiltered air bearing rate.

(b) Filtered air bearing rate.

Figure 4.5: Unfiltered versus filtered sensor measurements.

The delay block was required to prevent algebraic loop errors in Simulink. Algebraic loop errors often occur when virtual model blocks are dependant on hardware components for input.

4.4 Observations

The first manoeuvre was for a yaw rotation. For this rotation the DGCMG was placed on the platform with the flywheel spin axis aligned with the air bearing axis of rotation. This manoeuvre only used the wheels in order to generate a torque. In Figure 4.6a, 90% of the maximum torque was applied at $t = 20\,\text{s}$ until the wheel speed saturated as shown in Figure 4.6b at $t = 30\,\text{s}$. The wheel speed follows the commanded speed with a constant error for a ramp command and caused a delay in the generated torque that can be noticed in the graph. The air bearing was then allowed to rotate at a constant angular rate for an equal amount of time before and after the midway point as seen in Figure 4.6c, before the same torque profile was applied in the negative direction as shown in Figure 4.6a at $t = 105\,\text{s}$. This resulted in an approximate 30° rotation in near minimum time. The Q-feedback controller was then activated to ensure a zero steady state error as seen in Figure 4.6d after $t = 130\,\text{s}$. The 2% settling time for this yaw manoeuvre is 92.9 s.

The next manoeuvre was for a pitch rotation. For this manoeuvre the DGCMG was placed on the air bearing with the outer gimbal rotation axis aligned with the rotation axis of the air bearing. The moment of inertia measured for this manoeuvre and

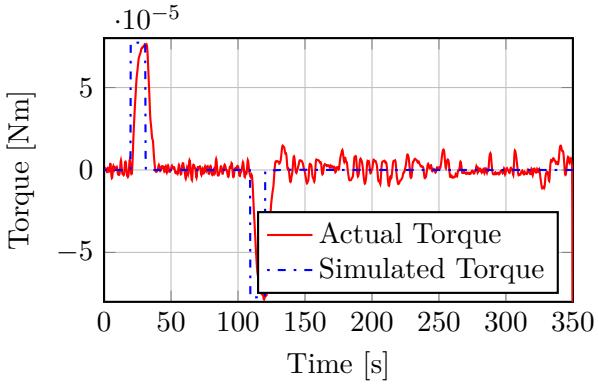

(a) Yaw control torque.

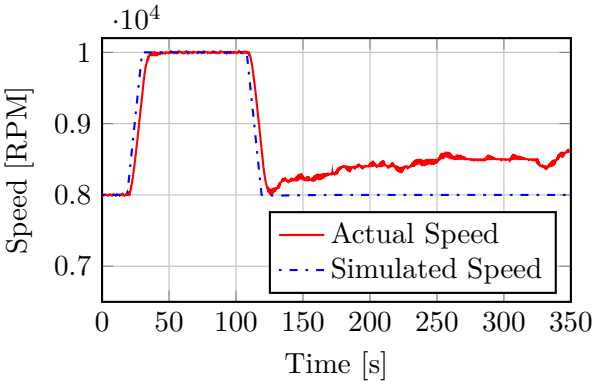

(b) DGCMG single flywheel speed.

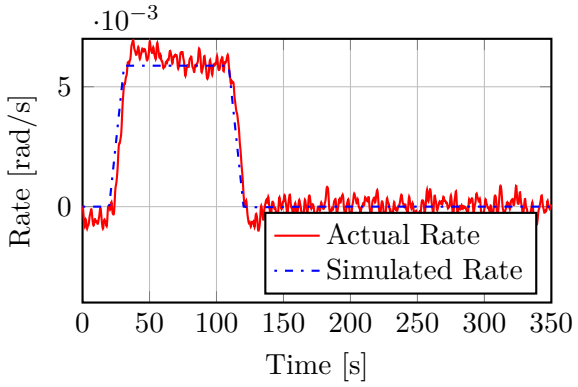

(c) Air bearing rate for yaw.

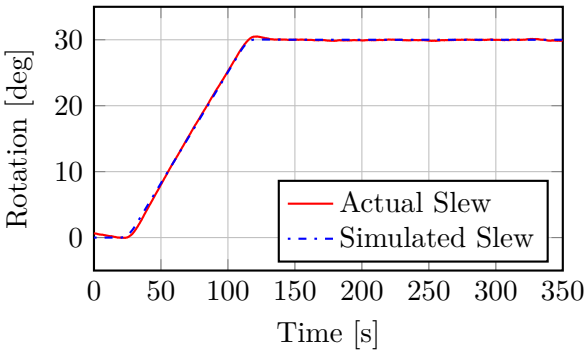

(d) Air bearing angle for yaw.

Figure 4.6: Test results for 30° yaw manoeuvre.

the yaw manoeuvre was nearly identical and therefore the slew times can be directly compared. During this manoeuvre, only the inner gimbals rotated around the DGCMG X-axis. Again the Bang-Off-Bang controller was applied to achieve a near minimum time slew followed by the Q-feedback controller to achieve zero steady state error. The use of CMGs allowed for a much larger torque to be applied to the platform as seen in Figure 4.7a. Due to the scaling factor, s, in (3.23) and the friction torque on the air bearing, the torque achieved during the test was 0.52 mN m which is less than the calculated 0.58 mN m in Chapter 2. Unfortunately the gimbal angle quickly reached its mechanical limit at $t = 25$ s, as seen in Figure 4.7b, and no torque could be applied further. Figure 4.7d shows that the manoeuvre was still noticeably faster than that of the yaw rotation with a 2% settling time 44.6 s.

The roll manoeuvre was similar to the pitch manoeuvre, but now the DGCMG X-axis was aligned with the air bearing rotation axis and the outer gimbals were rotated

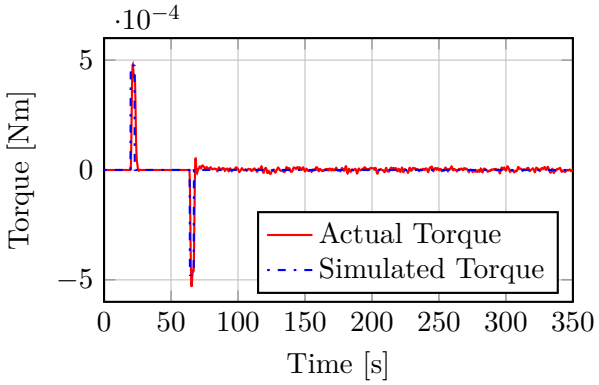

(a) Pitch control torque.

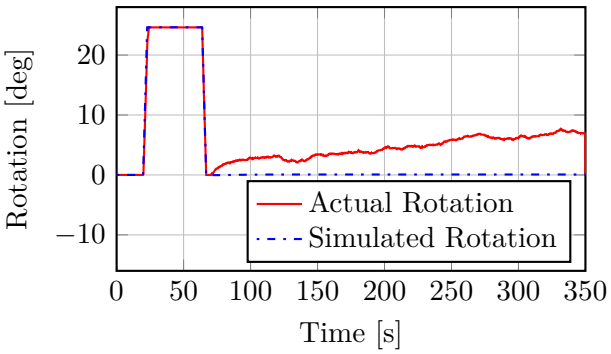

(b) X-Axis gimbal rotation.

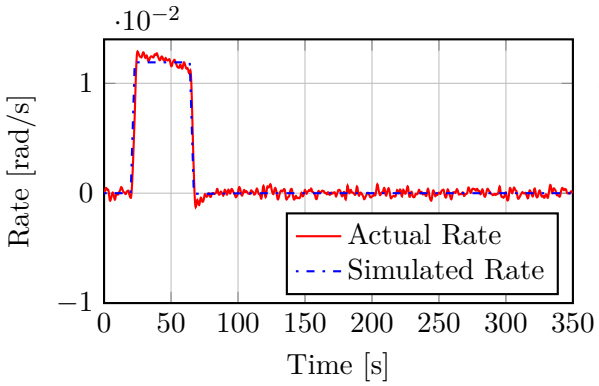

(c) Air bearing rate for pitch.

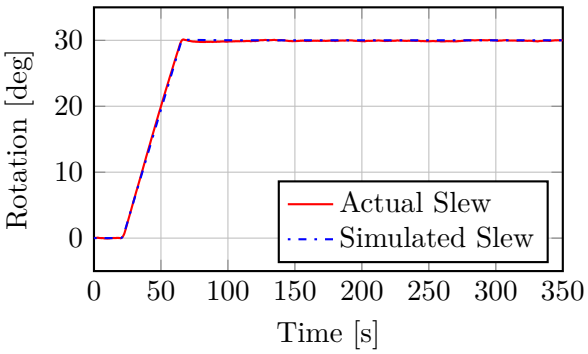

(d) Air bearing angle for pitch.

Figure 4.7: Test results for 30° pitch manoeuvre.

to provide the correct torque.

In Figures 4.6b and 4.7b it can be seen that the flywheel speed and the gimbal rotation were not zero during the Q-feedback controller operation. These deviations from the simulated values were caused by disturbance torques on the air bearing rejected by the controller. This caused momentum build-up on the DGCMG. If the pointing vector was held for longer without any momentum dumping, the platform would have begun to rotate as the actuator became saturated. To determine the momentum storage of this DGCMG configuration, the mechanical saturation values can be entered into the equation for the total angular momentum, (3.11), and this will provide the theoretical values:

$$\mathbf{h}_{\max} = \begin{bmatrix} 1.451 \\ 1.451 \\ 0.858 \end{bmatrix} \quad [\text{mN m s}]$$

By examining the duration of the torque profiles in Figures 4.6a and 4.7a, the momentum storage was measured as:

$$\mathbf{h}_{\max} = \begin{bmatrix} 1.432 \\ 1.431 \\ 0.863 \end{bmatrix} \quad [\text{mN m s}]$$

4.4.1 Momentum Dumping

To prevent the DGCMG from reaching angular momentum saturation, the magnetic torquer rods can continuously be used to dump momentum. Due to the singularity free properties of this DGCMG configuration, momentum dumping will be simpler than with a SGCMG design. In order to utilize the torquer rods that were discussed in Chapter 1, the earth's magnetic field, $\mathbf{B}_E$, at the current orbit position is required. This can be measured by a magnetometer or estimated from a propagation model. The torque, $\mathbf{N}$, produced by the torquer rods is perpendicular to the magnetic field and the magnetic dipole moment, $\mathbf{M}$, as shown in (4.4).

$$\mathbf{N} = \mathbf{M} \times \mathbf{B}_E \tag{4.4}$$

From [18] a simple momentum dumping algorithm is given with command torques for the rods, $\mathbf{N}_c$, given by (4.5).

$$\mathbf{N}_c = -\mathbf{K} \cdot \mathbf{h}_{\text{total}} \tag{4.5}$$

Where $\mathbf{K}$ is the dumping gains that are determined with simulations and $\mathbf{h}_{\text{total}}$ is the angular momentum of the DGCMG system. The commanded torque can then be used with a cross-product controller to find the torquer rod dipole moment reference as shown by (4.6).

$$\mathbf{M} = \frac{\mathbf{B}_E \times \mathbf{N}_c}{|\mathrm{B}_E|^2} \tag{4.6}$$

4.4.2 Three-Axis Control Test

In order to test a true three-axis manoeuvre, the DGCMG was mounted at an inclination on the air bearing platform. The controller was changed with a mounting DCM as previously calculated in (4.3). All gimbals including the flywheel speeds were utilized during this rotation as seen in Figures 4.8a to 4.8c.

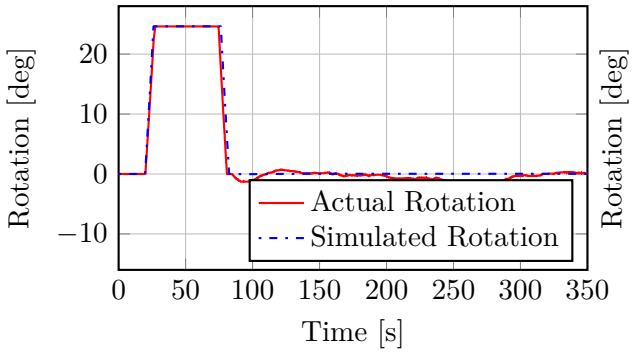

(a) Inner gimbal rotation.

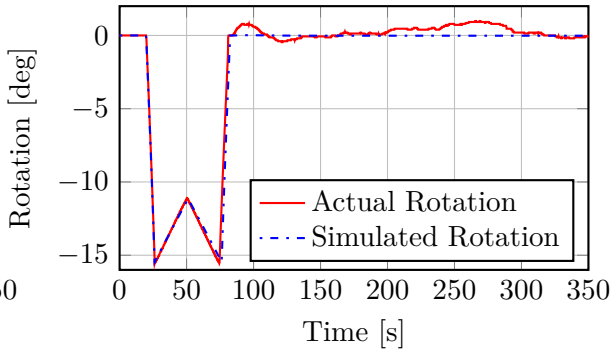

(b) Outer gimbal rotation.

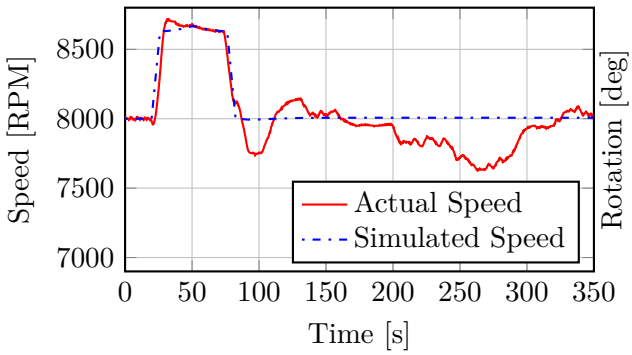

(c) Speed of single flywheel.

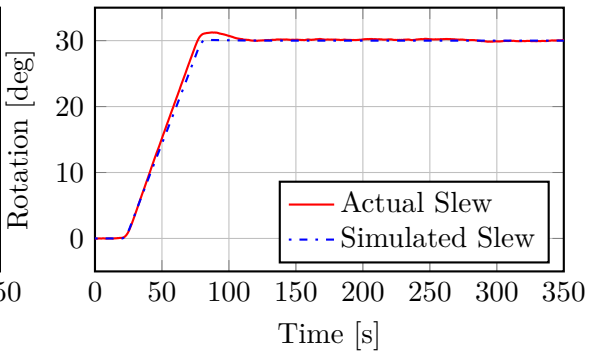

(d) Air bearing angle for three-axis slew.

Figure 4.8: DGCMG states during three-axis manoeuvre.

The purpose of this test was to verify that all hardware can function in unison and also show the effects of hardware misalignment. In Figures 4.9a to 4.9c the torque in each axis of the DGCMG reference frame is shown.

These combined CMG torques produced a rotation in the Z-axis in the air bearing frame. The rate of the air bearing Z-axis, as shown in Figure 4.9d, were integrated to find the slew seen in Figure 4.8d.

Figure 4.10 shows the air bearing rotation in the X- and Y-axis. From this figure it is evident that there was a high frequency oscillation of the air bearing platform due to the platform being non-level and the centre of mass not aligned with the swivel point

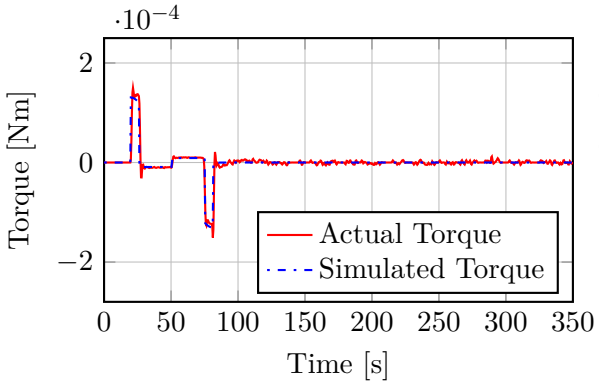

(a) Torque in DGCMG referenced X-axis.

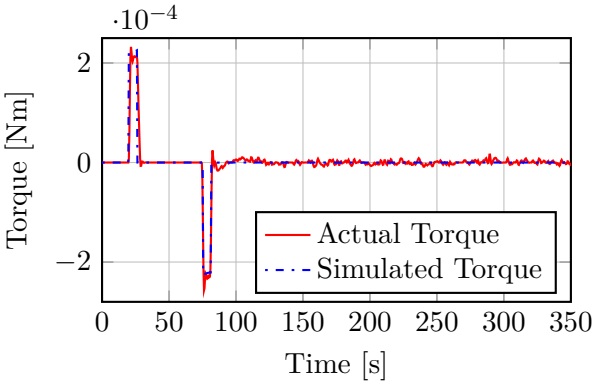

(b) Torque in DGCMG referenced Y-axis.

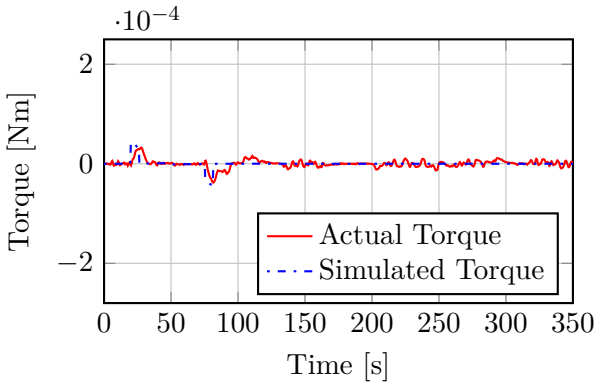

(c) Torque in DGCMG referenced Z-axis.

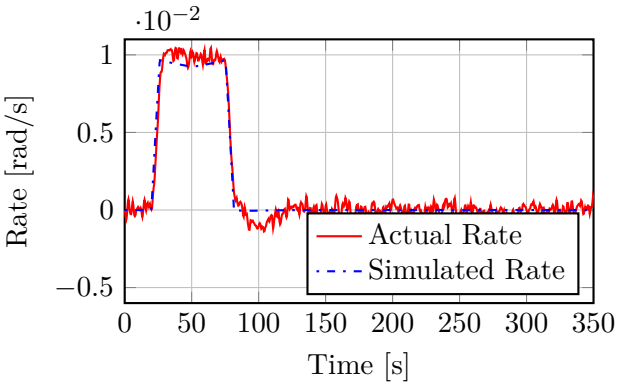

(d) Air bearing rate for three-axis slew.

Figure 4.9: DGCMG states during three-axis manoeuvre.

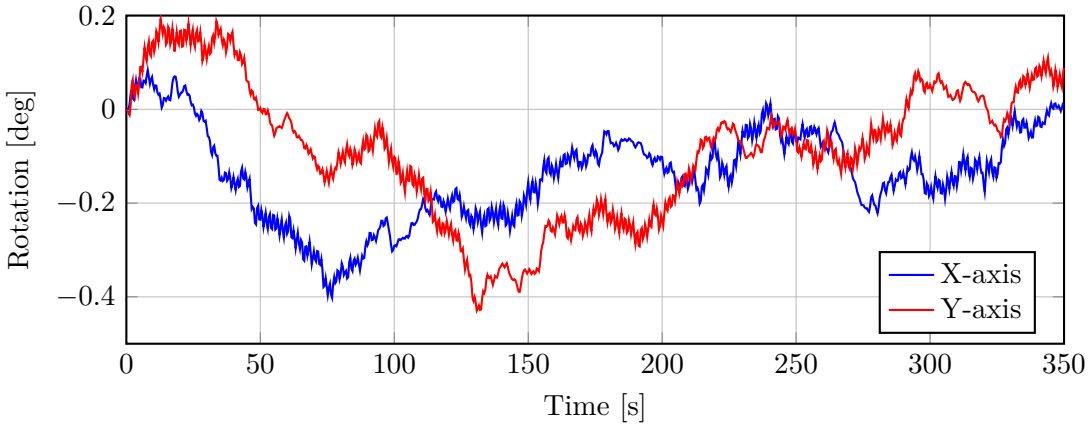

Figure 4.10: Air bearing rotation in X- and Y-axis.

when released. This motion is similar to pendulum motion. The figure also shows that there was a slight rotation in the X- and Y-axis during the slew manoeuvre between

$t = 20\,\text{s}$ and $t = 100\,\text{s}$. This indicates that there is small hardware misalignment in the setup that causes cross coupling torques. The control system will reject these torques, but this illustrates that the mechanical manufacturing process needs to be perfect.

4.5 Power Consumption

A major concern for any space flight hardware is power consumption. The power for the DGCMG was measured for the three-axis manoeuvre in Figure 4.8d. The measurement was done for the entire control board. This included the Hall sensors, microcontroller, XOR gates, steppers and BLDC motors. The power for the MEMS gyroscopic sensor and wireless communication were not included in any power measurements. All power measurements were obtained from an INA139 current sensor by Texas Instruments and filtered, using a $1\,\mu\text{F}$ capacitor.

When the BLDC motors and all the steppers were switched off, the average power usage was $105\,\text{mW}$. This is the power consumption of the microcontroller, XOR gates, drivers and other supporting ICs. With the three steppers switched on to hold a position, the total power usage increased to an average of $302\,\text{mW}$. At the nominal rate of 8000 RPM for each BLDC motor, the total power usage again increased to an average of $420\,\text{mW}$. With all steppers running at the maximum allowed rate the power usage averaged $556\,\text{mW}$.

By comparing the power usage in Figure 4.11b with the torque of all axes of the DGCMG, there is a clear correspondence. Therefore power usage can be greatly reduced by using less torque for manoeuvres that are not time critical. The peak power usage during the three-axis manoeuvre was measured as $554\,\text{mW}$ with an average of $420\,\text{mW}$ and is shown in Figure 4.11b.

As a method to evaluate the performance of the DGCMG, additional tests were performed on a traditional momentum wheel. The momentum wheel consists of a similar BLDC motor and was driven by the same driver setup as used to accelerate the DGCMG flywheels. The wheel has a MOI around its spin axis of $4.7117 \times 10^{-5}\,\text{kgm}^2$ and a maximum torque of $2.1\,\text{mN m}$ and is shown in Figure 4.12.

In order to properly compare this momentum wheel with the DGCMG, the torque was scaled down until the settling time for the two test slews were equal. The momentum wheel showed poor reference tracking performance at low rotation rates, but greatly improved when a momentum bias was added to the wheel. This was done by spinning the wheel to a rate of 500 RPM while preventing the air bearing platform from rotating. Figure 4.13a shows the torque profile necessary to perform a slew shown in Figure 4.13b. Notice that this slew has a settling time of $85\,\text{s}$ that is very close to that

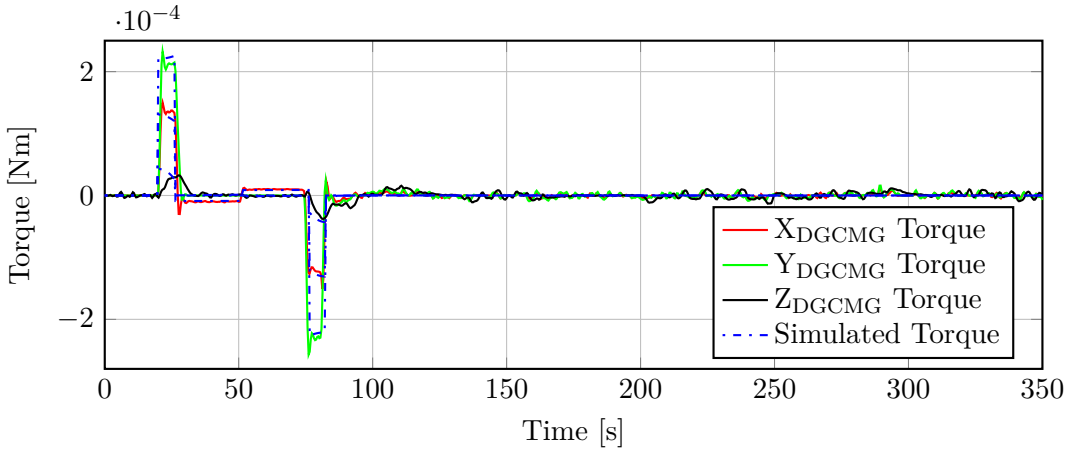

(a) Torque output of DGCMG during three-axis slew.

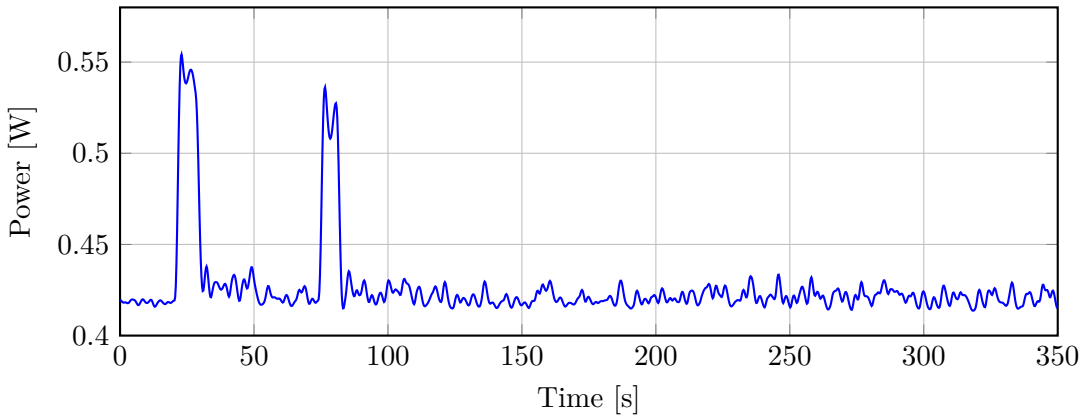

(b) DGCMG total power usage during three-axis slew.

Figure 4.11: Power usage relating to torque output of DGCMG.

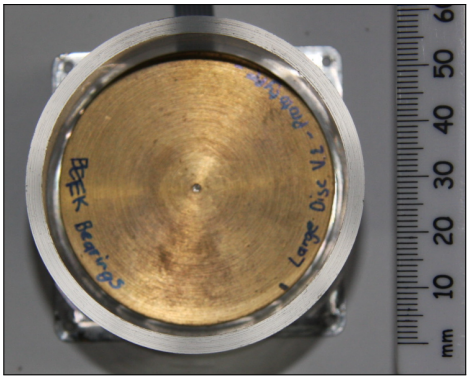

(a) Large momentum wheel top view.

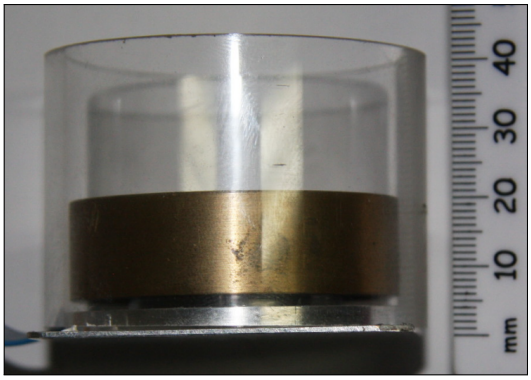

(b) Large momentum wheel side view.

Figure 4.12: Large momentum wheel in protective acrylic housing.

of the DGCMG three-axis slew. Figure 4.13c shows the power usage of the momentum wheel test. From this power curve the maximum power usage was 380 mW and the average usage is 352 mW. This is less than that of the DGCMG, but it should be kept in mind that the DGCMG was tested for a three-axis manoeuvre where three momentum wheels would be required. If the power usage of the microcontroller and other supporting components remain the same as with the DGCMG test, the average power usage of the wheel alone would be 247 mW. This is higher than the 150 mW value given in the datasheet found in Appendix C. With three wheels and each momentum biased at 500 RPM, the average power usage would be approximately 846 mW. The wheel performs worse at higher torque and shows that the power usage does not scale linearly.

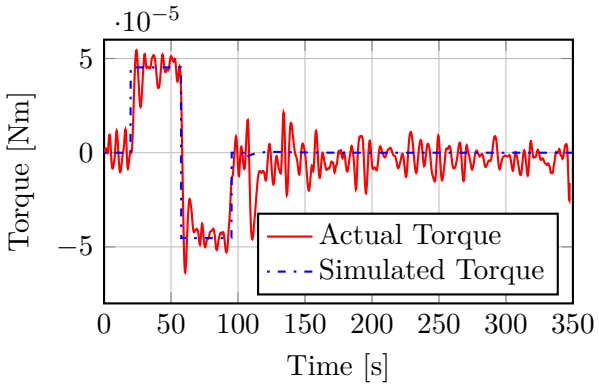

(a) Torque generated by large wheel.

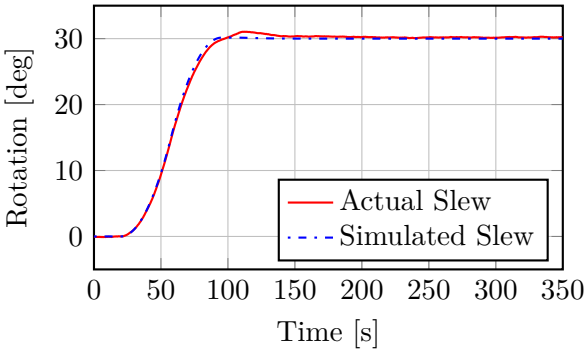

(b) Air bearing angle for large wheel slew.

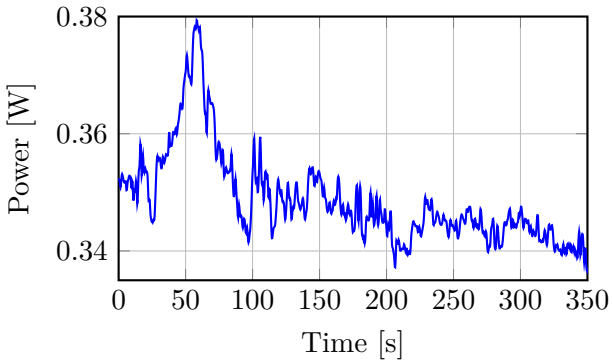

(c) Large wheel total power usage.

Figure 4.13: Yaw simulation using Q-feedback controller and zero disturbance torque.

4.6 Pointing Accuracy

In Chapter 2.3.1 the tolerance of the gear design is discussed and the gimbal angle resolution was found to be 0.066° and 0.067° for the inner and outer gimbals. The backlash in the gears may cause a gimbal angle deviation of up to 0.896°. The backlash, stepper rates and angle resolution were modelled as noise in the simulations shown in Figure 4.3 in Chapter 4.3. This noise will cause angle deviations in the final slew. The maximum deviation in the simulations and the maximum deviation during the HIL test are shown in Table 4.1.

Table 4.1: Pointing Accuracy Results.

Air Bearing MOI [kgm^2]	**Simulated Maximum Deviation [deg]**	**Actual Maximum Deviation [deg]**	**Actual Variance [deg]**
0.1234	0.0624	0.17	0.004
0.1301	0.0592	0.18	0.003
0.1374	0.0561	0.14	0.004
0.1534	0.0505	0.10	0.002

The test was repeated for different MOI values by adding mass to the air bearing. From the table it shows that the deviation decreased with increased MOI due to larger disturbances required for acceleration. There are large differences between the simulated deviation and the measured deviation. The measured deviation was largely introduced by sensor noise, but can also be attributed to unmodelled disturbances in the DGCMG system or disturbances on the air bearing ball-socket surface. The pointing accuracy experienced in orbit will be vastly different than these measurements and therefore only actual flight tests can determine the true values.

When the deployed optics in [3] is considered at a 500 km altitude as illustrated in Figure 4.14, the ground coverage is approximately 6.1 km × 4.6 km. The satellite used as a platform for this Peregrine telescope is FalconSat-7 [32] with a mass of 5 kg and a 3U body. With the deployed telescope, the maximum MOI axis for this satellite will be approximately 0.08 kgm^2. If we assume the pointing accuracy experienced in orbit is similar to the values measured on the air bearing, such a small MOI will have approximately 0.18° of pointing accuracy. With such a pointing accuracy and the assumption that the satellite orbit position is exactly known, the aim point on the earth surface will deviate by approximately 1.57 km. Therefore the target will still be within the bounds of the image produced. The target will only start falling outside the coverage area at an inaccuracy of 0.53°. If a line scanning imaging sensor is used, there

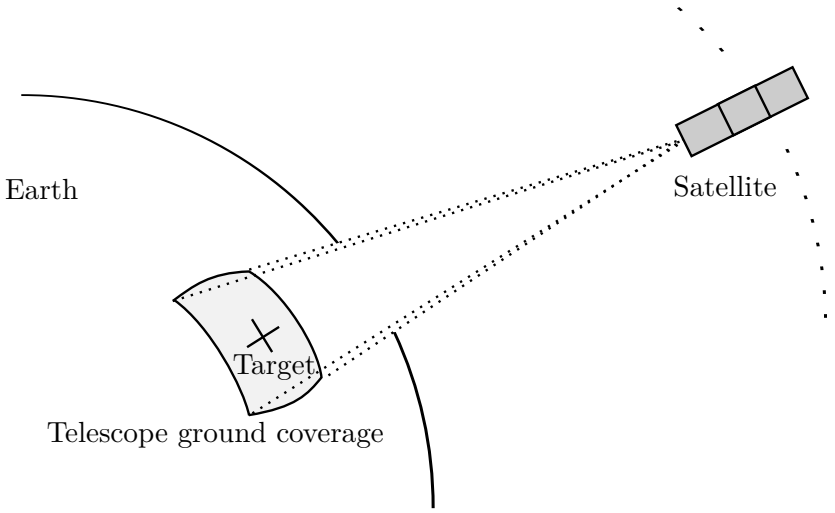

Figure 4.14: Imaging satellite ground coverage.

will be significant distortion on the image caused by the deviation. The maximum deviation is often referred to as attitude jitter. Long exposure images may also suffer distortion caused by this jitter. A method to reduce such distortion is to perform the slew manoeuvre to the desired angle and dump momentum with the magnetic torquer rods to bring the gimbal angles back to zero. This allows the system to safely decelerate both flywheels to achieve a near motionless platform before imaging commences. The dumping duration will be long and therefore this method may not be practical due to the presence of external disturbance torques, but may allow the flywheel speed to be decreased for less jitter.

Chapter 5

Conclusion

In this chapter all the results from previous chapters are combined into a final specification for the DGCMG and compared to existing technology. The current design is still a prototype developed for this thesis and several improvements are suggested.

5.1 Results

From Chapters 2 and 4 the design and measurement results have shown that the final DGCMG have the following specifications:

- Maximum momentum storage of 1.43 mN m s in a CMG axis
- Torque capability of 0.52 mN m in a CMG axis
- Peak power usage of 556 mW with average of 420 mW
- Total mass of 260 g
- Size of 47 mm×49.5 mm×94 mm

These specifications are close to those outlined in Chapter 1, but unfortunately the 30° slew could only be completed at a minimum time of 44.6 s for a 12U equivalent MOI. This will give an average slew rate of 0.67 °/s that just falls short of the agile requirement set in the specifications. The slew rate for a 3U CubeSat can be calculated with (5.6). For these equations it is assumed that the torque, $N = 0.52\,\text{mN m}$, remains constant during the small gimbal rotation of $\delta_{\text{max}} = 25°$ with a gimbal rate of $0.17\,\text{rad s}^{-1}$.

$$t_{\max} = t_{\text{accel}} = t_{\text{decel}} = \frac{\delta_{\max}}{0.17} = 2.6\,\text{s} \tag{5.1}$$

$$\dot{\theta}_{\max} = \frac{N}{I} t_{\max} = 2.33\,^{\circ}\,\text{s}^{-1} \tag{5.2}$$

$$\theta_{\text{accel}} = \theta_{\text{decel}} = 0.5\frac{N t_{\max}^2}{I} = 3.03^{\circ} \tag{5.3}$$

$$\theta_{\text{coast}} = 30^{\circ} - 2\theta_{\text{accel}} = 23.94^{\circ} \tag{5.4}$$

$$t_{\text{coast}} = \frac{\theta_{\text{coast}}}{\dot{\theta}_{\max}} = 10.3\,\text{s} \tag{5.5}$$

$$t_{\text{total}} = t_{\text{coast}} + 2t_{\max} = 15.5\,\text{s} \tag{5.6}$$

The acceleration, coasting and deceleration phases will last for t_{accel}, t_{coast} and t_{decel} respectively. These durations are rounded to the nearest sampling period by the control system. The actuator will therefore be able to provide agile manoeuvrability to a 3U CubeSat.

The final efficiency values for this actuator is $\eta_P = 9.35 \times 10^{-4}\,\text{Nm/W}$, $\eta_M = 2.0 \times 10^{-3}\,\text{Nm/kg}$ and $\eta_V = 2.38\,\text{Nm/m}^3$. Table 5.1 shows the efficiency of the DGCMG actuator compared with efficiency ratings for other commercially available CubeSat actuators. All these values are for three-axis control configurations. These efficiency ratings show that the DGCMG performs well when compared to similar sized CMG based actuators. Some of the other actuators may have better efficiency ratings, but the zero singularity and zero momentum bias of this DGCMG are a major advantage.

Table 5.1: Actuator Efficiency Values.

Actuator	**Power Efficiency [Nm/W]**	**Mass Efficiency [Nm/kg]**	**Volume Efficiency [Nm/m^3]**
DGCMG	9.35e-4	2.00e-3	2.38
Nagabhushan's Pyramid	2.67e-4	1.80e-3	1.60
Honeybee SGCMGs	1.12e-2	3.61e-2	47.5
Schoonwinkel Tetrahedral	7.86e-4	6.70e-3	3.18
Maryland Unit	4.92e-5	9.92e-4	1.56
Large ESL Wheel	3.89e-4	4.30e-3	7.71
Small ESL Wheel	1.50e-4	1.70e-3	4.31

When comparing this DGCMG with Nagabhushan's pyramid configuration, it is shown that the power, mass and volume efficiencies are higher for the DGCMG. However, the larger SGCMGs of Honeybee are far more efficient in power, mass and volume.

The DGCMG is more power efficient than all the three-axis momentum wheel configurations that were compared. The DGCMG will also provide redundancy as discussed in Chapter 2. However, the DGCMG were only more efficient in mass than the three-axis configuration of small ESL wheels and the three-axis Maryland unit. When comparing the volume efficiency of the DGCMG to the three-axis momentum wheel configurations, the DGCMG only performed better than the Maryland unit.

The pointing accuracy measurements appear to be very good, but it should be reiterated that this is obtained from a noisy inertial measuring unit and an air bearing platform that inherently have some friction and disturbance torque due to air flow variations.

The test results have shown that the mechanical complexity does translate to difficulty in manufacturing, but with modern computer machining the tolerance can be lowered.

5.2 Future Improvement

The DGCMG built for this thesis is a prototype and can be improved considerably. Also, the tests were performed at very conservative levels to avoid destroying the components.

5.2.1 Electrical Design Improvement

In future work the power usage can be improved. This can be done by experimenting with different microcontrollers, stepper motors, stepper motor drivers and changing gear ratios of the hardware design.

Table 2.1 shows that the sensor-less driver used over 30 mW less per motor and this indicates that the built-in Hall-sensors are very inefficient. The A4941 driver does commutate poorly at low speeds, but performed well around the 8000 RPM speed that the DGCMG operate. In case of gimbal failure the wheels must still be usable in reaction wheel mode at a low momentum bias and thus the LV8827LFQA was elected over the A4941 in the final design. When a sensor-less driver is used, a dedicated wheel encoder should be added to perform accurate motor speed control. Such an encoder may have lower power consumption than the built-in motor Hall sensors and be more accurate as well. This dedicated encoder can be added to the top of the flywheel casing, but will require additional volume. The driver electronics can also be mounted on the inner gimbal casings to reduce the size of the unit if the space around the gimbals permits such a change.

It is necessary to be able to recover after a full system reset during space flight. Currently the stepper motor steps are counted to obtain the gimbal angles. After a reset, this count is lost. The steppers also occasionally miss a step when the current in the coils are not high enough. For all these reasons, it is necessary to have an absolute rotation angle encoder for the gimbals that is accurate, has low power usage and is small in size. The size available is very limited around the gimbals. Consequently, large mechanical design changes would be necessary to fit the encoder and would thus not be a viable option. Another option would be to have an optical switch at a known gimbal angle and have the gimbals sweep after a reset until it encounters this switch. Another method could be to use a stepper driver that has stall detection using the back EMF to detect when the stepper motor has reached a mechanical stop. It is advisable to use mechanical stops to prevent the stepper motors from ever exceeding their maximum range as this will sever their wires from the delicate connection pads of the motors. To improve the missed steps problem, a constant current driver for the stepper motors should be tested. The MOSFET circuit shown in Figure 2.16 from Section 2.4, that is currently used to power the stepper motor drivers, is not the ideal solution for these missed steps. The stepper rates may be increased if missed steps can be avoided and this will greatly increase torque capabilities.

5.2.2 Slew Performance Improvement

Future improvement can also be made in the slew settling time. As previously mentioned, the CMG torque is very large, but the torque can only be applied for a very short duration before the gimbals reach their 25° angle limit. By using thin, silicon insulated, multi-core wires, instead of the current plastic insulated, multi-core, ribbon cables, the gimbals can be allowed to rotate at least ±45°. This will decrease the slew manoeuvre settling time for the pitch in Figure 4.7d from 44.6 s to 28.5 s as found with simulation. By increasing the angle limit further to ±60°, the settling time will decrease to 25 s.

The maximum torque capability of the CMGs can also be improved by increasing the nominal flywheel speed from 8000 RPM to 9000 RPM and increasing the flywheel radius with 1.2 mm. This will increase the torque capability from 0.52 mN m to 1 mN m with no overall size increase and by only slightly increasing the overall weight by 15 g and an approximate power increase of 45 mW.

5.2.3 Mechanical Structure Improvements

As previously mentioned in Section 2.3, the mass of the entire DGCMG can be reduced significantly by removing material from the frame. Detailed strength analysis should be done to determine the optimal mechanical design that will have minimum mass but still retain rigidity. This rigidity is vital in order to survive the immense forces experienced during launch. Finite Element Analysis software may be useful in this regard to study the strain in the frame with large forces applied.

Hardware improvements that will greatly improve the DGCMG system performance are shown in Appendix D.2.

Tests that could be done in the future, that were not performed during this thesis, are:

- Temperature tests to determine if the device can tolerate the large temperature fluctuations that occur when the spacecraft moves from eclipse into the sun exposed part of the orbit.
- Vacuum tests to determine if the device can survive in the low pressure environment of space.
- Vibration tests to determine if the mechanical design can survive the large forces involved during launch and still operate effectively.

During launch, the gimbals will rattle due to backlash in the gears and radial tolerances in the bearings. This may cause damage to gear teeth or the motors. Therefore, methods should also be analysed on securing the DGCMG during launch. A simple method could be to add a release rod that secures all the gimbals and frame together. Such a rod can be spring loaded to release the setup when a burn wire is activated. This method is risky as a failure might leave the entire device inoperable.

5.3 Summary

This thesis shows research performed on current attitude actuators and CMG technology for use in CubeSats and nano-satellites. It outlined the development and testing of a CMG configuration consisting of two scissoring DGCMGs. The scissoring of the outer gimbals was accomplished using gears and the inner gimbals were individually actuated. The development included electronic and hardware design as well as the implementation of attitude controllers for simulations and Hardware-in-the-Loop tests. The tests results satisfy the design specifications and support future development of the proposed design.

References

[1] C. Bernal and M. van Bolhuis, "Releasing the cloud: A deployment system design for the qb50 cubesat mission," *26th annual AIAA/USU*, Augustus 2012.

[2] D. Selva and D. Krejci, "A survey and assessment of the capabilities of cubesats for earth observation," *Acta Astronautica*, vol. 74, pp. 50–68, 2012.

[3] J. Champagne, S. Hansen, T. Newswander, and B. Crowther, "Cubesat image resolution capabilities with deployable optics and current imaging technology," *28th annual AIAA/USU*, 2014.

[4] M. E. Dearborn, G. P. Andersen, O. Asmolova, R. L. Balthazor, M. G. McHarg, H. C. Nelson, T. S. Quiller, G. R. Wilson, T. J. Harvey, and T. W. Murphey, "A deployable membrane telescope payload for cubesats," *Journal of Small Satellites*, vol. 3, pp. 253–264, March 2014.

[5] "CubeSpace website." `http://www.cubespace.co.za/`, 2015.

[6] J. Schoonwinkel, "Attitude determination and control system of a nanosatellite," Master's thesis, Stellenbosch: University of Stellenbosch, 2007.

[7] "Maryland Aerospace website." `http://maiaero.com/`, 2015.

[8] J. Auret, "Design of an aerodynamic attitude control system for a cubesat," Master's thesis, Stellenbosch: Stellenbosch University, 2012.

[9] J. Gerber, "A 3-axis attitude control system hardware design for a cubesat," Master's thesis, University of Stellenbosch, 2014.

[10] O. R. Stohlman, M. Schenk, and V. Lappas, "Development of the deorbitsail flight model," *National Harbor, Maryland*, 2014.

[11] A. Schoonwinkel, G. Milne, S. Mostert, W. Steyn, and K. van der Westhuizen, "Pre-flight performance of sunsat, south africa's first remote sensing and packet

communications microsatellite," *Proceedings of the Tenth Annual AIAA/USU Conference on Small Satellites*, September 1996.

[12] Y. Tsuda, O. Mori, R. Funase, H. Sawada, T. Yamamoto, T. Saiki, T. Endo, K. Yonekura, H. Hoshino, and J. Kawaguchi, "Achievement of ikarosâĂŤjapanese deep space solar sail demonstration mission," *Acta Astronautica*, vol. 82, no. 2, pp. 183–188, 2013.

[13] C. Biddy and T. Svitek, "Lightsail-1 solar sail design and qualification," in *Proceedings of the 41st Aerospace Mechanisms Symposium*, 2012.

[14] J. Mueller, R. Hofer, and J. Ziemer, "Survey of propulsion technologies applicable to cubesats," *NASA Technical Report*, 2010.

[15] E. Butikov, "Precession and nutation of a gyroscope," *European journal of physics*, vol. 27, no. 5, p. 1071, 2006.

[16] N. Townsend, A. Murphy, and R. Shenoi, "A new active gyrostabiliser system for ride control of marine vehicles," *Ocean engineering*, vol. 34, no. 11, pp. 1607–1617, 2007.

[17] S. R. Starin and J. Eterno, "Spacecraft attitude determination and control systems," in *Space Mission Engineering: The New SMAD* (J. R. Wertz, D. F. Everett, and J. J. Puschell, eds.), ch. 19.1.3, pp. 576–580, Hawthorne, CA: Microcosm Press, 2011.

[18] B. Wie, *Space Vehicle Dynamics and Control*, ch. 7 and 11. AIAA Education Series, Reston, Virginia: AIAA, second ed., 2008.

[19] R. Berner, "Control moment gyro actuator for small satellite applications," Master's thesis, Stellenbosch: University of Stellenbosch, 2005.

[20] "Honeybee Robotics website." `http://www.honeybeerobotics.com/`, 2015.

[21] V. Nagabhushan, "Development of control moment gyroscopes for attitude control of small satellites," Master's thesis, University of Florida, 2009.

[22] V. J. Lappas, W. H. Steyn, and C. I. Underwood, "Attitude control for small satellites using control moment gyros," *Acta Astronautica*, vol. 51, no. 1, pp. 101–111, 2002.

[23] W. H. Steyn, "A dual-wheel multi-mode spacecraft actuator for near-minimum-time large angle slew maneuvres," *Aerospace Science and Technology*, vol. 12, pp. 545–554, Jan. 2008.

[24] S. Zheng and B. Han, "Investigations of an integrated angular velocity measurement and attitude control system for spacecraft using magnetically suspended double-gimbal CMGs," *Advances in Space Research*, vol. 51, no. 12, pp. 2216–2228, 2013.

[25] "Faulhaber website." `http://www.faulhaber.com/`, 2015.

[26] R. Burt, "Distributed electrical power system in cubesat applications," Master's thesis, Utah State University, Logan, UT, 2011.

[27] Allegro MicroSystems, LCC, 115 Northeast Cutoff, Worcester, Massachusetts, USA, *A4915 Data Sheet*, April 2013. Rev. 1.

[28] P. J. Botma, "The design and development of an adcs obc for a cubesat," Master's thesis, Stellenbosch: Stellenbosch University, 2011.

[29] W. H. Steyn, "Near-minimum-time eigenaxis rotation maneuvers using reaction wheels," *Journal of Guidance, Control, and Dynamics*, vol. 18, no. 5, pp. 1184–1189, 1995.

[30] B. Wie, H. Weiss, and A. Arapostathis, "Quaternion feedback regulator for spacecraft eigenaxis rotations," *Journal of Guidance, Control, and Dynamics*, vol. 12, pp. 375–380, Mar. 1988.

[31] S. Chesi, O. Perez, and M. Romano, "A dynamic, hardware-in-the-loop, three-axis simulator of spacecraft attitude maneuvering with nanosatellite dimensions," *Journal of Small Satellites*, vol. 4, no. 1, pp. 315–328, 2015.

[32] G. Andersen, O. Asmolova, G. McHarg, M. Dearborn, and T. Quiller, "Falconsat-7: Towards rapidly deployable space-based surveillance," *Dept of Physics, Air Force Academy*, 2013.

Appendix A

Attitude Conversions

This appendix shows the relationship between the different attitude representations. The conversion to direction cosine matrix of all these representations will be shown and this will allow any conversion between representations to be performed via DCM.

A.1 Euler Angles

In order to convert Euler angles to a Direction Cosine Matrix, it is necessary to formulate a DCM for each axis rotation. A rotation ϕ about the X-axis or roll axis is given by the DCM:

$$\mathbf{C_X} = \begin{bmatrix} 1 & 0 & 0 \\ 0 & \cos(\phi) & \sin(\phi) \\ 0 & -\sin(\phi) & \cos(\phi) \end{bmatrix} \tag{A.1}$$

For an angle θ about the Y-axis or pitch axis the DCM is:

$$\mathbf{C_Y} = \begin{bmatrix} \cos(\theta) & 0 & -\sin(\theta) \\ 0 & 1 & 0 \\ \sin(\theta) & 0 & \cos(\theta) \end{bmatrix} \tag{A.2}$$

And finally, a rotation ψ about the Z-axis or yaw axis is given by the DCM:

$$\mathbf{C_Z} = \begin{bmatrix} \cos(\psi) & \sin(\psi) & 0 \\ -\sin(\psi) & \cos(\psi) & 0 \\ 0 & 0 & 1 \end{bmatrix} \tag{A.3}$$

These DCMs can be multiplied in the inverse order of the Euler sequence to form the final rotation matrix. That is, an Euler-123 rotation to DCM would become:

$$\mathbf{C_{123}} = \mathbf{C_Z C_Y C_X} = \tag{A.4}$$
$$\begin{bmatrix} \cos(\theta)\cos(\psi) & \cos(\phi)\sin(\psi) + \sin(\phi)\sin(\theta)\cos(\psi) & \sin(\phi)\sin(\psi) - \cos(\phi)\sin(\theta)\cos(\psi) \\ \cos(\theta)\sin(\psi) & \cos(\phi)\cos(\psi) - \sin(\phi)\sin(\theta)\sin(\psi) & \sin(\phi)\cos(\psi) + \cos(\phi)\sin(\theta)\sin(\psi) \\ \sin(\theta) & -\cos(\theta)\sin(\phi) & \cos(\theta)\cos(\phi) \end{bmatrix}$$

In the same way the other sequences can be converted to DCMs with $\mathbf{C_{312}} = \mathbf{C_Y C_X C_Z}$, $\mathbf{C_{321}} = \mathbf{C_X C_Y C_Z}$, $\mathbf{C_{132}} = \mathbf{C_Y C_Z C_X}$, etc. To inversely find the Euler angles from a DCM, the components can be used with trigonometric functions as follows:

$$\phi = \arctan 4\left(\frac{-C_{32}}{C_{33}}\right) \tag{A.5}$$
$$\theta = \arcsin\left(C_{31}\right) \tag{A.6}$$
$$\psi = \arctan 4\left(\frac{-C_{12}}{C_{11}}\right) \tag{A.7}$$

Note that the arctan is used in full quadrant fashion and that $\theta \in \{-\frac{\pi}{2}, \frac{\pi}{2}\}$ is required.

A.2 Axis-Angle

The Axis-Angle representation can be given by the unit vector $\mathbf{e}$, called the Euler axis or eigenaxis, and the angle θ.

In Figure A.1 the point $\mathbf{B}$ is the result after the point $\mathbf{A}$ is rotated around the Euler axis shown by the dotted line. The circle shows the plane perpendicular to the Euler axis on which the point is rotated. Basis vectors $\mathbf{x}'$ and $\mathbf{y}'$ can be defined on this plane to form a coordinate reference frame where $\mathbf{x}'$ is in the direction of the point $\mathbf{A}$ and $\mathbf{y}'$ is the 90° to $\mathbf{x}'$. The cross product can be used to find these vectors:

$$\mathbf{y}' = \mathbf{e} \times \mathbf{A} \tag{A.8}$$
$$\mathbf{x}' = \mathbf{y}' \times \mathbf{e} \tag{A.9}$$
$$\mathbf{x}' = \mathbf{e} \times \mathbf{A} \times \mathbf{e} \tag{A.10}$$

A rotation of the point $\mathbf{A}$ with the circle coordinate system as reference can then be defined as:

$$\mathbf{B} = \cos(\theta)\mathbf{x}' + \sin(\theta)\mathbf{y}' \tag{A.11}$$

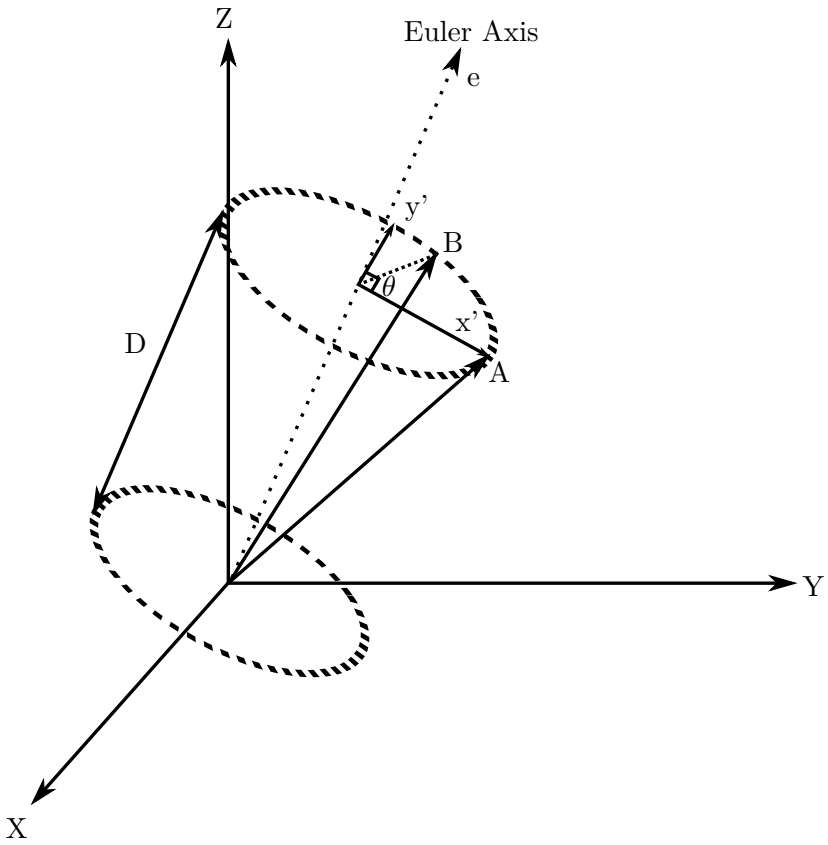

Figure A.1: Axis-Angle to DCM conversion.

In order to transform this equation to the proper reference frame, an offset must be added that is defined by the vector $\mathbf{D} = \mathbf{A} - \mathbf{x}'$. Equation A.11 now becomes:

$$\mathbf{B} = \mathbf{A} + (\cos(\theta) - 1)\,\mathbf{x}' + \sin(\theta)\mathbf{y}' \tag{A.12}$$
$$= \mathbf{A} + (\cos(\theta) - 1)\,(\mathbf{e} \times \mathbf{A} \times \mathbf{e}) + \sin(\theta)\,(\mathbf{e} \times \mathbf{A}) \tag{A.13}$$

To get this equation in matrix form, the skew symmetric matrix must be defined where:

$$\mathbf{y}' = \mathbf{e} \times \mathbf{A} \tag{A.14}$$
$$= \tilde{\mathbf{e}}\mathbf{A} \tag{A.15}$$

The cross product can be written out as:

$$y_1' = e_2A_3 - A_2e_3 \tag{A.16}$$
$$y_2' = e_3A_3 - A_3e_1 \tag{A.17}$$
$$y_3' = e_1A_3 - A_1e_2 \tag{A.18}$$

Therefore the skew symmetric matrix is:

$$\tilde{\mathbf{e}} = \begin{bmatrix} 0 & -e_3 & e_2 \\ e_3 & 0 & e_1 \\ -e_2 & e_1 & 0 \end{bmatrix} \tag{A.19}$$

Equation A.13 now becomes:

$$\mathbf{B} = \mathbf{A} + (\cos(\theta) - 1)\,(\tilde{\mathbf{e}}\mathbf{A} \times \mathbf{e}) + \sin(\theta)\,(\tilde{\mathbf{e}}\mathbf{A}) \tag{A.20}$$
$$= \mathbf{A} + (1 - \cos(\theta))\left(\tilde{\mathbf{e}}^2\mathbf{A}\right) + \sin(\theta)\,(\tilde{\mathbf{e}}\mathbf{A}) \tag{A.21}$$
$$= \left[\mathbf{I} + (1 - \cos(\theta))\,\tilde{\mathbf{e}}^2 + \sin(\theta)\tilde{\mathbf{e}}\right]\mathbf{A} \tag{A.22}$$

The direction cosine matrix $\mathbf{C}$ can now be defined as:

$$\mathbf{C} = \left[\mathbf{I} + (1 - \cos(\theta))\,\tilde{\mathbf{e}}^2 + sin(\theta)\tilde{\mathbf{e}}\right] = \tag{A.23}$$

$$\begin{bmatrix} 1 + (1 + (e_1^2 - 1)\cos(\theta)) & -e_3\sin(\theta) + e_1e_2(1 - \cos(\theta)) & e_2\sin(\theta) + e_1e_3(1 - \cos(\theta)) \\ e_3\sin(\theta) + e_1e_2(1 - \cos(\theta)) & 1 + (e_2^2 - 1)(1 - \cos(\theta)) & -e_1\sin(\theta) + e_2e_3(1 - \cos(\theta)) \\ -e_2\sin(\theta) + e_1e_3(1 - \cos(\theta)) & e_1\sin(\theta) + e_2e_3(1 - \cos(\theta)) & 1 + (e_3^2 - 1)(1 - \cos(\theta)) \end{bmatrix} \tag{A.24}$$

With this matrix available, the inverse conversion from DCM to Axis-Angle can be

performed as follows:

$$\theta = \arccos\left(\frac{C_{11} + C_{22} + C_{33} - 1}{2}\right) \tag{A.25}$$

$$e_1 = \frac{(C_{32} - C_{23})}{\sqrt{\left((C_{32} - C_{23})^2 + (C_{13} - C_{31})^2 + (C_{21} - C_{12})^2\right)}} \tag{A.26}$$

$$e_2 = \frac{(C_{13} - C_{31})}{\sqrt{\left((C_{32} - C_{23})^2 + (C_{13} - C_{31})^2 + (C_{21} - C_{12})^2\right)}} \tag{A.27}$$

$$e_3 = \frac{(C_{21} - C_{12})}{\sqrt{\left((C_{32} - C_{23})^2 + (C_{13} - C_{31})^2 + (C_{21} - C_{12})^2\right)}} \tag{A.28}$$

This conversion is only possible when the angle is not equal to $0°$ or $180°$.

A.3 Quaternion

We have defined quaternions as a special representation of the Axis-Angle and the conversion is given by:

$$q_1 = e_1 \sin\left(\frac{\theta}{2}\right)$$
$$q_2 = e_2 \sin\left(\frac{\theta}{2}\right)$$
$$q_3 = e_3 \sin\left(\frac{\theta}{2}\right)$$
$$q_4 = \cos\left(\frac{\theta}{2}\right)$$

where,

$$q_1^2 + q_2^2 + q_3^2 + q_4^2 = 1$$

With (A.24) the conversion of a quaternion to DCM can be given by:

$$\mathbf{C} = \begin{bmatrix} q_1^2 - q_2^2 - q_3^2 + q_4^2 & 2(q_1q_2 + q_3q_4) & 2(q_1q_3 - q_2q_4) \\ 2(q_1q_2 - q_3q_4) & -q_1^2 + q_2^2 - q_3^2 + q_4^2 & 2(q_2q_3 + q_1q_4) \\ 2(q_1q_3 + q_2q_4) & 2(q_2q_3 - q_1q_4) & -q_1^2 - q_2^2 + q_3^2 + q_4^2 \end{bmatrix} \tag{A.29}$$

To perform the inverse conversion, the quaternions can be found with:

$$q_4 = \frac{1}{2}\sqrt{C_{11} + C_{22} + C_{33} + 1} \tag{A.30}$$

$$q_1 = \frac{1}{4q_4}(C_{23} - C_{32}) \tag{A.31}$$

$$q_2 = \frac{1}{4q_4}(C_{31} - C_{13}) \tag{A.32}$$

$$q_3 = \frac{1}{4q_4}(C_{12} - C_{21}) \tag{A.33}$$

In some cases the result will be inaccurate if the result for q_4 is very small or zero. For such cases it would be wise to first calculate the quaternion element whose index corresponds to the index of the largest value on the DCM diagonal.

Appendix B

SPI Communication

The Serial Peripheral Interface (SPI) is a communications bus used by the microcontroller to communicate with sensors, memory or other controllers. This interface uses synchronous communication and can provide very high speed that is determined by a selectable clock divider. With synchronous communication, the clock is connected between devices and data is sent or received on the rising or falling clock edges. In hardware this can be achieved using a simple shift register and is much cheaper than a UART. The lines connected between the devices consist of a clock signal named SCK or CLK, MOSI (Master Output Slave Input) and MISO (Master Input Slave Output) for data transfer. There is also a slave select (SS) line that alerts the peripheral device before communication starts. SPI operate with a master and slave structure where the microcontroller usually represents the master and the peripheral device the slave. The master drives the SS line, sends data with the MOSI line and receives data with the MISO line. For the peripheral device this is inverted. Multiple slaves can be connected to the SPI bus, but there can only be one master.

Some devices read the data on the MOSI line when a rising edge is detected on the clock line and then sets new bit on the MISO line when the falling edge is reached and other slave devices does this on the opposite edges. This is referred to as the clock phase. It is therefore important to consult the datasheet of the device and set the microcontroller on the same data mode. When setting up communication with a peripheral device it is first required to set the master SCK rate to nearly the maximum which the peripheral can handle. Next, the order of the bits sent and received must be indicated as either Most Significant Bit (MSB) or Least Significant Bit (LSB) first. The SCK line can be either high or low during idle mode and is referred to as the clock polarity. The clock polarity and phase defines four modes that a peripheral device may belong to. These modes are shown in Table B.1 and must be set in the master. When

communicating with multiple slave devices, the mode can be changed accordingly.

Table B.1: SPI Modes of Operation.

SPI Mode	**Clock Polarity**	**Clock Phase**
0	0	0
1	0	1
2	1	0
3	1	1

For the ADIS16375 the SPI settings according to the datasheet is as follows:

- Maximum clock rate: SCK$\leq$15 MHz
- SPI Mode 3: Polarity=1, Phase=1
- MSB-First

Appendix C

Datasheets

CubeWheel

UNIVERSITEIT STELLENBOSCH UNIVERSITY

ESL Electronic Systems Laboratory

Feature List

- Can be used to exchange momentum with satellite body.
- Compatible with CubeSat and Nanosatellite applications
- Angular feedback obtainable through shielded magnetic encoder
- Brushless DC motor with vacuum rated bearings

Specifications

Large Wheel:		
Speed Range	±8000	rpm
Speed control accuracy (over full range)	< 5	rpm
Max Torque	2.1	mNm
Momentum Storage (@ 8000 rpm)	40	mNms
Peak Power (@ maximum acceleration)	1.8	W
Average Power (@ 2000 rpm)	150	mW
Dimension	55 Ø x 30	mm
Total Mass	162	g
Small Wheel:		
Speed Range	±8000	rpm
Speed control accuracy (over full range)	< 5	rpm
Max Torque	0.23	mNm
Momentum Storage (@ 8000 rpm)	1.7	mNms
Peak Power (@ maximum acceleration)	0.51	W
Average Power (@ 2000 rpm)	50	mW
Dimension	28 Ø x 22.7	mm
Total Mass	45	g

Contact Details

Electronic Systems Laboratory
Engineering Faculty
University of Stellenbosch
Private Bag X1 Matieland 7602
South Africa

T: +27-21-808-4926
F: +27-21-808-4981

E: whsteyn@sun.ac.za
http://www.esl.sun.ac.za/

Maryland Aerospace

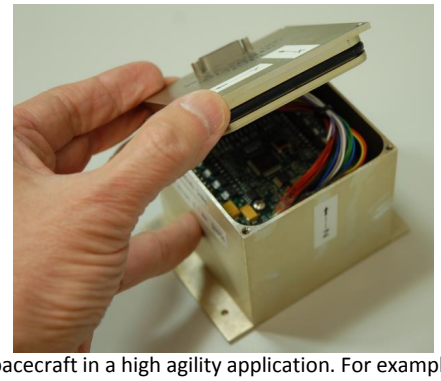

MAI-201

Miniature 3-AxisReaction Wheel

The MAI-201 is a 3 axis Miniature Reaction Wheel (MRW) in a hermetically sealed 3.2" x 3.2" x 2.725" enclosure. It is suitable for up to about 40lbs Nanosatellite applications requiring precise 3-axis pointing such as is required for Earth imaging or celestial pointing.

Torque and momentum storage have been sized for a micro spacecraft in a high agility application. For example, the MAI-201 can slew a 20 kg Earth imaging spacecraft to rapidly retarget between successive aim points, each located ± 30° off track.

The MAI-201 has been newly redesigned to accommodate precision dynamic balancing of the rotors down to less than 1mg-mm, enabling science missions requiring very low jitter such as observation of extra solar planets.

Specifications

Performance Item	Unit	Specification
ADACS		No
Dimensions	in	3.2 x 3.2 x 3.725
Mass	g	640
Momentum Storage@10000rpm	mNms	9.37
Max Torque	mNm	0.635
Operating Voltage	V	12
Power Consumption		
Idle	W	1.56 (0.13 @ 12V)
Steady State/Typical	W	4.98 (0.42A @ 12V)
Peak	W	12.9 (1.07A @ 12V)
Command/TLM Interface		RS232
Operating Temperature	deg C	-40 to 80
Launch Environment Vibration Spec	g rms	10

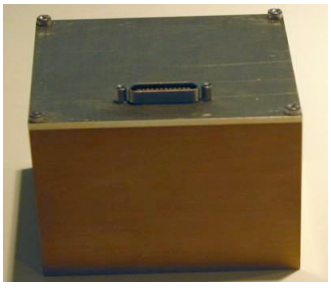

[w]: www.maiaero.com
[e]: discover@maiaero.com
[p]: 410-451-2505

UNIVERSITEIT STELLENBOSCH UNIVERSITY

CubeTorquer

ESL Electronic Systems Laboratory

Application

- Can be used to interact with the magnetic field of the earth to actively control satellite orientation.
- Compatable with CubeSat and Nanosatellite applications

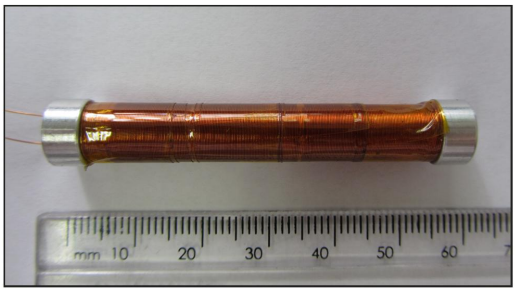

Specifications

Functional Characteristics:

Nominal magnetic moment	±0.2	Am^2
Linearity (Within ±0.4Am^2 range)	2.5	%
Residual moment	<0.48	mAm^2
Power	209	mW @ 2.5V
Resistance	30 – 31	Ω
Inductance	0.585	H
Magnetic gain constant (Within linear region)	2.9024	Am^2/A

Physical Characteristics:

Length	60	mm
Rod core diameter	5	mm
Rod core material	Supra 50	
Overall diameter	10	mm
Mass	22 ± 0.25	g

Contact Details

Electronic Systems Laboratory
Engineering Faculty
University of Stellenbosch
Private Bag X1 Matieland 7602
South Africa

T: +27-21-808-4926
F: +27-21-808-4981

E: whsteyn@sun.ac.za
http://www.esl.sun.ac.za/

HONEYBEE ROBOTICS
Spacecraft Mechanisms Corporation

Microsat CMG Attitude Control Array

Specification	Data
Mass	
Single CMG	600g
Control Electronics (for 4 CMGs)	700g
Size	
Single CMG	48 x 48 x 91 mm
Control Electronics*	215 x 115 x 25 mm
Box 90 Array (w/ electronics)*	230 x 125 x 82 mm
Power	
Single CMG, steady state	1.5 W
Single CMG, peak torque	2.0 W
Box 90 Array, steady state	8 W
Box 90 Array, Peak	10 W
CMG Momentum	
Rated Power, per CMG	56 mNm-s
Enhanced, per CMG	86 mNm-s
Box 90 Momentum Envelope (ellipsoid)	112 x 112 x 224 mNm-s
CMG Torque	
Rated Power	112 mNm
Enhanced	172 mNm
Wheel Rate	8,000 rpm (nominal) 12,000 rpm (max)
Radiation	
CMG	100krad
Control Electronics	10krad (100krad in dev.)
Interface	RS232 or RS422 Torque Triple Command or individual CMG rate commands
Operating Temperature Range	-20 to +85° C
* CubeSat-Compatible Option Available	

Description

Honeybee Robotics' **Microsat Control Moment Gyroscope** modules provide small spacecraft with unprecedented agility and pointing capabilities. They offer an order of magnitude superior performance over reaction wheels, at a fraction of the power.

Our Microsat CMG modules can be packaged together as a unit in any configuration, or they can be distributed to offer packaging flexibility. The scissored pair arrangement is designed to provide a seamless replacement for traditional reaction wheels.

Our integrated steering law controller can host a standard Box-90 pseudo-inverse steering law, or support a user-defined steering law.

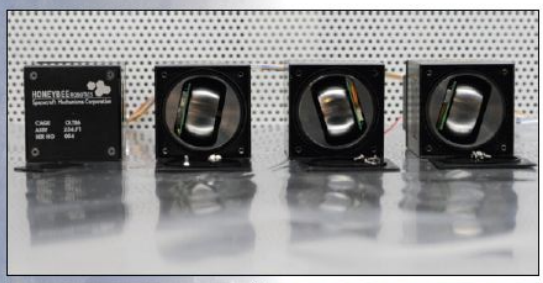

Contact

Honeybee is ISO9001:2000 and AS9100C certified.

Honeybee Robotics
Spacecraft Mechanisms Corporation

Erik Mumm
VP & Director of Flight Systems
Mumm@HoneybeeRobotics.com
(720) 340-4491

www.HoneybeeRobotics.com

FAULHABER

Stepper Motors 0,65 mNm

Two phase, 20 steps per revolution
PRECIstep® Technology

AM0820-ww-ee

	ww =		V-3-18		V-5-56		A-0,225-7		
			Voltage	Current	Voltage	Current	Voltage	Current	Drive mode
1	Nominal voltage		3	–	5	–	2	–	V DC
2	Nominal current per phase (both phases ON)		–	0,15	–	0,08	–	0,225	A
3	Phase resistance (at 20°C)		18		56		7,3		Ω
4	Phase inductance (1kHz)		3,9		12,6		1,4		mH
5	Back-EMF amplitude		1,3		2,4		0,8		V/k step/s
6	Holding torque [1] (at nominal current in both phases)	0,65							mNm
7	Holding torque [1] (at twice the nominal current)	1							mNm
8	Step angle (full step)	18							degree
9	Angular accuracy [2]	± 10							% of full step
10	Residual torque	0,06							mNm
11	Rotor inertia	2,75							$\cdot 10^{-9}$ kgm^2
12	Resonance frequency (at no load)	170							Hz
13	Electrical time constant	0,21							ms
14	Ambient temperature range	–30 ... +70							°C
15	Winding temperature tolerated, max.	130							°C
16	Thermal resistance winding-ambient air	76							°C/W
17	Thermal time constant	180							s
18	Shaft bearings	sintered bronze sleeves (standard)			ball bearings, preloaded (optional)				
19	Shaft load, max.:								
	– radial (3 mm from bearing)	0,3			3,0				N
	– axial	0,2			1,5				N
20	Shaft play, max.:								
	– radial (0,2N)	15			12				µm
	– axial (0,2N)	140			~0				µm
21	Isolation test voltage	200							V DC
22	Weight	3,3							g

[1] with bipolar driver
[2] 2 phases ON, balanced phase currents
[3] Curves measured with a load inertia of 10 $\cdot 10^{-9}$ kgm^2
[4] Testing the motor at lower supply voltages in current mode will result in a decrease in torque at higher speed, even with the same current setting

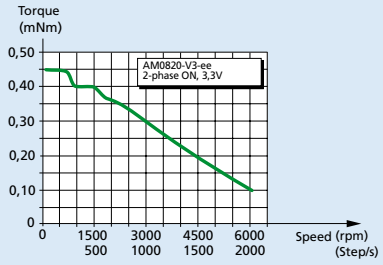

Voltage mode (V) [3]
Driver AD VL M1S

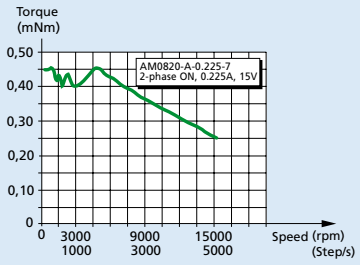

Current mode (A) [3] [4]
Driver AD CM M1S

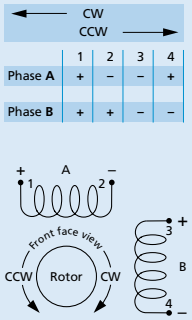

For notes on technical data and lifetime performance refer to "Technical Information".
Edition 2011 – 2012

FAULHABER

Dimensional drawing

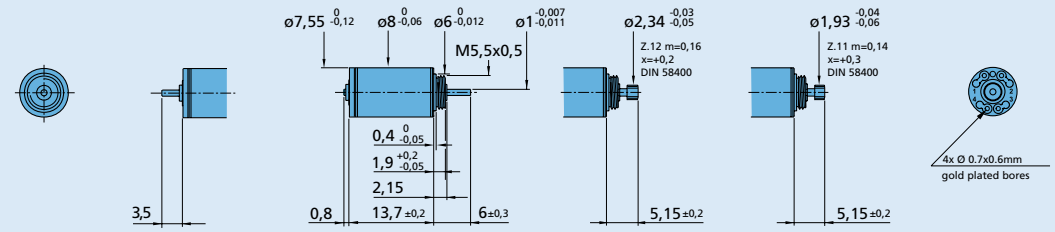

Front face view — Rear shaft

AM0820

Front shaft — for Gearhead 08/1 — for Gearheads 08/2, 08/3

Combinations

Drive Electronics	Encoders	Stepper Motors	Gearheads / Lead screws
AD VL M_S		**AM0820**	**08/1**
AD CM M_S			**08/2**
			08/3*
			10/1
			Lead screws M1,2 - M1,6
			Lead screws M2 - M2,5 - M3

* Zero Backlash Gearheads

Ordering information

Example: **AM0820-2R-V-3-18-08**

Motor type AM = Motor design 08 = Motor diameter (mm) 20 = Steps per revolution	**Bearings** (rr) Special lubricant options available	**Winding** (ww)	**Motor execution** (ee) Only front output shaft	With double output shaft	Front output shaft
AM0820	**-** (sleeve bearings)	**-V-3-18**	**-01**	**-00**	Plain shaft
	-2R (2 ball bearings)	**-V-5-56**	**-08**	**-09**	Pinion 08/1
		-A-0,225-7	**-10**	**-11**	Pinion 10/1
			-12	**-13**	Pinion 08/2, 08/3
			-21	**-20**	Shaft for lead screw M1,2
			-23	**-22**	Shaft for lead screw M2 - M2,5 - M3
			-25	**-24**	Shaft for lead screw M1,6

For notes on technical data and lifetime performance refer to "Technical Information".
Edition 2011 – 2012

FAULHABER

Planetary Gearheads 60 mNm

For combination with
DC-Micromotors
Stepper Motors

Series 08/1

	08/1	08/1K
Housing material	metal	metal
Geartrain material	steel	steel
Recommended max. input speed for:		
– continuous operation	8 000 rpm	8 000 rpm
Backlash, at no-load	≤ 3 °	≤ 3 °
Bearings on output shaft	sintered bearings	ball bearings
Shaft load, max.:		
– radial (4,5 mm from mounting face)	≤ 0,8 N	≤ 5 N
– axial	≤ 1 N	≤ 3 N
Shaft press fit force, max.	≤ 5 N	≤ 5 N
Shaft play		
– radial (4,5 mm from mounting face)	≤ 0,04 mm	≤ 0,06 mm
– axial	≤ 0,1 mm	≤ 0,05 mm
Operating temperature range	- 30 ... + 100 °C	- 30 ... + 100 °C

Specifications							
Number of gear stages		**1**	**2**	**3**	**4**	**5**	**6**
Continuous torque	mNm	60	60	60	60	60	60
Intermittent torque	mNm	120	120	120	120	120	120
Weight without motor, ca.	g	2,9	3,8	4,6	5,4	6,3	7,1
Efficiency, max.	%	90	80	70	60	55	48
Direction of rotation, drive to output		=	=	=	=	=	=
Reduction ratio (exact)		**4:1**	**16:1**	**64:1**	**256:1**	**1 024:1**	**4 096:1**
L2 [mm] = length without motor		9,6	12,3	15,0	17,7	20,4	23,1
L1 [mm] = length with motor	0816P...S	25,6	28,3	31,0	33,7	36,4	39,1
	AM0820...-08	23,4	26,1	28,8	31,5	34,2	36,9

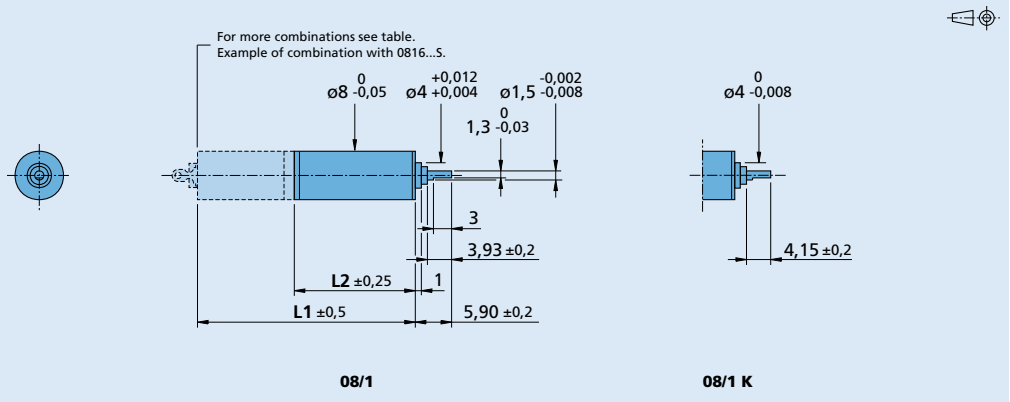

08/1 **08/1 K**

For notes on technical data and lifetime performance refer to "Technical Information".
Edition 2012 – 2013

FAULHABER

Brushless Flat DC-Micromotors 0,6 mNm

For combination with
Drive Electronics:
Speed Controller

Series 1509 ... B

			1509 T		006 B	012 B	
1	Nominal voltage	U_N			6	12	Volt
2	Terminal resistance, phase-phase	R			22,0	92,8	Ω
3	Output power [1]	$P_{2\ max.}$			0,31	0,30	W
4	Efficiency	$\eta_{max.}$			56	55	%
5	No-load speed	n_o			14 700	14 700	rpm
6	No-load current	I_o			0,0174	0,0087	A
7	Stall torque	M_H			0,97	0,92	mNm
8	Friction torque, static	C_o			0,025	0,025	mNm
9	Friction torque, dynamic	C_v			$2{,}6 \cdot 10^{-6}$	$2{,}6 \cdot 10^{-6}$	mNm/rpm
10	Speed constant	k_n			2 623	1 312	rpm/V
11	Back-EMF constant	k_E			0,381	0,762	mV/rpm
12	Torque constant	k_M			3,64	7,28	mNm/A
13	Current constant	k_I			0,275	0,137	A/mNm
14	Slope of n-M curve	$\Delta n/\Delta M$			15 856	16 721	rpm/mNm
15	Terminal inductance, phase-phase	L			590	2 350	µH
16	Mechanical time constant	τ_m			115	121	ms
17	Rotor inertia	J			0,69	0,69	gcm²
18	Angular acceleration	$\alpha_{max.}$			14	13	$\cdot 10^3$rad/s²
19	Thermal resistance	$R_{th\,1}$ / $R_{th\,2}$	65 / 45				K/W
20	Thermal time constant	τ_{w1} / τ_{w2}	10 / 130				s
21	Operating temperature range		-25 ... +80				°C
22	Shaft bearings		ball bearing, preloaded				
23	Shaft load max.:						
	– radial at 3 000/16 000 rpm (3 mm from mounting flange)		2,0 / 0,5				N
	– axial at 3 000/16 000 rpm (push-on only)		2,0 / 1,7				N
	– axial at standstill (push-on only)		15				N
24	Shaft play:						
	– radial	≤	0,015				mm
	– axial	=	0				mm
25	Housing material		plastic				
26	Weight		6,9				g
27	Direction of rotation		electronically reversible				
28	Number of pole pairs		2				
Recommended values - mathematically independent of each other							
29	Speed up to	$n_{e\ max.}$			16 000	16 000	rpm
30	Torque up to [1] [2]	$M_{e\ max.}$			0,52 / 0,60	0,51 / 0,58	mNm
31	Current up to [1] [2]	$I_{e\ max.}$			0,17 / 0,20	0,09 / 0,10	A

[1] at 5 000 rpm
[2] thermal resistance $R_{th\,2}$ not reduced / thermal resistance $R_{th\,2}$ by 55% reduced

Note:

The diagram indicates the recommended speed in relation to the available torque at the output shaft for a given ambient temperature of 22°C.

The diagram shows the motor in a completely insulated as well as thermally coupled condition ($R_{th\,2}$ 55% reduced).

The nominal voltage curve shows the operating point at nominal voltage in the insulated and thermally coupled condition. Any points of operation above the curve at nominal voltage will require a higher operating voltage. Any points below the nominal voltage curve will require less voltage.

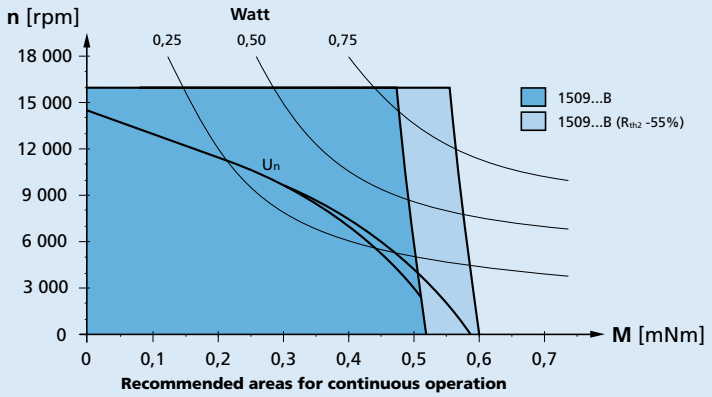

For notes on technical data and lifetime performance refer to "Technical Information".
Edition 2014

FAULHABER

1509 T ... B

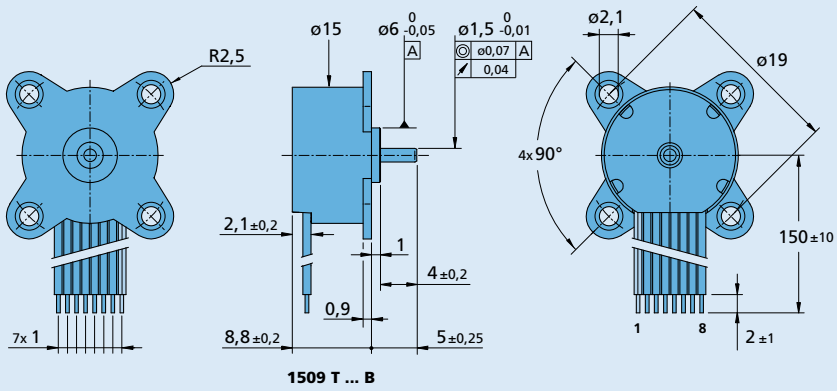

1509 T ... B

Cable
Jacket Material: PVC
8 conductors, AWG 28
grid 1,0 mm
wires tinned

Note:
Hallsensors digital

Connection

No.	Function
1	Phase C
2	Phase B
3	Phase A
4	GND
5	+ 5V
6	Hall sensor C
7	Hall sensor B
8	Hall sensor A

For notes on technical data and lifetime performance refer to "Technical Information".
Edition 2014

Appendix D

Mechanical Schematics

D.1 Current Design

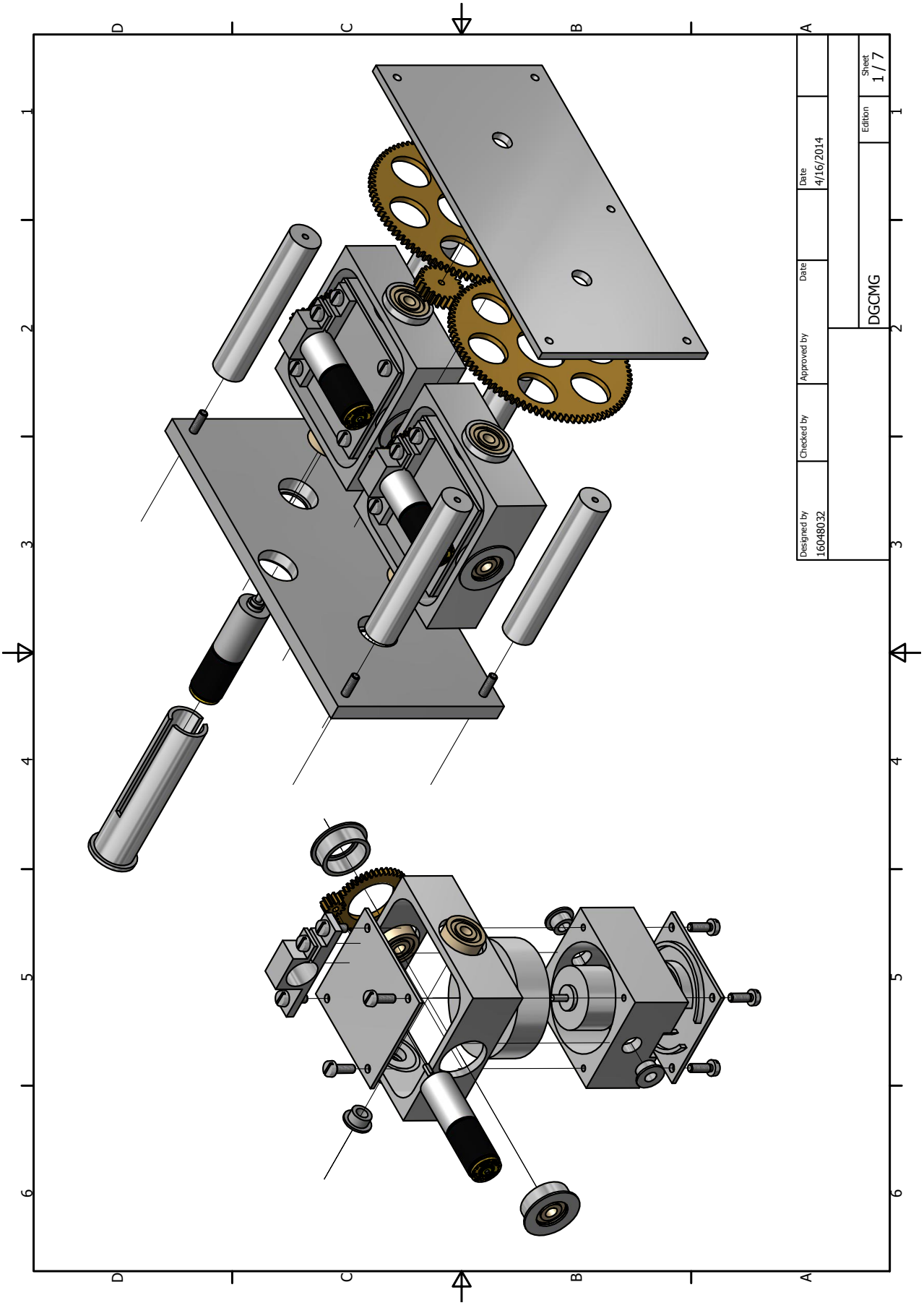

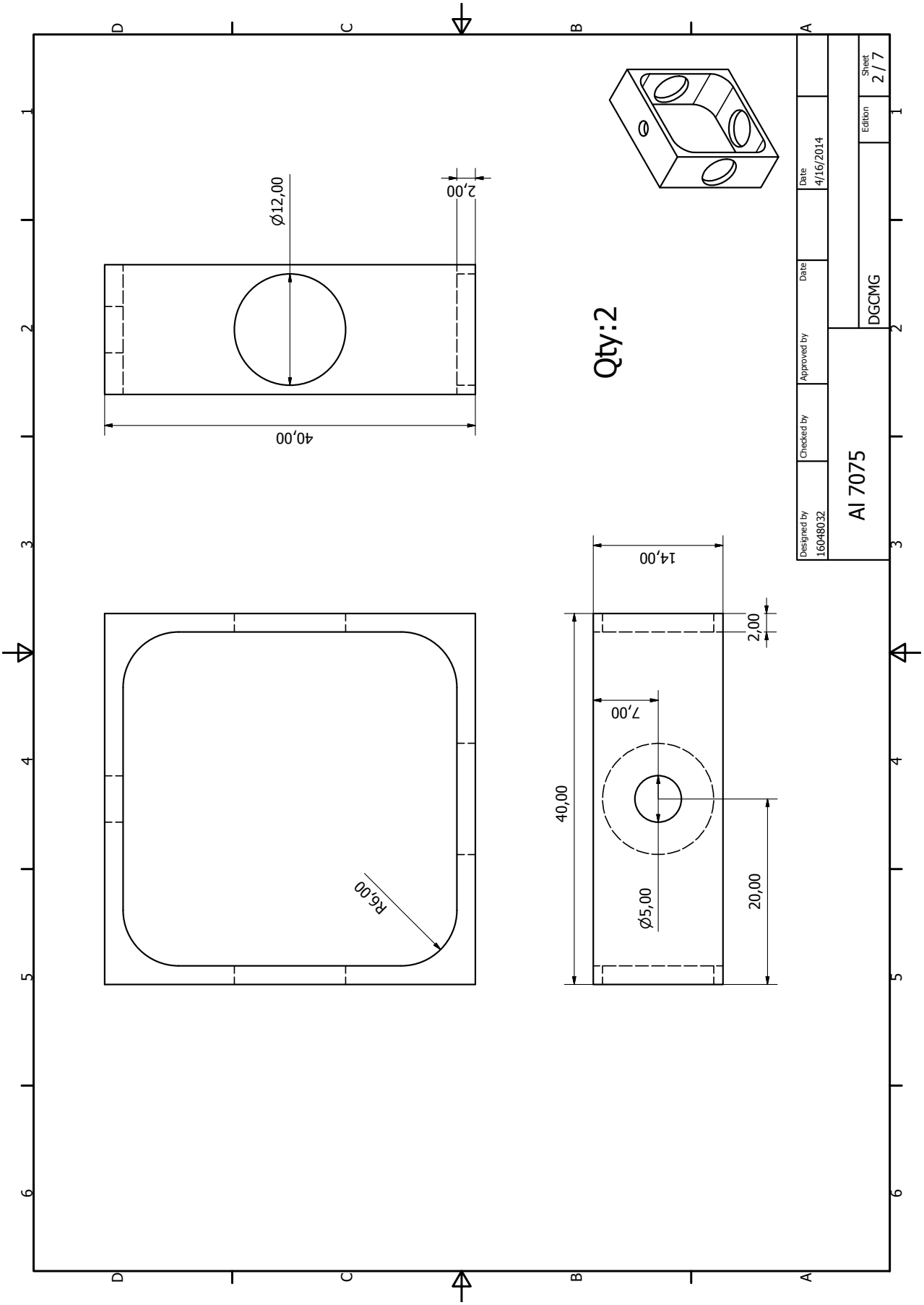

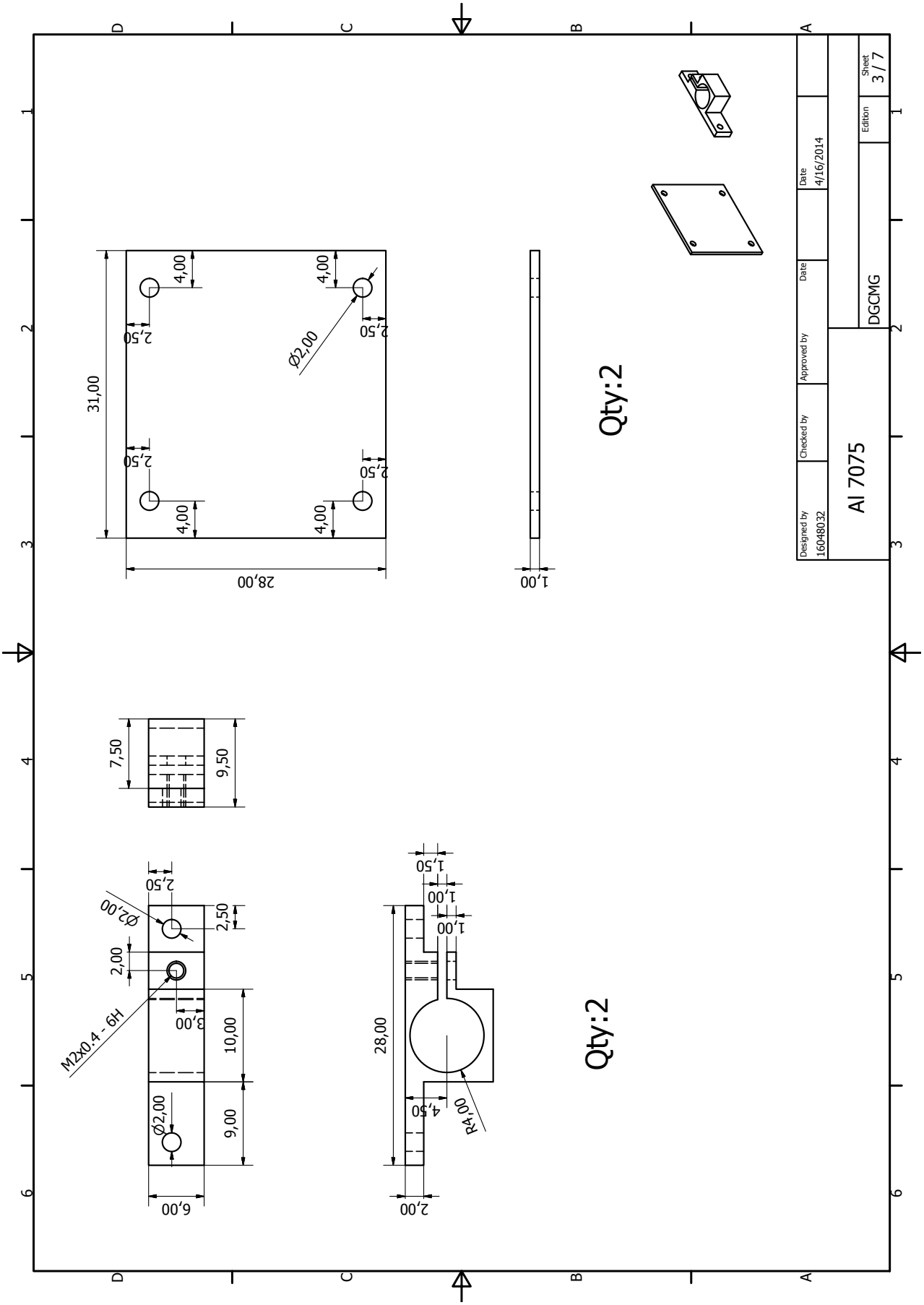

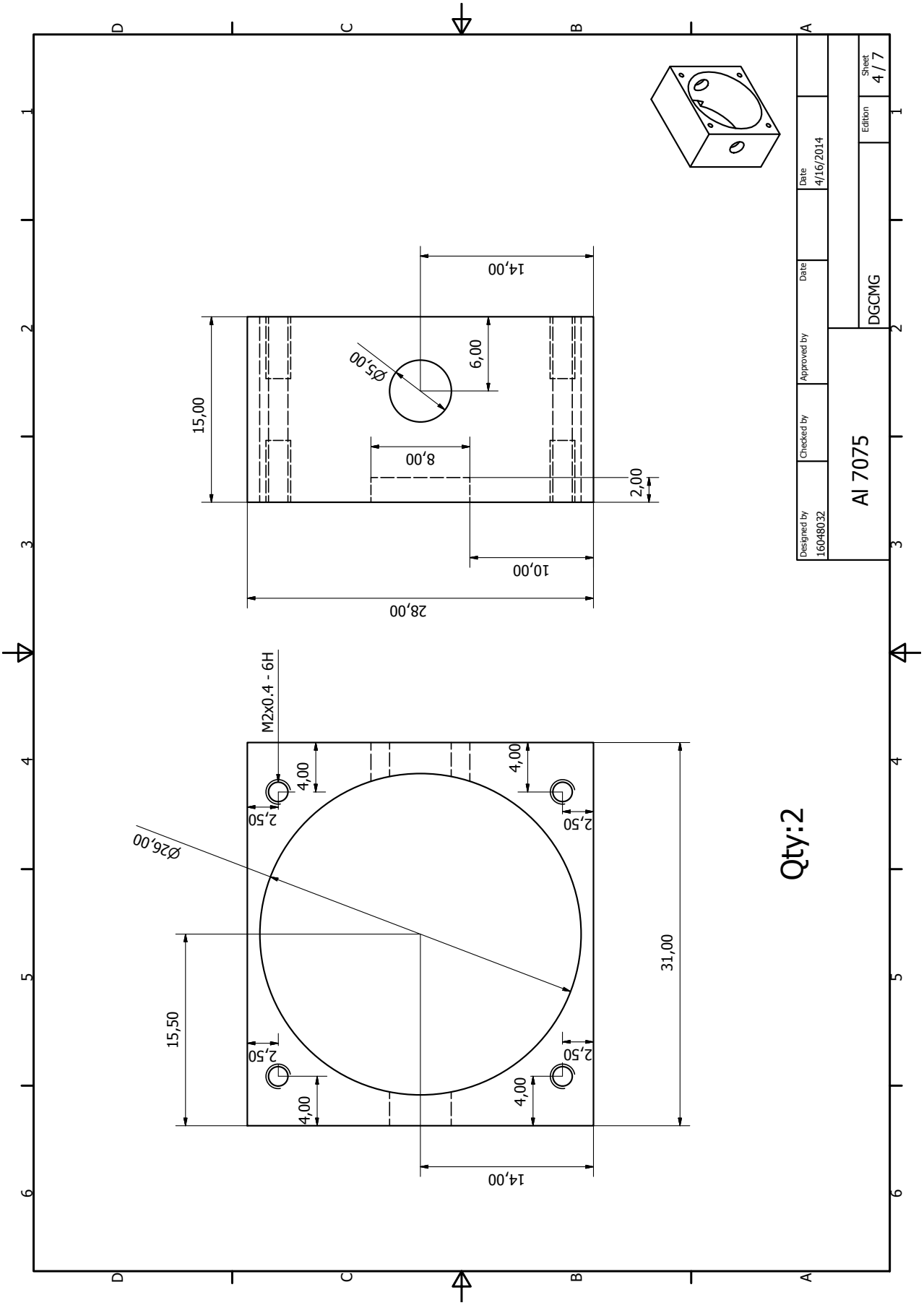

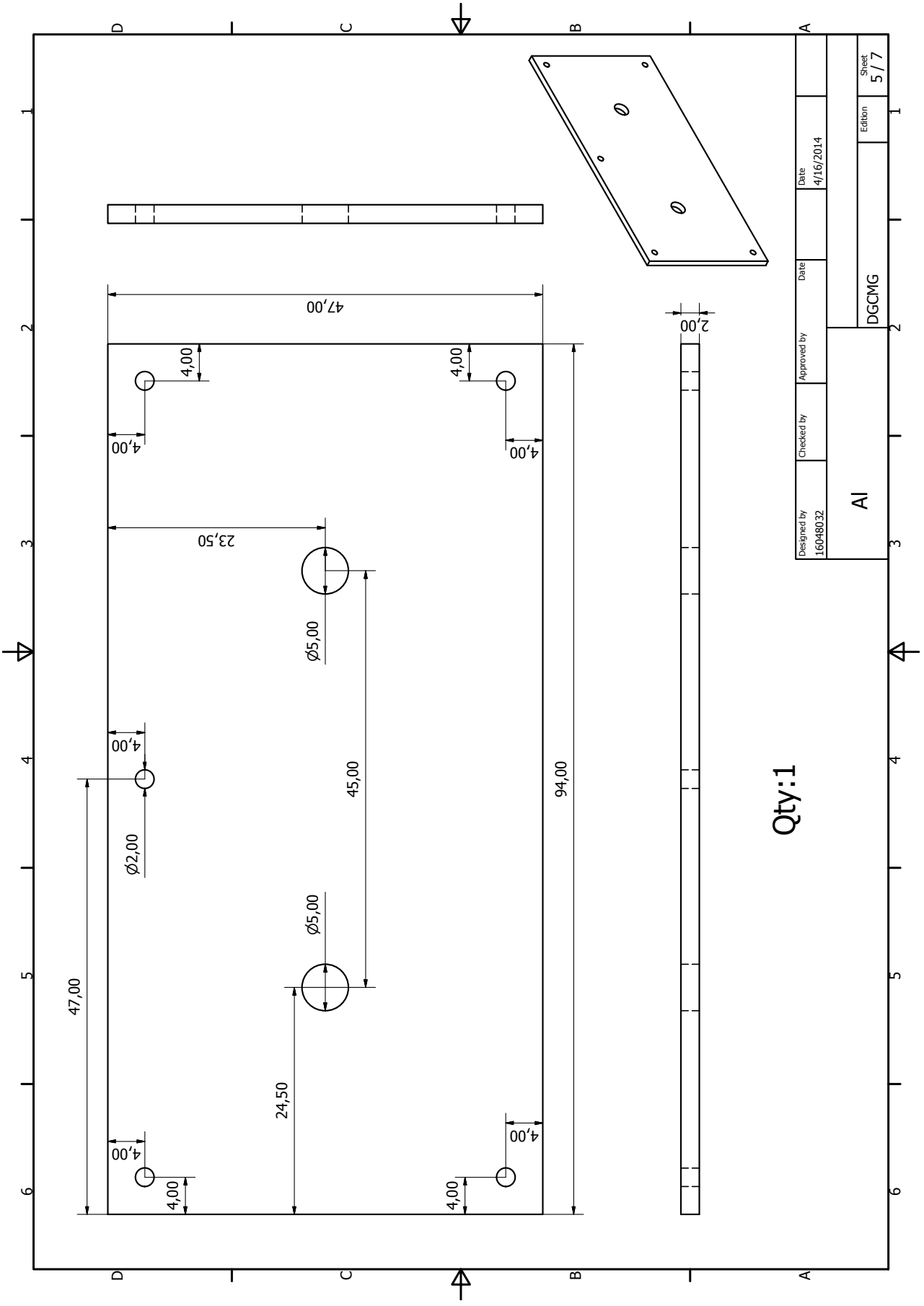

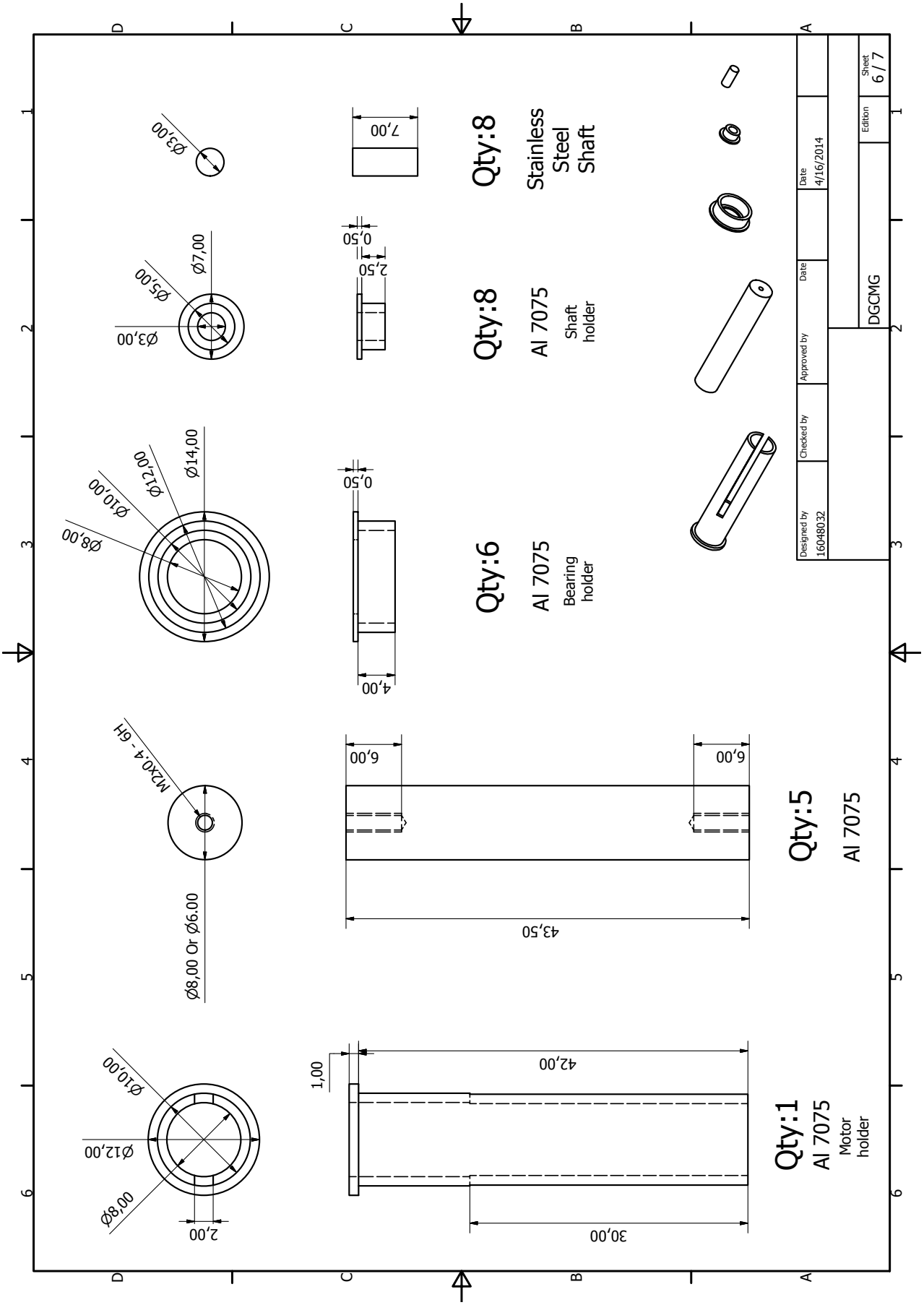

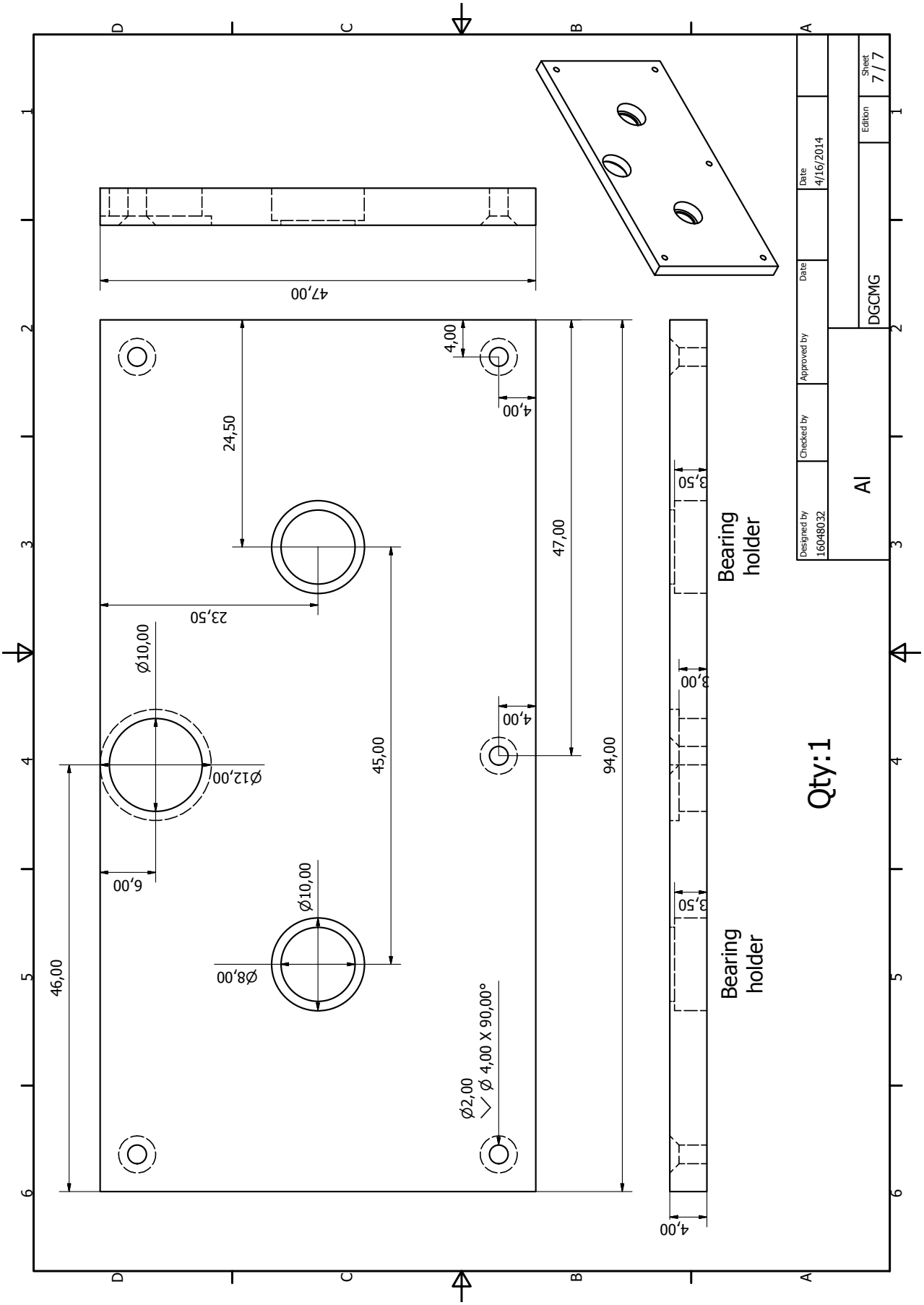

D.2 Improved Design

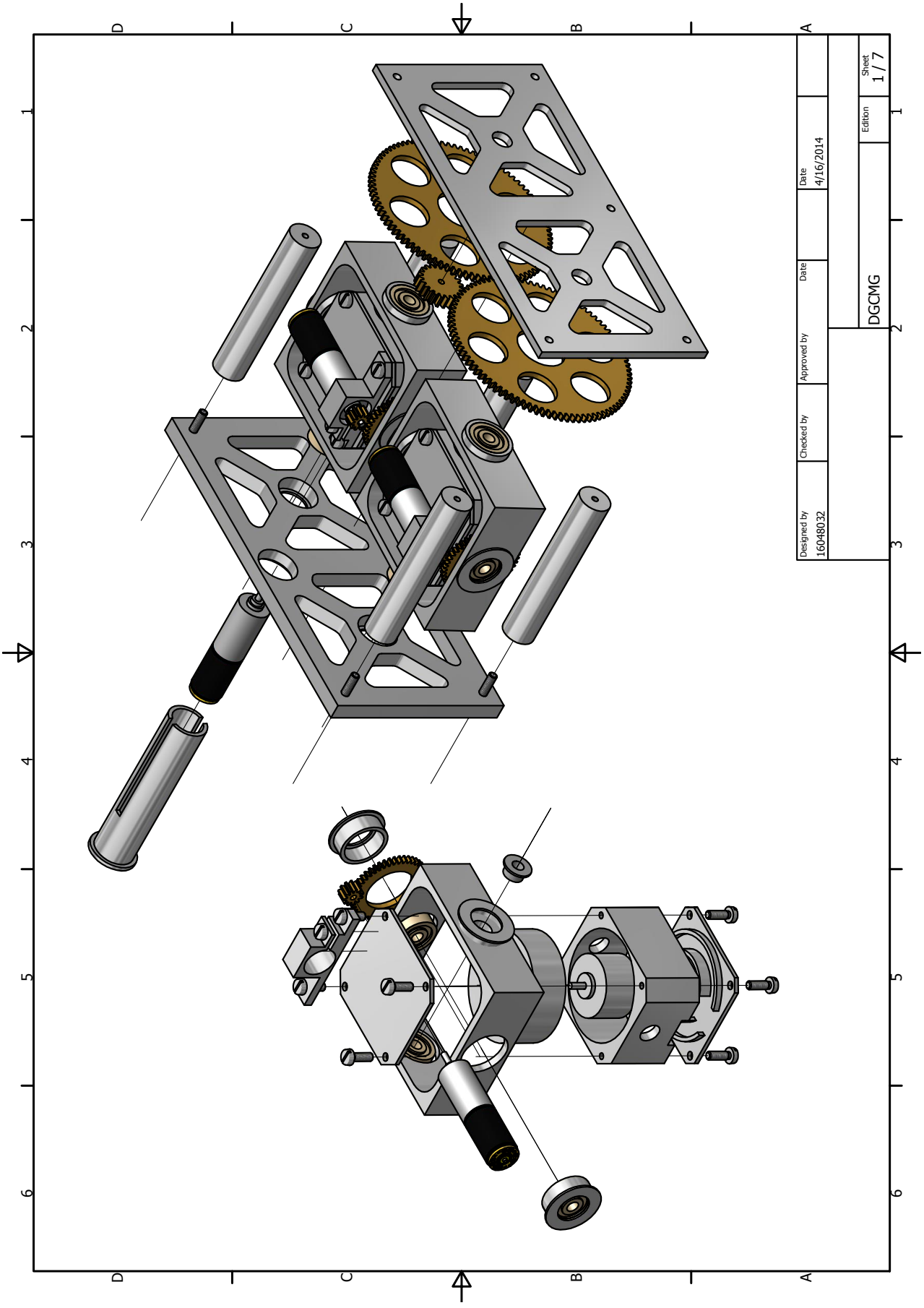

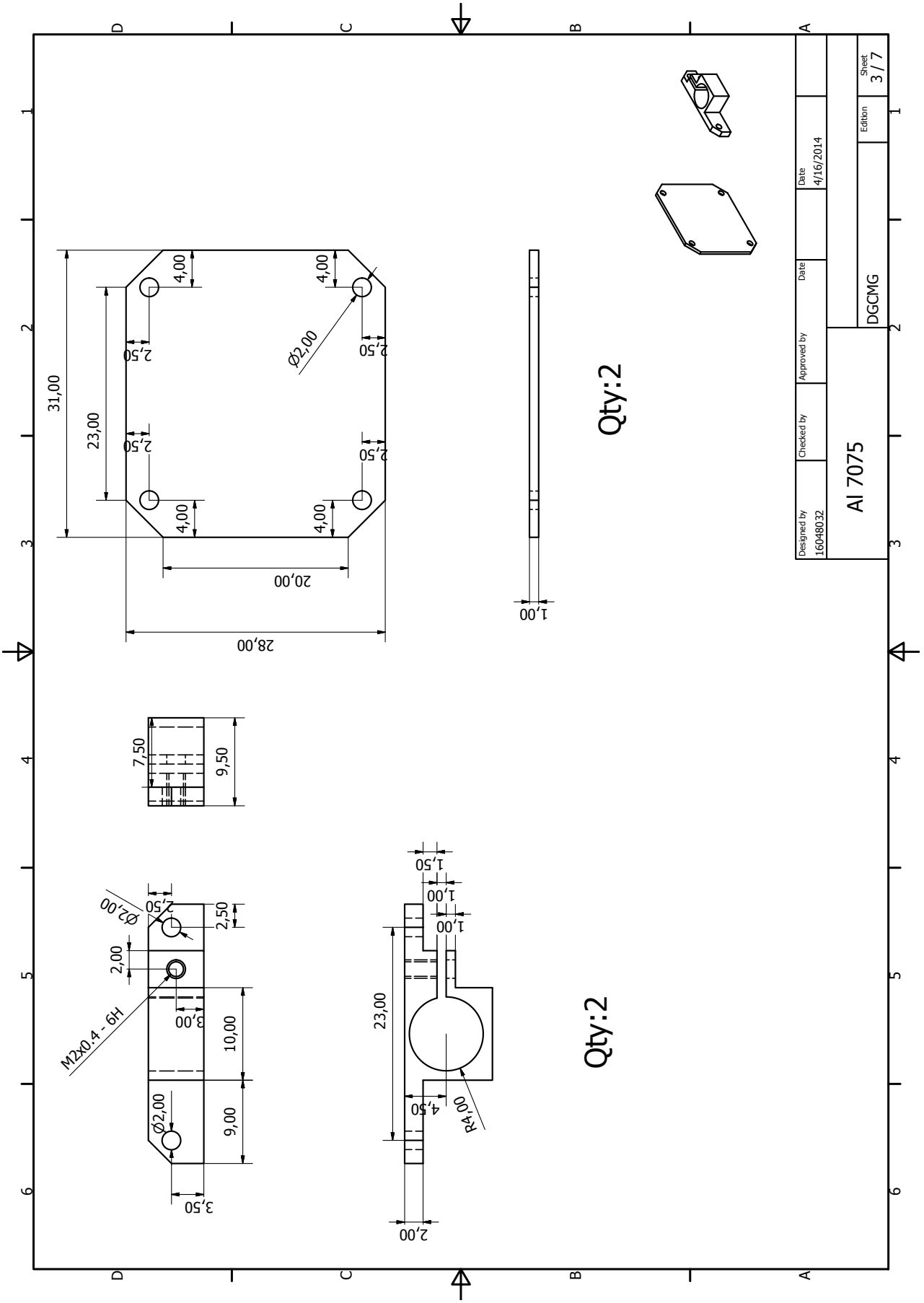

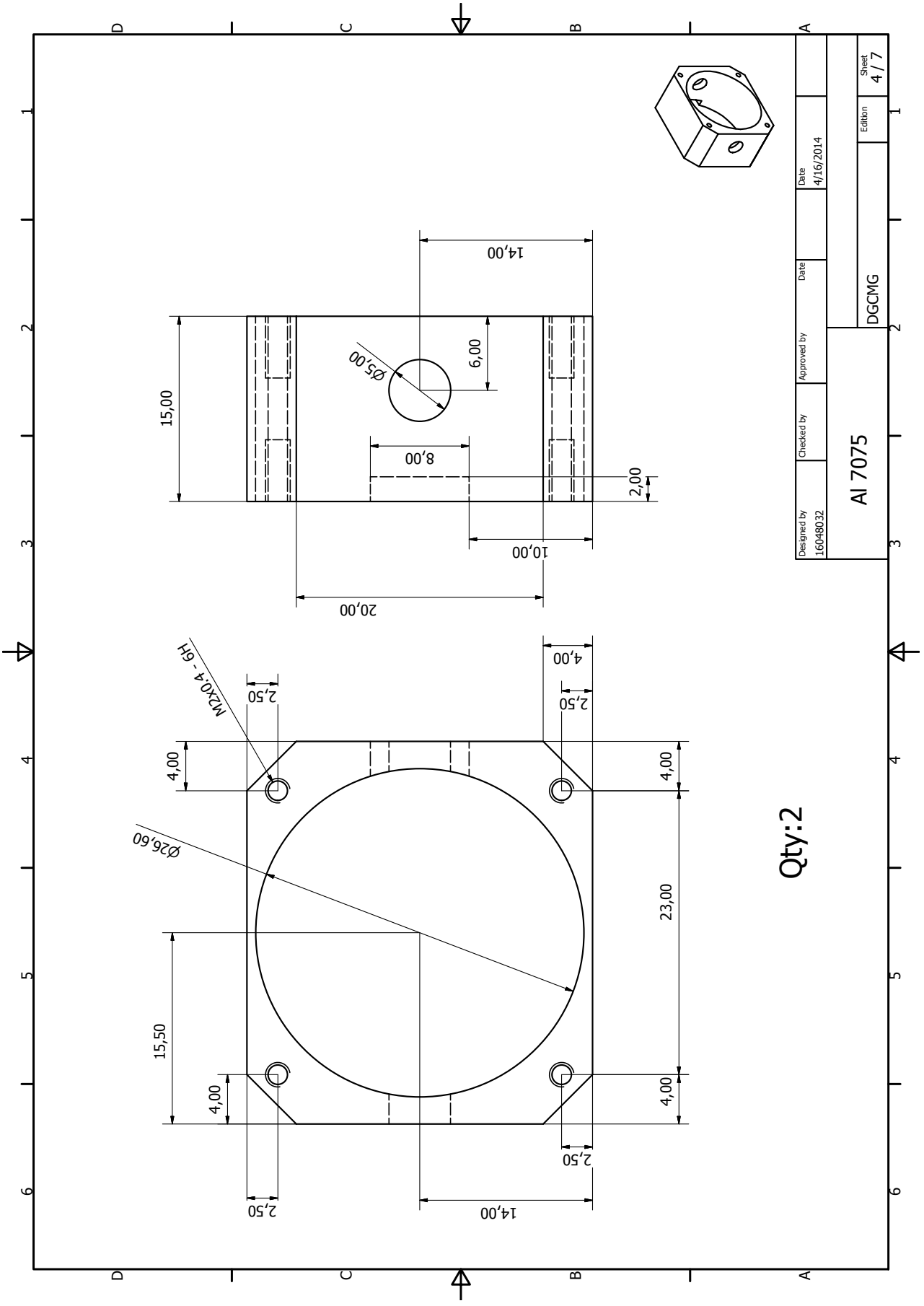

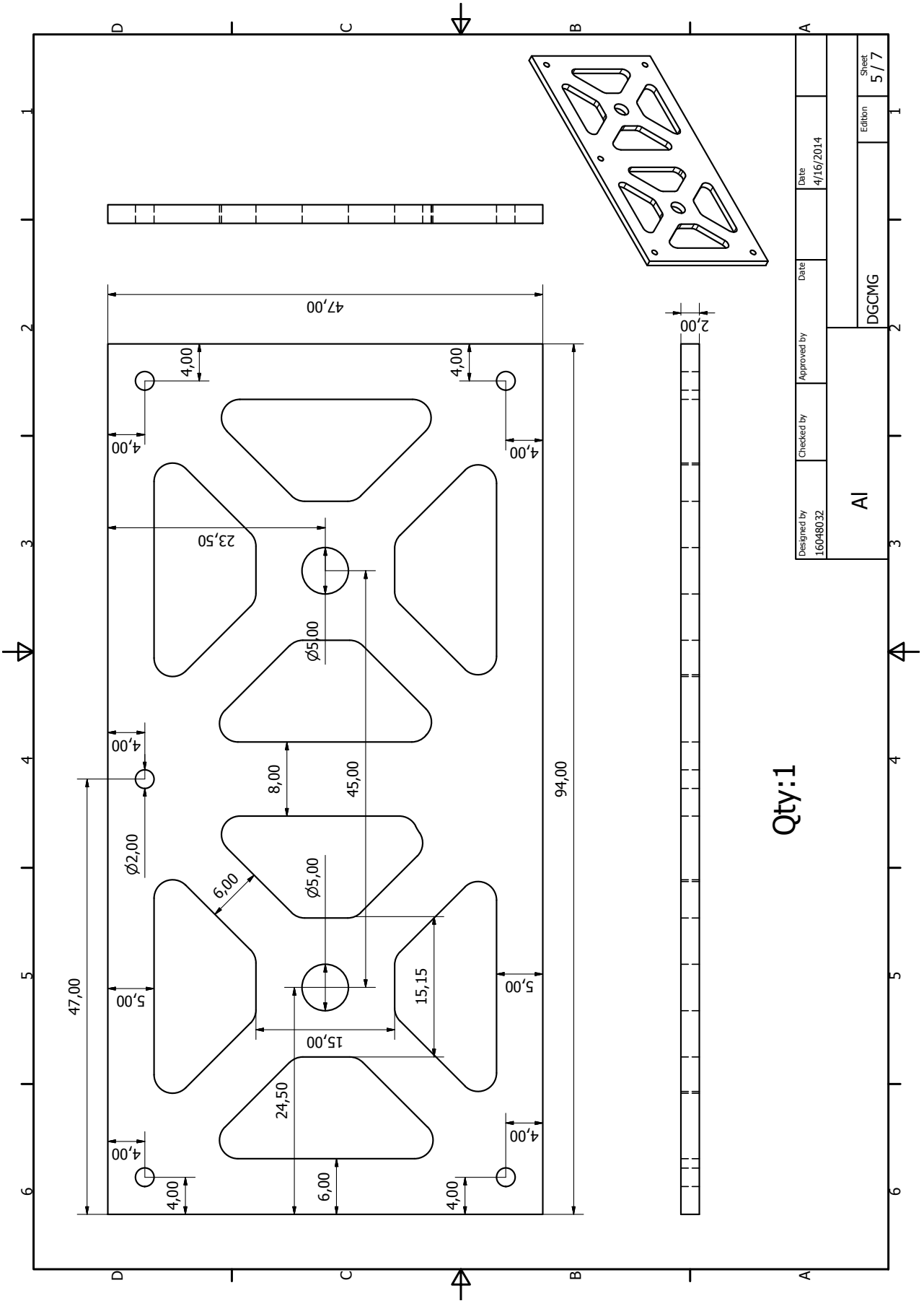

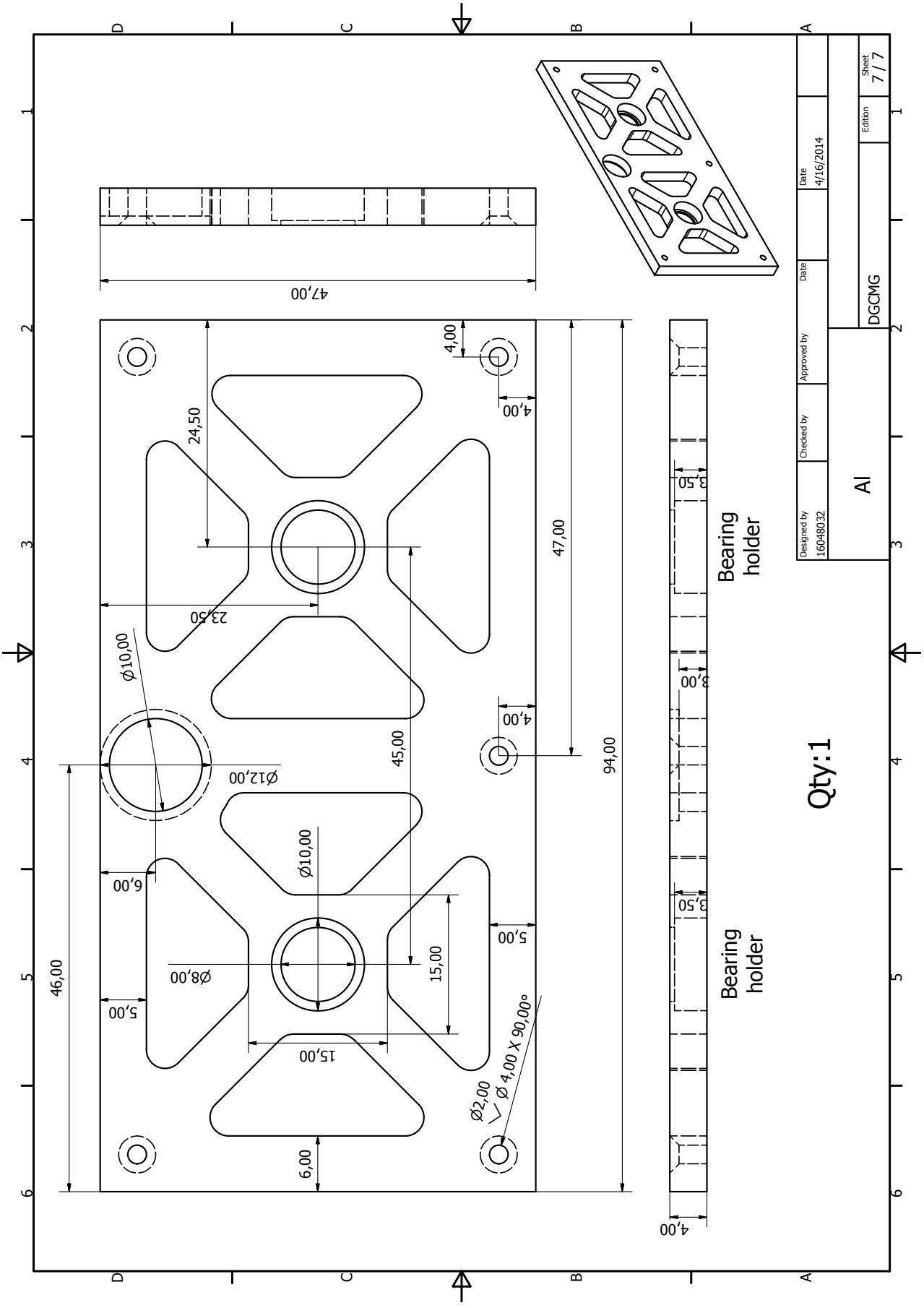

Appendix E

PCB Designs

E.1 Final PCB

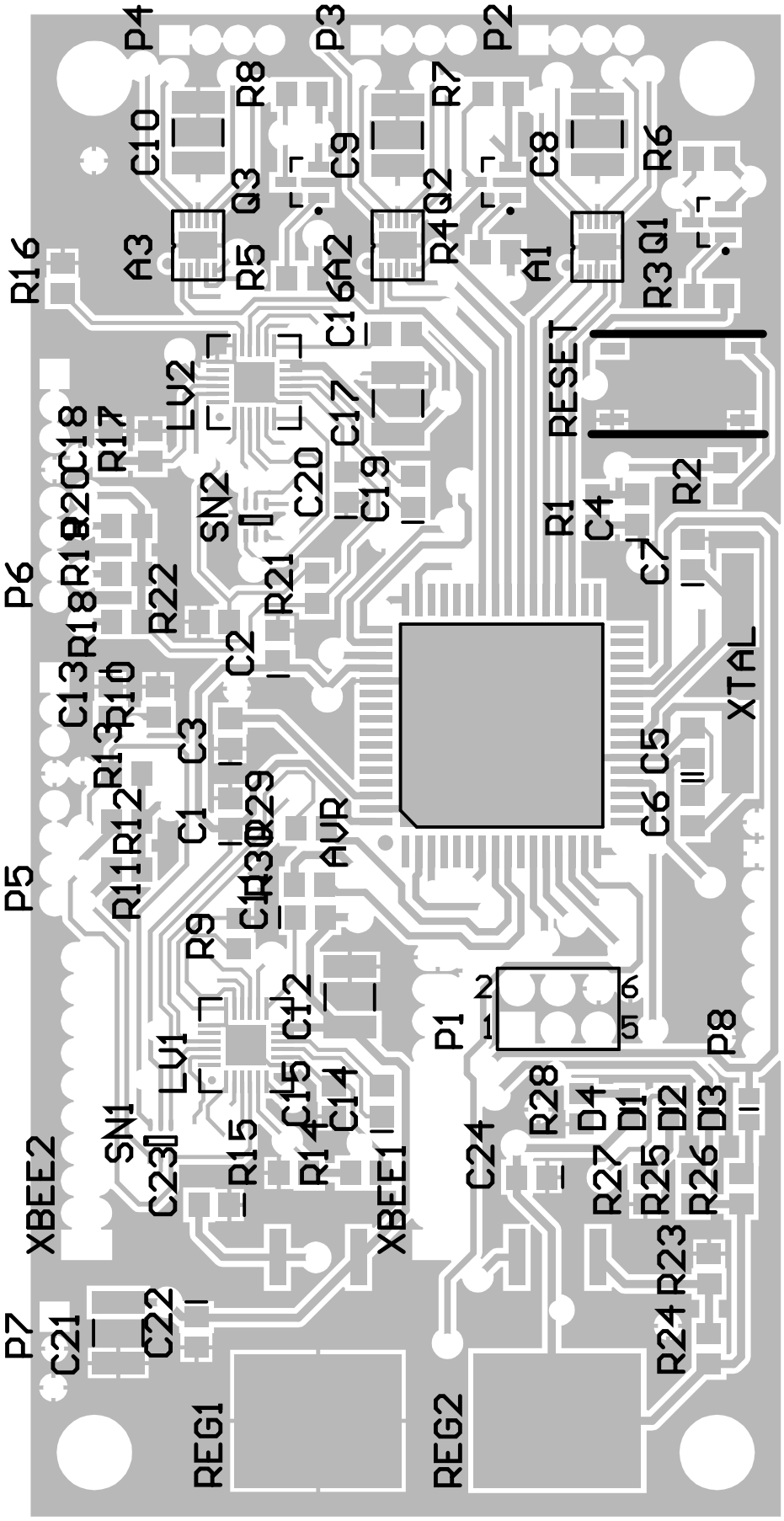

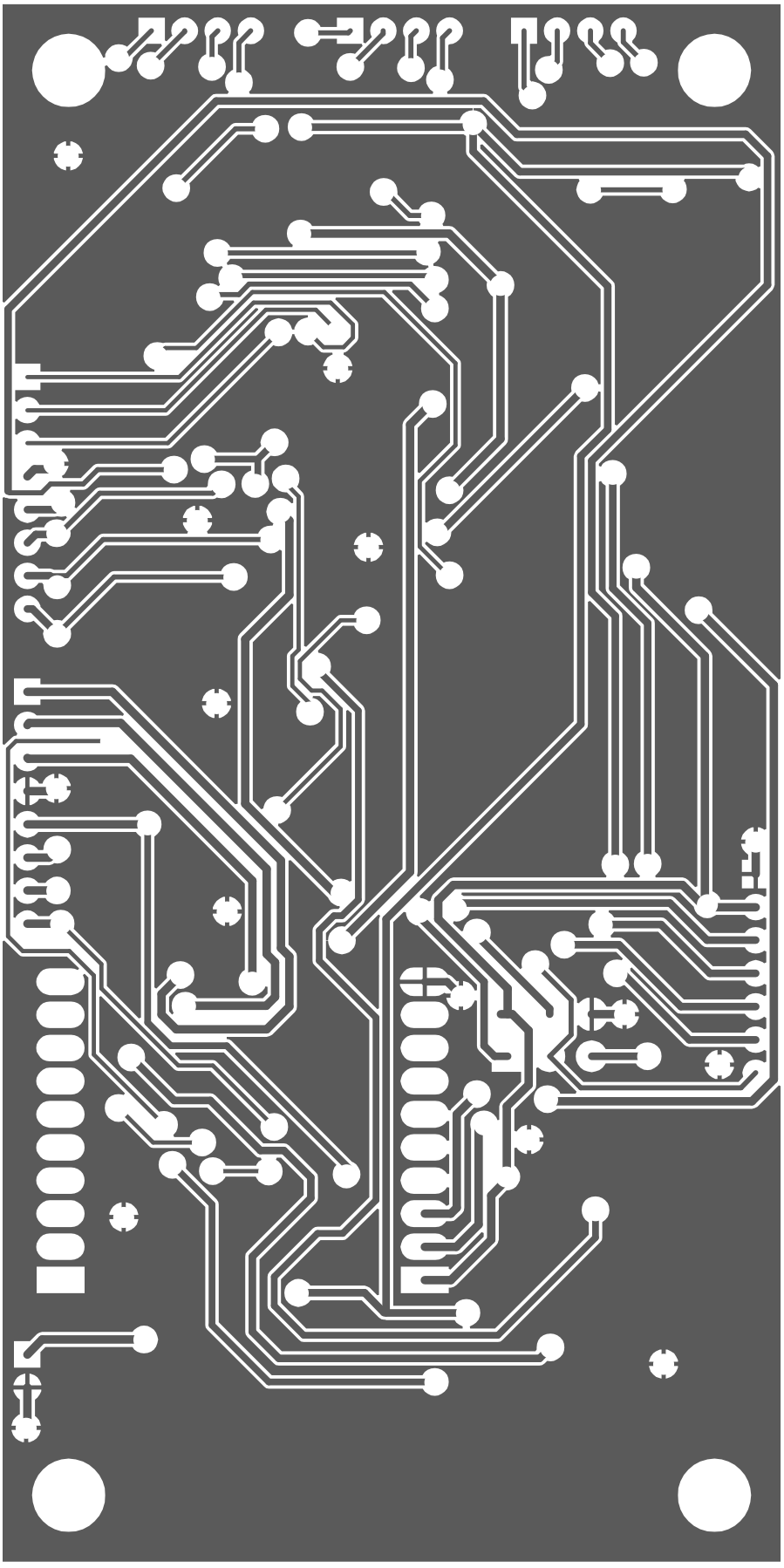

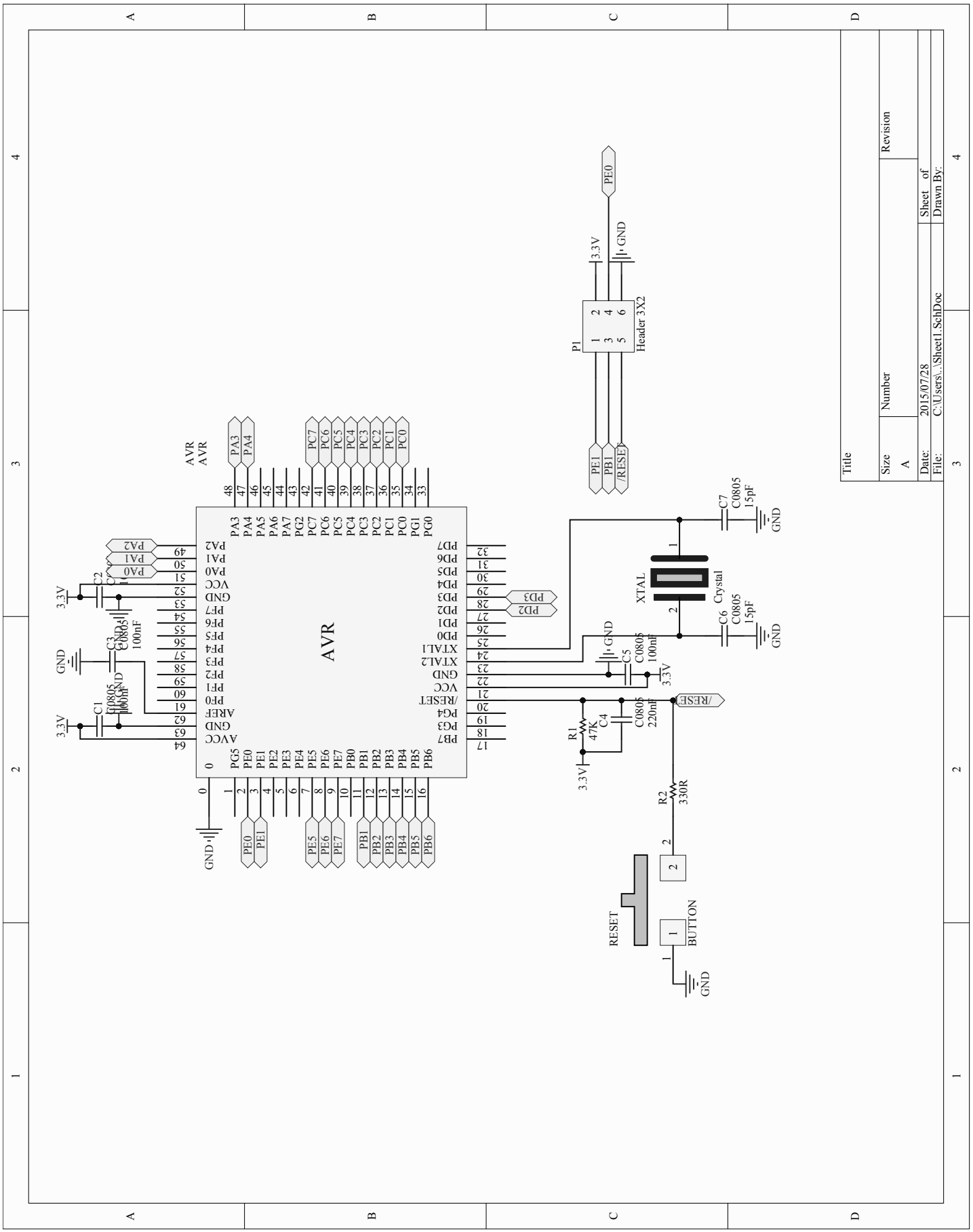

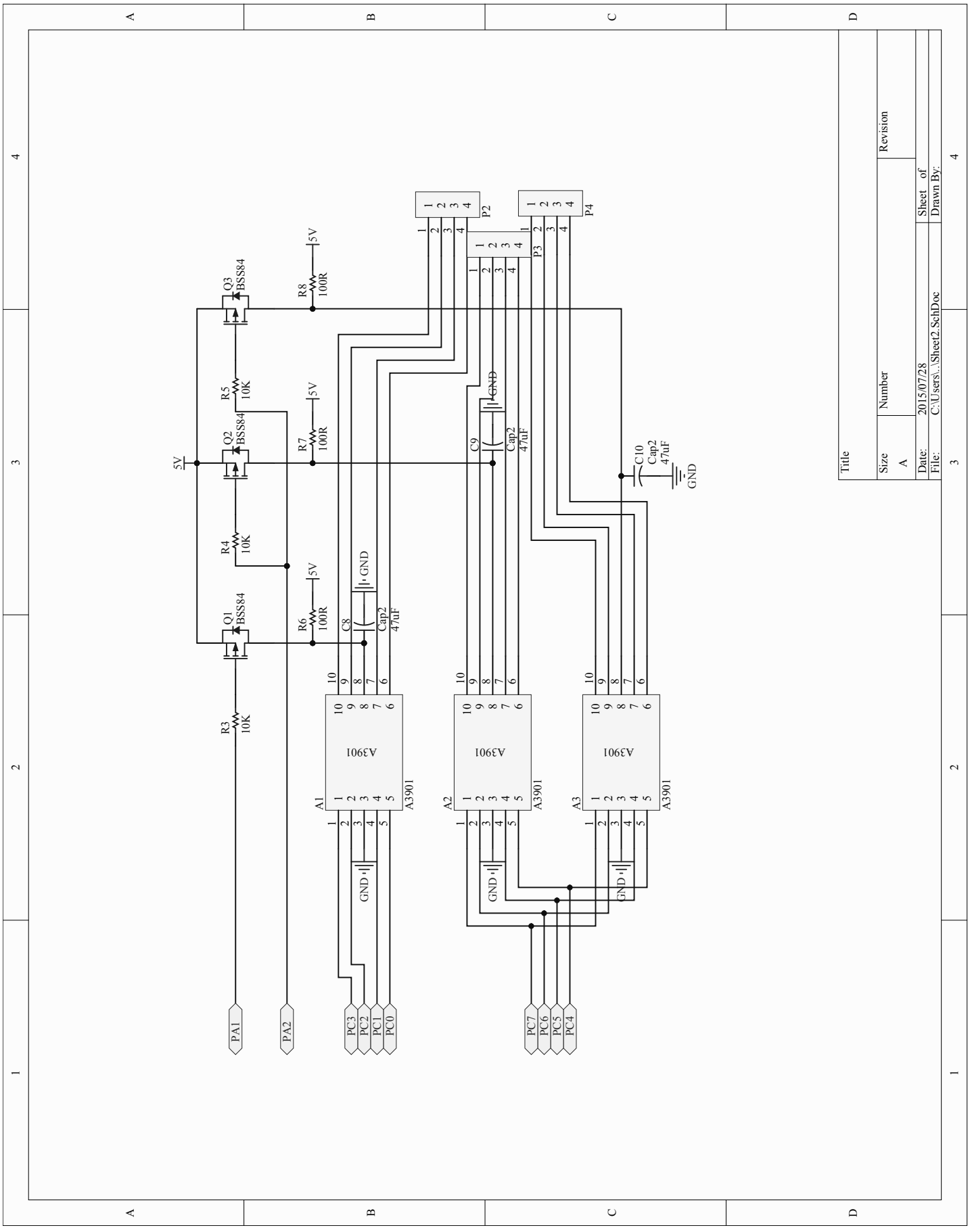

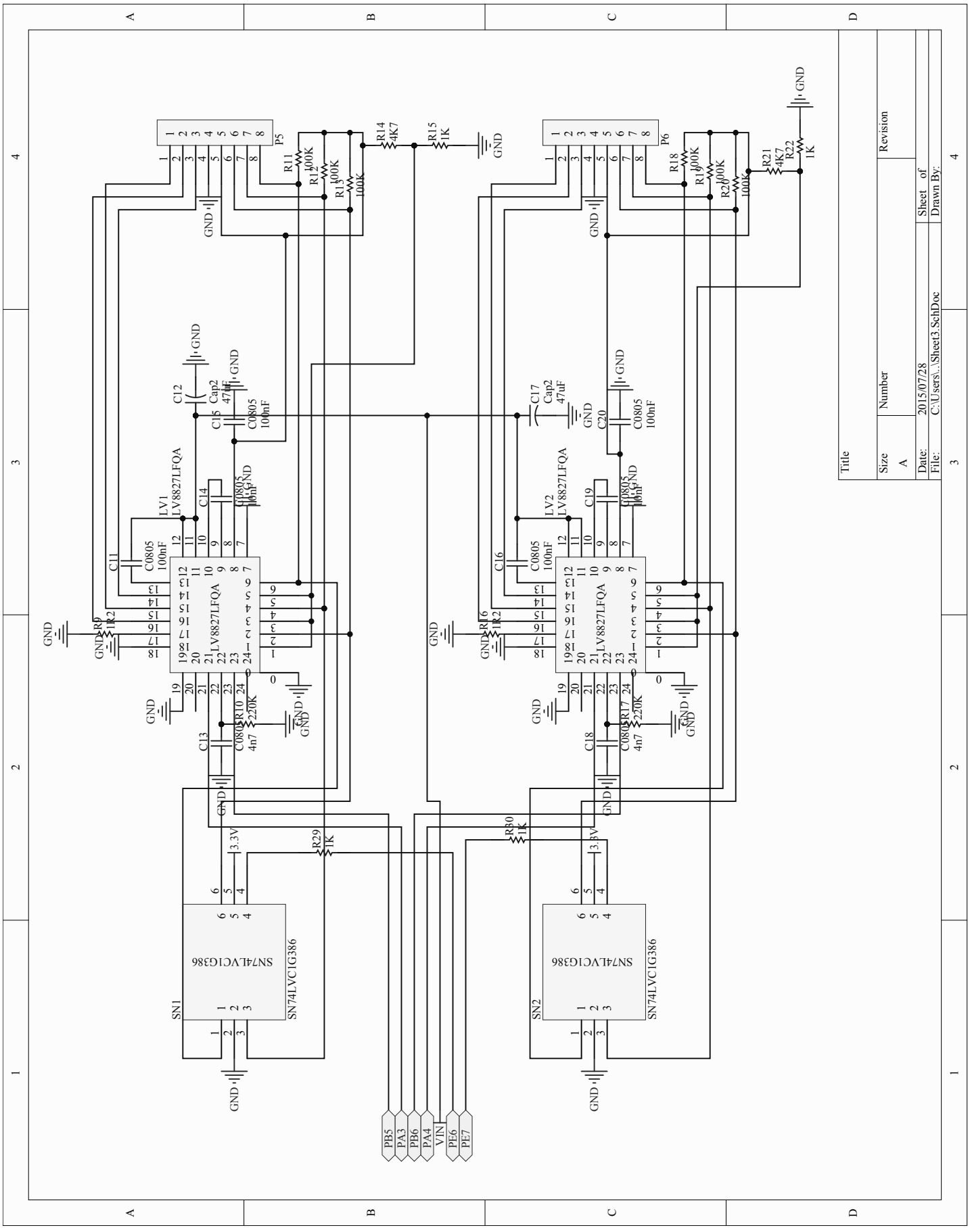

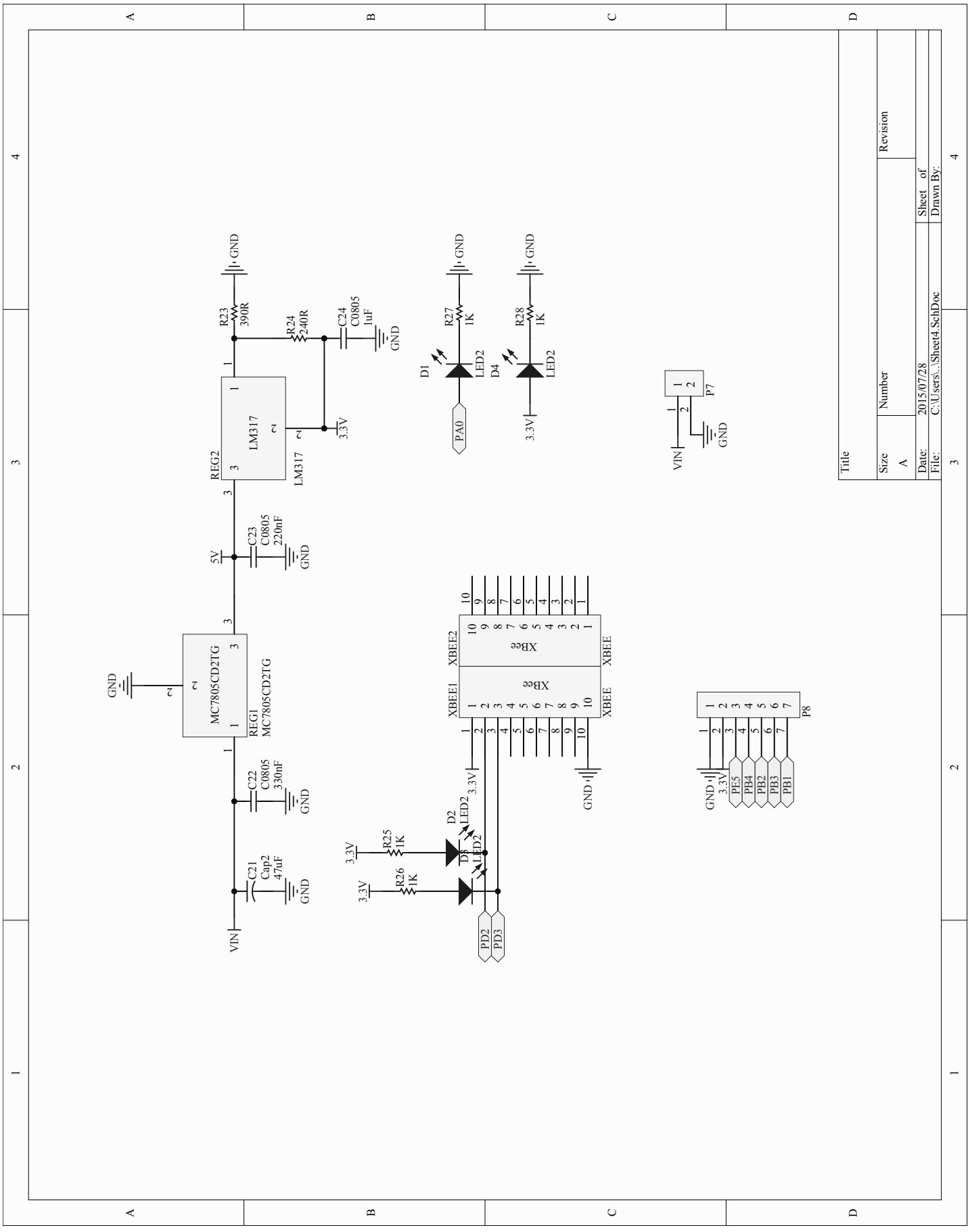

E.2 Driver Test PCBs

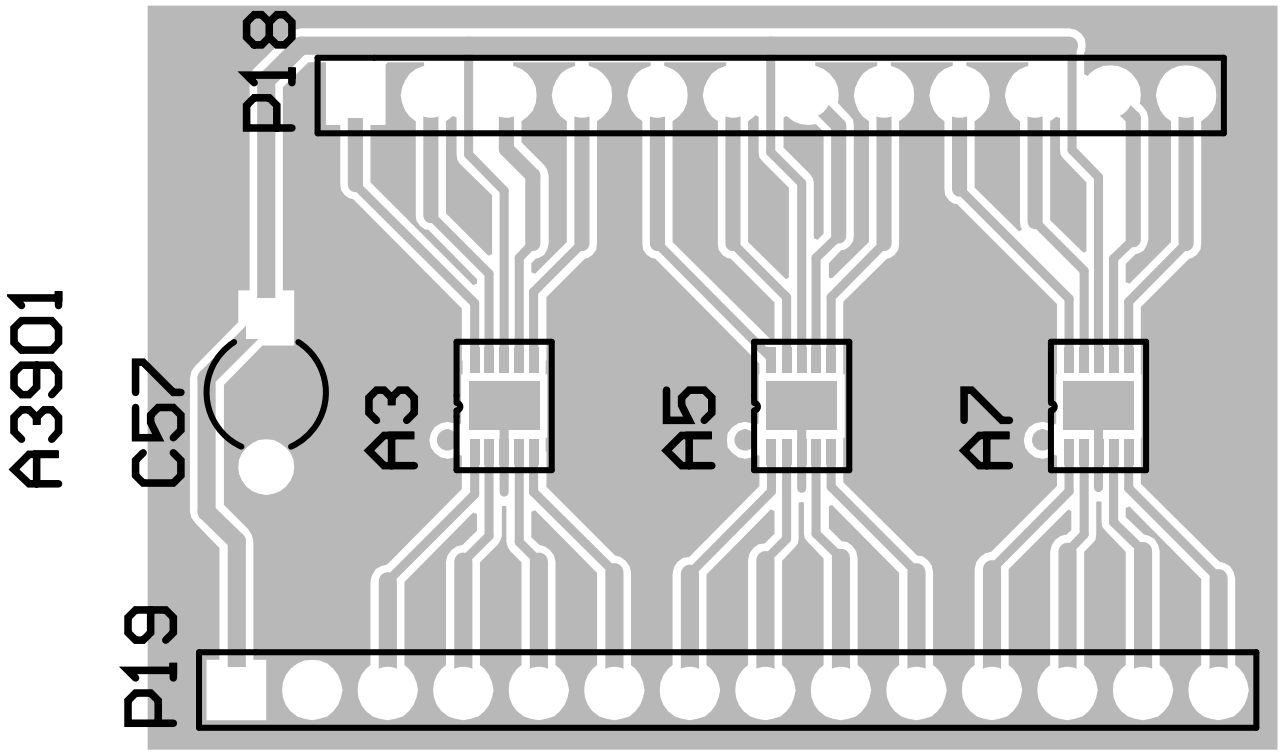

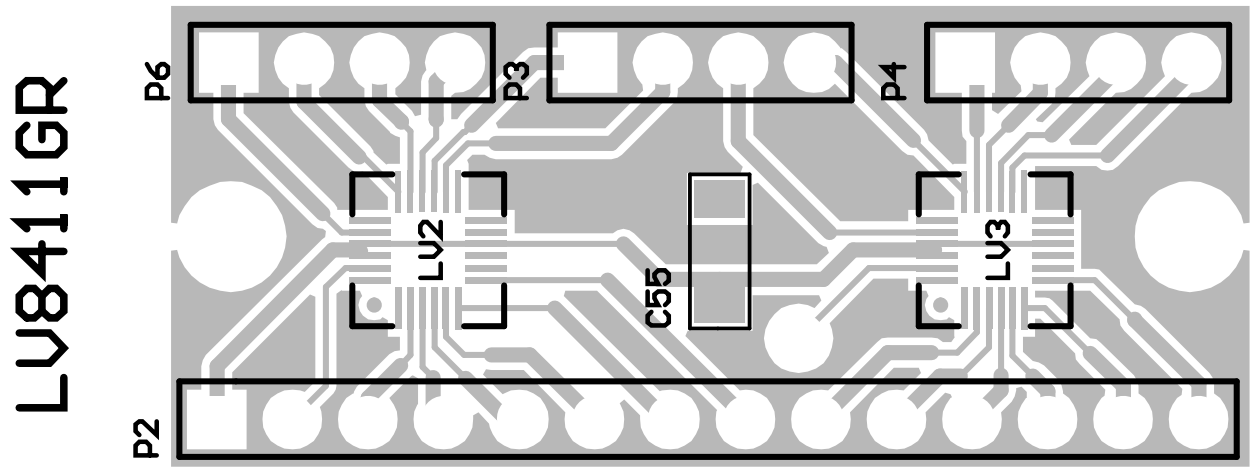

LV8827LFQA

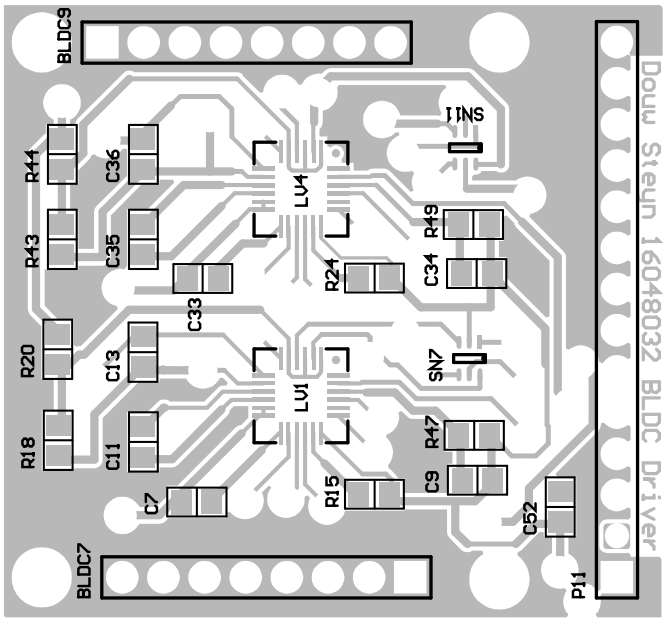

LB1980

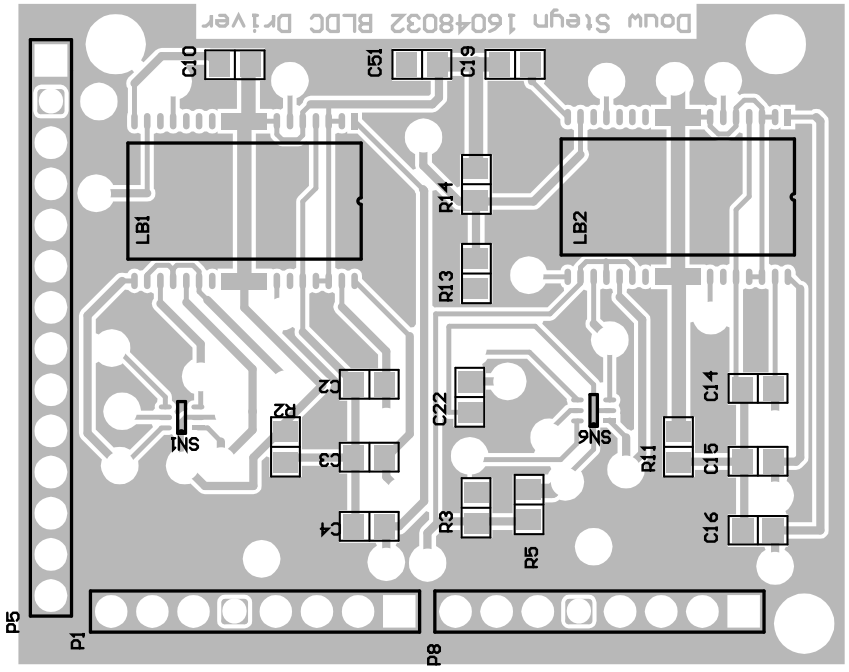

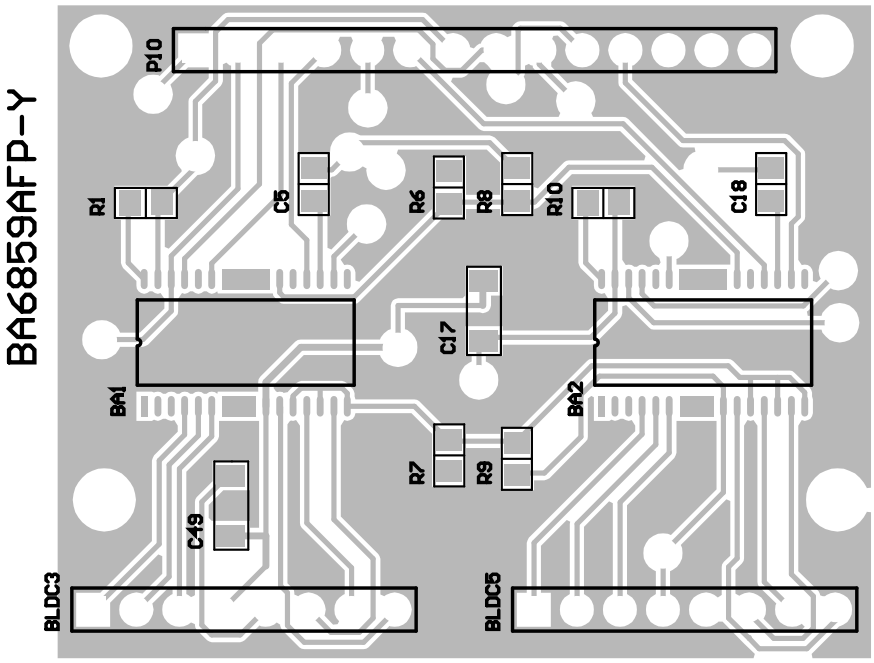

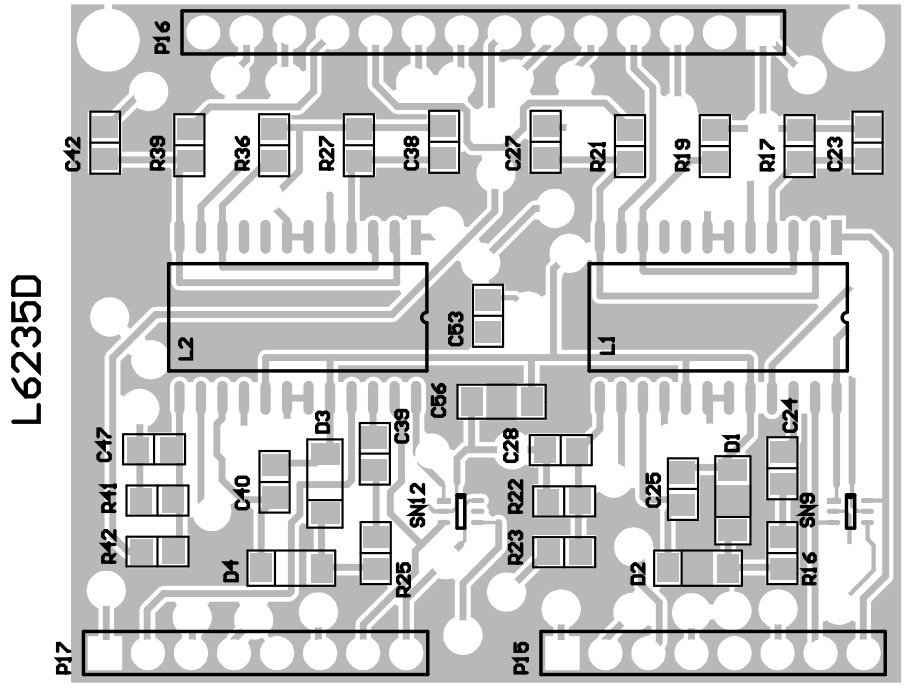

A4941

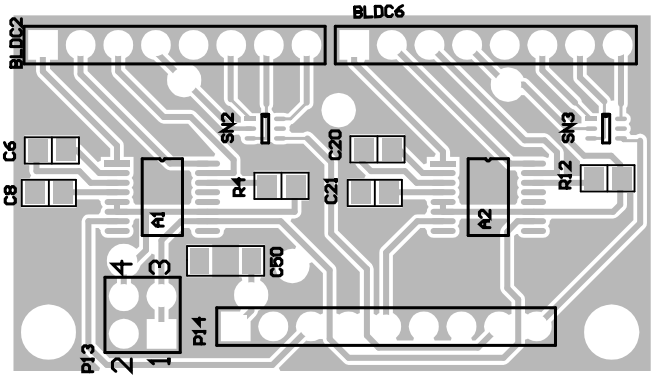

MTD6501D

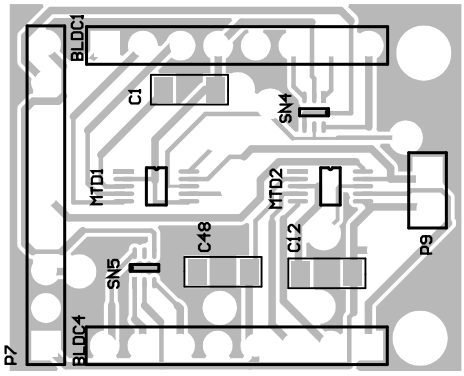

A4915